Curso 2005/06
CIENCIAS Y TECNOLOGÍAS/12
I.S.B.N.: 84-7756-704-2

CRISTINA ABAJAS BUSTILLO

The influence of gravitational microlensing on broad emission lines of quasars

Director
EVENCIO MEDIAVILLA GRADOLPH

SERVICIO DE PUBLICACIONES
UNIVERSIDAD DE LA LAGUNA

SOPORTES AUDIOVISUALES E INFORMÁTICOS
Serie Tesis Doctorales

A mi madre,
por inspirarme en lo intangible del camino.
A mi padre,
por mostrarme siempre un camino.
A Miguel,
por compartir el camino conmigo.

Agradecimientos

En primer lugar quiero expresar mi agradecimiento al Instituto de Astrofísica de Canarias y a su director Prof. Francisco Sánchez por brindarme la oportunidad de realizar esta tesis. Al Dr. Miquel Serra-Ricart y al Dr. Valentín Martínez Piallet por abrirme las puertas del Observatorio del Teide, el cual me ha proporcionado el sustento para realizar esta tesis. También quiero agradecer al Departamento de Astrofíca de la Universidad de La Laguna en las personas de Jordi Cepa y Maria Jesús Arevalo por su hospitalidad en la etapa final.

A mi director de tesis, Dr. Evencio Mediavilla Gradolph, por ser "un genio que ve las cosas en la semilla", y por su infinito optimismo. Asimismo quiero mostrar mi agradecimiento al Dr. José Antonio Muñoz por sus elaborados y valiosos comentarios, y por sacarme de algún que otro atolladero; al Dr. Luka Popović, por su colaboración a lo largo de estos años.

Como no todo ha sido investigar, sino que también hubo que trabajar, quiero dar las gracias a todo el personal con el que he trabajado en el OT; especialmente a mis compañeros operadores, por cambiarme los turnos, facilitándome la asistencia a congresos y la realización de los cursos de doctorado; a los soportes, en particular a Gabi, por el picoteo y el entretenimiento; a Julia y Alberto por compatir la misma situación que nos une; a Lourdes, Loli y Cristino por sus riquísimos guisos; y a todos con los que he compartido un café, una comida, una charla, y probablemente muchas risas y quizás alguna lágrima. No pueden faltar palabras de agradecimiento para mis dos superiores, Dr. Miquel Serra-Ricart y Dr. Alejandro Oscoz, que siempre me han apoyado en este proyecto.

Además, Miquel me acogió en su proyecto de aventuras científicas, y le debo el conocer algunas maravillas del mundo. Por supuesto, no puedo olvidarme del resto del personal de Shelios, Javi, Adela, Juanma (¡gracias por presentame a Miguel!), Angel, Casado y todos lo que pasaron tiempo con nosotros. Ha sido un placer viajar con ustedes y liberar mi mente de la investigación y el trabajo.

Una mención especial a Nuria, a Africa, a las niñas (Aurora, Elena y Mónica), a Atse, a Juanje, a los museros, y como no, a Rudy.

Gracias a todos aquellos amigos que tienen un trocito de mi corazón. A mis amigos del alma: Sofía, Alejandro y Rodri, gracias por existir. A los peninsulares: Marta, Javi y Sara; Eva, Rafa y Celia; Fanny, Fernando y Valvanuz; gracias por compartir vuestro tiempo conmigo; A mis chicas de Navamuel, Estíbaliz, Nuria y Silvia, por las reuniones anuales. A los insulares: Pablo, gracias por las fiestas y por la música; Tony, Eva y Mónica, gracias por acogerme en vuestra casa cuando la mía estuvo inhabitable; Olivia, gracias por ofrecerme refugio en La Gomera; Rosa, gracias por tu sinceridad; Lourdes y Ceci, gracias por las comiditas veraniegas, el vino y las charlas; Esther, gracias por corregir el ingés de esta tesis y sobre todo por hacer de madre adoptiva; Y a todos, incluidos a los que se me haya olvidado mencionar, gracias por vuestra amistad.

Quiero ofrecer un especial agradecimiento a Alex y a Javi. Alex, gracias por ser mi amigo, mi jefe, por las largas conversaciones, las juergas, la comprensión y el apoyo recibido a lo largo de estos años. Javi, gracias por tu amistad, por tener claras tus prioridades, por tus valiosos consejos, por los ratos compartidos con tu familia (Gele, Noelia y Carlos), y por estar siempre ahí.

Gracias a mis padres, Jose Manuel y Loli, por ser los mejores padres del Universo. A mi hermana, Rebeca, por madurar conmigo en la distancia y en la cercanía, y por las largas conversaciones telefónicas de hermana. A mis abuelos, Sabina y Pepe, por mimarme a lo largo de toda mi vida. Al resto de mis familiares, tanto consanguíneos como políticos, gracias por arroparme.

Y muy especialmente quiero darle las gracias a Miguel, que ha hecho que pase de vivir en la tierra a vivir en el séptimo cielo. Gracias por ser mi compañero, mi amigo, por completarme, por tu apoyo incondicional y por caminar junto a mí.

Cristina Abajas

Resumen

En esta tesis se estudia la influencia del efecto microlente gravitatorio sobre las líneas anchas de emisión (BELs) de los cuásares (QSOs) usando las estimaciones más recientes del tamaño de la región de líneas anchas (BLR) y la relación de escalado que existe entre este tamaño y la luminosidad.

El efecto microlente, causado por estrellas u otros objetos compactos, puede producir importantes amplificaciones en las BELs de algunos cuásares sujetos al efecto lente gravitatoria. El efecto microlente podría ser especialmente relevante en las líneas de alta ionización que se generan en la BLR. Hemos identificado un grupo de 10 lentes gravitatorias, que representan aproximadamente al 30% de la muestra estudiada, en las cuales resultaría más favorable observar el efecto microlente. Usando modelos cinemáticos estándar para los núcleos activos de galaxias (AGN), se han estudiado los cambios que una microlente situada en diferentes posiciones respecto al centro de la BLR produce sobre los perfiles de las líneas. El efecto microlente induciría importantes efectos sobre las líneas, tales como la amplificación selectiva de diferentes partes del perfil o el desplazamiento de su pico. El estudio de los perfiles de las BELs con diferente grado de ionización en la misma imagen de un cuásar que haya sufrido el efecto microlente sería un método alternativo para probar cuál es la estructura y el tamaño de la región donde se originan las líneas.

En la segunda parte de esta tesis se ha considerado la aproximación de caústica rectilínea para estudiar la influencia del efecto microlente sobre las BELs. Básicamente, se reproducen los mismos resultados obtenidos que cuando se considera una microlente aislada, especialmente las amplificaciones asimétricas de distintas partes del perfil de las líneas. Esta aproximación es válida para las regiones más internas de los AGN, donde es probable que se generen las líneas de emisión en rayos X.

Finalmente, hemos seleccionado una geometría bicónica para los cuásares con el objetivo de discutir en detalle la influencia del efecto microlente de un

patrón de caústicas sobre los perfiles de las líneas anchas de emisión. La amplificación causada por el efecto microlente usando este modelo anisotrópico no está directamente relacionada con el tamaño intrínseco del bicono (tal y como se medió por el método del eco o reverberación), sino que depende de la orientación del bicono y de la apertura del cono. La orientación del bicono proyectado respecto a la distorsión del patrón de magnificación puede inducir efectos muy interesantes, como las amplificaciones casi periódicas de la parte azul o roja de los perfiles de las líneas de emisión o la carencia de correlación entre las curvas de luz de la región de líneas anchas y del continuo de los cuásares. Los perfiles de las líneas de emisión de una región de líneas anchas, en movimiento respecto a una alta concentración de caústicas, muestran características muy claras y bien definidas en longitud de onda. Estas características son el resultado de muestrear la cinemática de la BLR con el cúmulo de caústicas. El modelo bicónico puede reproducir la variación recurrente del ala azul de la línea detectada en las líneas anchas de emisión de la imagen A de la lente gravitatoria SDSS J1004+4112. Sin embargo, no parece posible reproducir el tiempo de escala observado para este efecto si la fracción de masa en estrellas en el deflector es mayor de un 1% de la masa total. Movimientos paralelos entre el eje del bicono proyectado y la orientación de la distorsión gravitatoria externa conducirían a tiempos de escala excesivamente grandes.

Códigos de la UNESCO:

2101.09: Cosmología y Cosmogonía: Cuásares

2101.04: Cosmología y Cosmogonía: Galaxias

2101.05: Cosmología y Cosmogonía: Gravitación

Abstract

In the present PhD Thesis we discuss several effects of microlensing on the broad emission lines (BELs) of quasars (QSOs) in the light of recent determinations of the size of the broad line region (BLR) and its scaling with QSO luminosity.

Microlensing by star-sized objects can produce significant amplifications on the BELs of some multiple-imaged QSOs, and could be very relevant for high-ionization lines. We have identified a group of ten gravitational lens systems ($\sim 30\%$ of the selected sample) in which microlensing could be observed. Using standard kinematic models for active galactic nuclei (AGN), we have studied the changes induced in the line profile by a microlens located at different positions with respect to the center of the BLR. We found that microlensing could produce important effects such as the relative enhancement of different parts of the line profile or the displacement of the peak of the line. The study of BEL profiles of different ionization in a microlensed QSO image could be an alternative method for probing the BLR structure and size.

In the second part of this PhD Thesis we have considered the straight fold caustic approximation to study the effects of microlensing on the BELs. We basically reproduce the same results obtained in the case of the isolated microlens, in particular the asymmetrical red/blue enhancements. This approximation is valid for the innermost regions of the AGN, where some X-ray emission lines could be generated.

Finally, we have selected the biconical geometry to discuss in detail the influence of microlensing by a caustic network in the profiles of the emission lines. Microlensing amplification in this anisotropic model is not directly related to the bicone's intrinsic size (as measured by the reverberation method) but depends on the orientation of the bicone axis and on the cone aperture. The orientation of the projected bicone with respect to the shear of the magnification pattern can induce very interesting effects, like the quasi-periodic enhancements of the red/blue part of the emission line profile or the lack of correlation between the broad line region and continuum light curves of QSOs. The emission line profiles of a BLR moving in a high caustic concentration exhibit sharp features that are well defined in wavelength. These features (spikes) correspond to the scanning of the kinematics of the BLR by the caustic clusters. The biconical model can reproduce with a transversal (with respect to the shear) movement of the BLR the recurrent blue-wing enhancement detected in the emission line profile of the A image of the lensed quasar system SDSS J1004+4112. However it does not seem possible to match the observed time-scale if the fraction of matter in stars in the deflector is greater than ~1% of the total mass. Parallel movements would lead to excessively large time-scales.

UNESCO codes:

2101.09: Cosmology and Cosmogony: Quasars

2101.04: Cosmology and Cosmogony: Galaxies

2101.05: Cosmology and Cosmogony: Gravitation

Contents

1

Introduction

Pide, y te será concedido;
busca, y lo hallarás;
llama y se te abrirán las puertas.
Mateo 7:7

The gravitational lens effect is a powerful tool to study the broad line region of quasars because this relatively small region can be significantly magnified if it is placed behind a very massive body (a galaxy or a cluster of galaxies), providing clues about its geometry and kinematics.

This chapter is divided into three sections. Firstly, essential data about quasars, their discovery, properties and structure are presented, paying special attention to the broad line region (BLR), where broad emission lines (BELs) are generated. In the second place, a brief summary about gravitational lensing is included, containing an historical perspective, first discoveries and applications. The mathematical description of the theory of gravitational lensing will be extensively treated in a separate chapter, due to its importance in the development of this work. These first two sections give information about each part involved in the study of the influence of gravitational microlensing on BELs of quasars. Finally, motivations and objectives of this PhD Thesis are detailed.

1.1 Quasars

Quasars are among the most distant and luminous objects in the Universe. Light from distant quasars that is received at the Earth now was emitted when the Universe was only a fraction of its current age, and it has been travelling ever since. As light from these distant sources travels to us, there is a reasonable chance that it may be intercepted or deflected by an intervening galaxy along the way, which prints a signature of such an occurrence on the quasar spectrum. Nowadays it is thought that these objects are a type of active galactic nuclei, AGN, whose nuclear point-like emission almost completely outshines the extended stellar light of its host galaxy. Quasars present prominent BELs with equivalent widths[1] of ∼100 Å.

1.1.1 Some history

The observational study of AGN began with Fath. In 1908, when he was studying the spectra of the nuclei of the brightest "spiral nebulae", several emission lines characteristic of gaseous nebulae were identified in the spectrum of the nucleus of one galaxy, NGC 1068 (Fath 1908). In 1943, Carl Seyfert published his notable paper on galaxies with small bright nuclei that emit light with emission line spectrum, exhibit characteristically broadened emission lines, and cover a wide range of ionization. They are now known as "Seyfert galaxies".

Very rapid advance of radio astronomy in the 1950's led to the first optical identifications of the strong radio sources, as Cygnus A, identified by W. Baade and R. Minkowski in 1954, at a -then- astonishing redshift of 0.056. Many bright radio sources come in the form of double lobes with a galaxy located halfway between them with these lobes being connected to the galaxy by jets (Jennison & Das Gupta 1953; Maltby & Moffet 1963; Rees 1971). These radio lobes were the first evidence recognized as indicating nonstellar activity in external galaxies (e.g. Krolik 1999). It took almost a decade to assemble the first useful catalog, the 3C catalog (for 3rd Cambridge University survey), a collection of almost 500 radio sources. By 1960, Minkowski was able to identify the radio source 3C 295 with a galaxy at $z = 0.46$ (Minkowski 1960).

The paradigm about the galactic or extragalactic origin of the radio sources was not resolved until 1963, when C. Hazard and M. Schmidt discovered the first quasar, 3C273. Hazard supplied the accurate radio position from lunar occultations (Hazard, Mackey & Shimmins 1963), which matched with a 13th-magnitude stellar object with an optical jet. Schmidt (1963) provided the optical spectroscopy and redshift, showing broad Balmer emission lines at $z = 0.158$. Based on the great similarity between the spectra of quasars and nuclei of Seyfert 1 galaxies, Barnothy (1965) even proposed that high redshift quasars could actually be the lensed images of distant Seyfert 1 galaxy nuclei (see §1.2

---

[1] The equivalent width is the width of a rectangular line as deep as the continuum level and with the same area as the line under study. This quantity gives a direct measure of the total amount of energy in the continuum removed by the line, assuming that it is in absorption.

and §2 for detailed information on gravitational lens systems).

Radio galaxies were found as the optical counterparts of radio sources from early surveys (Matthews, Morgan & Schmidt 1965). In 1968, Schmitt noticed that there was a variable radio source located at the same position as BL Lac[2]. The radio source VRO 42.22.01 had been observed by MacLeod & Andrew (1968). Further study and discovery of other similar objects led Strittmatter and colleagues to propose that BL Lac and a handful of other sources were candidates for an entire new class of extragalactic object (Strittmatter et al. 1972). In the mid-1970's, it was noted that there was a category of quasar that, in some respects, resembled the BL Lacs. These were the so-called optically violently variable quasars, OVVs (McGimsey et al. 1975).

Nowadays, our knowledge about AGN has advanced enormously and this is now a very important branch of Astronomy. We are now quite certain that active galactic nuclei are powered by accretion onto supermassive collapsed objects (Peterson et al. 2004). Nevertheless, many essential details remain poorly understood. At a fundamental level, the physical origin of variations of AGN is not known, although accretion disc instabilities are probably involved (Peterson 2001). The kinematics and geometry of the broad line region remains unknown. The BELs generated by gas moving in infall, outflow or orbital motion only weakly constrain these possibilities because there are a wide variety of profoundly different kinematic models that yield similar line profiles[3](Peterson 2004).

1.1.2 Properties

The main classes of AGN are: quasars, Seyfert galaxies, BL-Lacs, OVVs, and radio galaxies. Many AGN have a point-like appearance, enormous luminosities ($\sim 10^{42}$ to $\sim 10^{48}$ erg s^{-1}), broad and narrow emission lines and non thermal emission from their nucleus, exhibiting radio-emitting compact cores, often connected by long, narrow jets to gigantic radio lobes up to a million light-years from the core.

The common characteristics of AGN are (Bartelmann & Schneider 2001):

- radio emission which, owing to its spectrum and polarization, is interpreted as synchrotron radiation;
- strong ultraviolet and optical emission lines from highly ionized species;

---

[2] BL Lac objects receive this name because of the first member of the class discovered, an object previously suspected of being a variable star in our Galaxy and which had been catalogued under the name of BL Lacertae (Hoffmeister 1929). This the standard format of naming a variable star.

[3] The detailed shape of a spectral line is called the line profile.

- a flat ultraviolet to optical continuum spectrum, often accompanied by polarization of the optical light (~0.5-10% in linear polarization);
- strong X-ray emission which can be interpreted as inverse Compton radiation;
- strong γ-ray emission which can be interpreted as inverse Compton emission from relativistic jets;
- variability at all wavelengths, from the radio to the γ-ray regime, on time scale from hours to years.

All these phenomena occur at a different level in each class of AGN (Robson 1996; Krolik 1999):

- A quasar is an optically point-like object with strong broad and narrow emission lines in its spectrum, and comparable luminosity in the infrared, optical, and X-ray bands. The redshifts of these spectral lines indicate that the quasars are very distant and very luminous. They are classified into two types: radio-loud quasars and radio-quiet quasars. The former are radio emitters, with some variability and polarization of the optical light, and the latter present these three characteristics weakly.
- An OVV quasar is a highly polarized, radio-loud quasar with an exceptionally rapid and large amplitude variability in the optical band.
- A BL Lac object is similar to a highly polarized, radio-loud quasar, except that it lacks strong broad and narrow emission lines.
- A Seyfert galaxy is (usually) a spiral galaxy with an optically bright nucleus with powerful ultraviolet and X-ray emission. Weak radio emission is detected. Seyfert galaxies are divided into two principal types according to whether their emission lines are broad (type 1) or narrow (type 2) profiles. In addition, Type 1 Seyferts present point-like appearance and some variability and polarization at optical band[4]. These characteristics are missing from Type 2 Seyferts.

---

[4] Type 1 Seyfert galaxies and radio-quiet quasars present similar characteristics, the only distinction is whether a host galaxy is visible. An active galactic nucleus is classified as a type 1 Seyfert galaxy when its host galaxy is visible, whereas when none is visible, it is called a radio-quiet quasar. Seyfert galaxies are on average two orders of magnitude less powerful than quasars and for this reason the host galaxy is visible.

- A radio galaxy is an elliptical galaxy with strong, nonthermal radio emission in the core, jets and lobes. They present strong narrow emission lines. There are two types: broad line radio galaxies and narrow line radio galaxies. The former present a point-like appearance, comparable luminosity in the infrared, optical and X-ray bands, strong BELs and low variability or pbulae were identified in the spectrum of the nucleus of one galaxy, NGC 1068 (Fath 1908).olarization, while the latter do not present any of these characteristics.

The radiation coming from AGN is produced by a wide variety of mechanisms, including high energy γ-ray processes, inverse Compton radiation, atmospheric reprocessing, dust emission and synchrotron radiation. An approach to understand these processes can be found in Blandford (1990). More detailed information can be found in Robson (1996) and Krolik (1999).

1.1.3 Structure

The standard model of an active galactic nucleus (Rees 1984; Weedman 1986; Robson 1996; Ulrich, Maraschi & Urry 1997; Krolik 1999) maintains that the fundamental engine is a supermassive black hole ($> 10^6 M_\odot$) in the core of the galaxy surrounded by an accretion disc, or more generally optically thick plasma, glowing brightly at ultraviolet and perhaps soft X-ray wavelengths. In the innermost region, hot optically thin plasma surrounding and/or mixed with the optically thick plasma gives rise to the medium and hard X-ray emission. Around the accreting supermassive black hole is the broad line region, contained within a large molecular torus and a larger narrow line region (NLR). In some systems, highly relativistic outflows of energetic particles along the poles of the rotating black hole, accretion disc, or torus form collimated radio-emitting jets that lead to extended radio sources (Fig. 1.1).

Unified models attempt to explain the range of AGN on the assumption that they differ only in luminosity, radio brightness and the angle at which they are viewed (Fig. 1.2; Antonucci 1993). The gas and dust torus might hide parts or all of the BLR.

The emission line spectra of AGN are kinematically composite rising in two separate line production regions (Osterbrock 1989; Netzer 1990). The narrow component has Doppler widths usually between 300-1000 km s^{-1} and these emission lines arise in relatively low density gas, $n_e : 10^3 - 10^6$ cm^3, that is spatially extended. In fact, the NLR is at least partially resolved in some of the nearest AGN, showing dimensions of 100-300 pc. In contrast, the broad components have Doppler widths in the range of around 3000-10000 km s^{-1} and arise in gas of fairly high density, $n_e > 10^8$ cm^3 (Netzer 1990). The radius

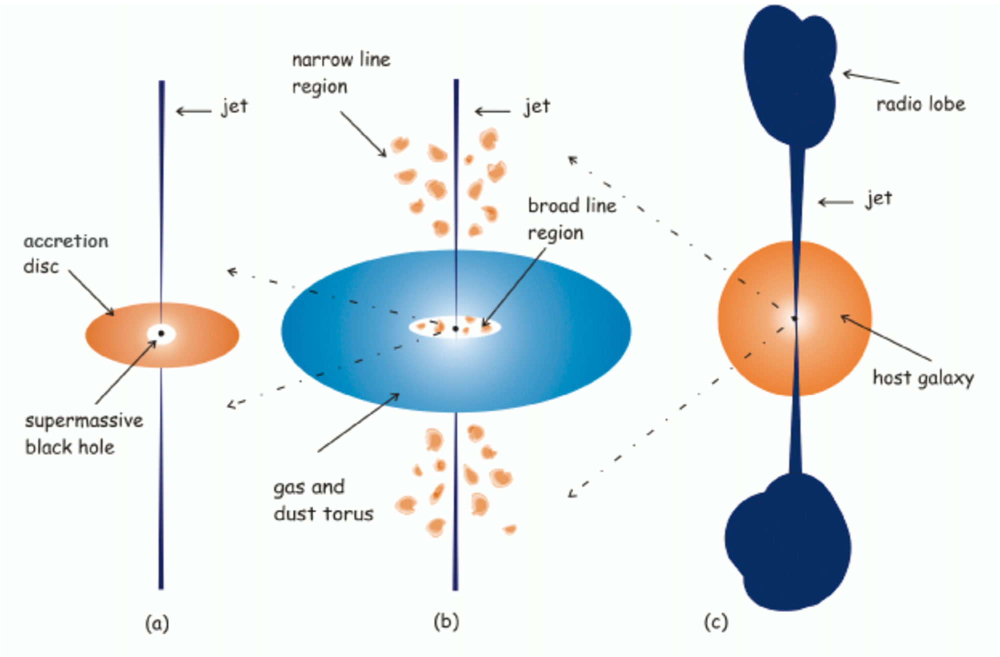

FIGURE 1.1— A generic model for an active galaxy. (a) The central engine is a supermassive black hole surrounded by an accretion disc with jets emerging perpendicular to the accretion disc. (b) The engine is surrounded by an obscuring torus of gas and dust. The broad-line region occupies the hole in the middle of the torus and the narrow-line region lies further out. (c) The entire AGN appears as a bright nucleus in an otherwise normal galaxy. Note that the jets extend to beyond the host galaxy and terminate in radio lobes.

of the BLR is of the order of $10^{16} - 10^{17}$cm (Wandel, Peterson & Malkan 1999), and the effective temperature of BLR clouds is of the order of 10^4 K (e.g. Osterbrock 1989; Netzer 1990; Krolik 1999). Distances are rough estimates, and almost all scale with the luminosity of the active galactic nucleus (Krolik 1999).

BLR

In the standard model, the BLR is composed of a large number of small ($\sim 10^8$ clouds; Arav et al. 1998) discrete, high-density clouds, which are optically thick to the incident hydrogen ionizing continuum and which have a relatively low covering fraction (10% of the sky as seen from the central engine). Since the gas temperature is low ($\sim 10^4$ K), the large line widths (FWHM $\sim 10^4$ km s^{-1}) are attributed to bulk motion of the line emitting gas (e.g. Goad & Koratkar 1998). The characteristic BELs arise from the photoionization of these clouds

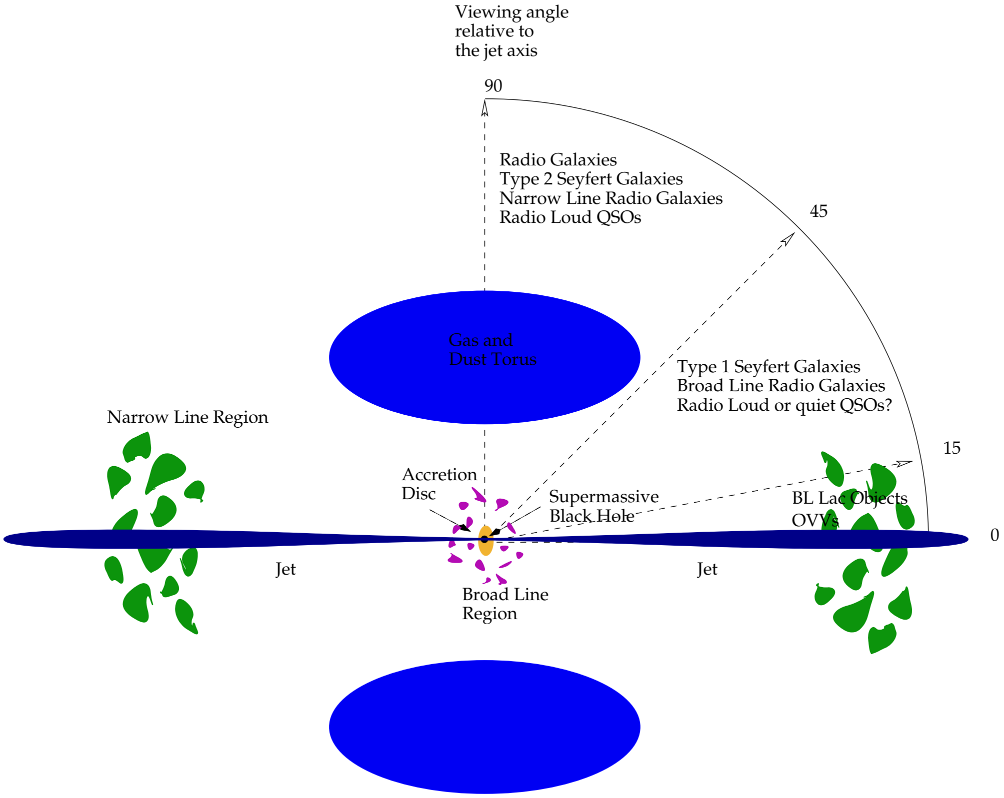

FIGURE 1.2— In the unified model theory, the AGN types depend on the orientation of the viewing angle with respect to the Earth. The angles are approximate.

by the central source. Hence variations in the ionizating continuum are seen as variations in the emission lines with a time delay associated with light travel time (Peterson 1993).

Each cloud contributes to the total line profile of a chemical element with a narrow line, being shifted by Doppler effect from the cloud rest-frame because of the velocity of the cloud along our line of sight.

Detailed models for the structure of the BLR (see, e.g., Collin-Souffrin, Dumont & Tully 1982) indicate that the lines of high-ionization potential (high ionization lines, HILs, like He I and He II lines, O VI λ1035, Lyα λ1216, N V λ1240 or C IV λ1549) are generated in regions close to the central ionizing source while lines of low ionization potential (low ionization lines, LILs, like Balmer lines, Mg II λ2798, C III] λ1909 or the optical Fe II lines) arise further out. Investigations so far, using photoionization and reverberating mapping methods, indicate that there is stratification of gas (see e.g. Gaskell & Sparke

1986, Koratkar & Gaskell 1991, Peterson 1993).

The BLR structure has been investigated using several methods:

Photoionization Method. In the past, the physical properties of the BLR have been characterized by a key parameter, the ionization parameter $U = Q_H/(4\pi r^2 nc)$, where Q_H is the number of hydrogen ionization photons per second, r is the cloud-source distance, c is the speed of light, and n is the density of the photoionized gas. This parameter represents where the photoionization equilibrium of the gas is attained, i.e. where the rate of photoionization is balanced by the rate of recombination (Netzer 1990). Given an estimate of Q_H, and using standard BLR parameters of U and the gas density, therefore, the size of the line emitting region can be obtained from the model. Thus, for a Seyfert 1 galaxy, Q_H is typically 10^{54} photons s^{-1}, with standard parameters $U \sim 10^{-2}$ and $n \sim 10^{9.5}$ cm^{-3}, yields the smallest BLR size of $\sim 2.9\ 10^{17}$ cm, or equivalently 112 lt-days (e.g. Goad & Koratkar 1998).

Reverberation Mapping Method. The technique used in the last few years, which has provided strong supporting evidence for a stratified BLR is the reverberation mapping method (Blandford & Mckee 1982). This technique uses the time lag between the continuum and the emission lines variations to determine the characteristic size of the BLR, or, more accurately, the size of the line emitting region for one particular emission line, and to deduce the masses of black holes, combining the inferred BLR radius with the widths of the emission lines. The derived size of the BLRs were found to be an order of magnitude smaller than that suggested by photoionization calculations (Wandel, Peterson & Malkan 1999), because different line species were found to respond on different timescales (stratification) with steep gradients in either U and/or n (e.g. Goad & Koratkar 1998). This order of magnitude diminishing of the BLR size is crucial for the motivations of this PhD Thesis.

Kaspi et al. (2000), using the reverberation mapping method, derived BLR sizes from the Balmer lines in the range from 13 to 514 light days, finding a global scaling of the BLR size as a function of the intrinsic luminosity, $r_{\mathrm{blr}} \propto L^{0.70\pm0.03}$. This power-law was reanalyzed by Kaspi et al. (2005) using the BLR size from all available AGN over the past 15 years compiled by Peterson et al. (2004) and obtained using this technique as well. Kaspi et al. (2005) found different power-law indexes depending on the wavelength, with the mean best-fitting for the optical continuum and the broad Hβ luminosity $r_{\mathrm{blr}} being \propto L^{0.67\pm0.05}$. The power-law index for the UV continuum luminosity is 0.56 ± 0.05 and 0.70 ± 0.14 for the X-ray luminosity.

At this time there is no consensus among the scientific community as regards the velocity field of clouds in BLR or its geometry. Models involving accretion discs (Chen, Halpern & Filippenko 1989; Dumont & Collin-Souffrin 1990a; Dumont & Collin-Souffrin 1990b), Keplerian cloud ensembles (Kwan & Carroll 1982; Bradley & Puetter 1986; Penston et al. 1990), winds (Perry & Dyson 1985; Smith & Raine 1985), and supernovae (Terlevich et al. 1992), among others, have been discussed. The principal observables which these models seek to explain are the shape and width of the emission line profile, which depend on both the spatial distribution of the emitting gas and its velocity field. It has become apparent from a variety of spectroscopic studies that a wide diversity in the shapes and widths of the profiles of the broad H_α and H_β lines is present among the AGN population (Osterbrock & Shuder 1982; de Robertis 1985; Crenshaw 1986; Stirpe 1990; Jackson & Browne 1991; Boronson & Green 1992; Miller et al. 1992; Eracleous & Halper 1994)

In the present PhD work we use another promising method to study the BLR of AGN, the gravitational lens effect. The first theoretical study was carried out by Nemiroff (1988) and continued by Schneider & Wambsganss (1990). The investigation focused on a few physically motivated models and used the inverse ray tracing method (Wambsganss, Paczyński & Katz 1990; §2.8) to obtain the amplification pattern that simulated the lens galaxy. However, they concluded that the BLR sizes were too extended to be substantially amplified by the gravitational lens effect. No significant attempts were carried out until Abajas et al. (2002) returned to the question using the new estimations of the BLR sizes (Wandel, Peterson & Malkan 1999, Kaspi et al. 2000).

1.2 Gravitational Lensing

The gravitational lens effect is produced when a very massive body (generally a galaxy or a cluster of galaxies) is placed near the line of sight connecting an observer with a distant luminous source, which could be an extended or compact source and is located very far from both the observer and the very massive body. The foreground mass concentration deflecting the light of the background source is called lens. The rays of light travelling from the background source to the observer can follow different paths due to gravitational deflection, generating multiple images, arcs or rings. Furthermore, the light deflection modifies the flux of the images of the source (Chang & Refsdal 1979; Chang & Refsdal 1984; Paczyński 1986; Kayser, Refsdal & Stabell 1986; Schneider & Weiss 1987).

The gravitational lens systems are classified in three classes depending on the optical geometry of the system and the type of source. In the first case, when the observer, the lens and the source are perfectly aligned, the image of the source in the observer plane is a ring image, known as an Einstein ring (Fig. 1.3). If the alignment between the components of the system is not perfect it is possible to observe several images when the source is compact, or several arcs if the source is extended (see, for more details, Schneider, Ehlers & Falco 1992).

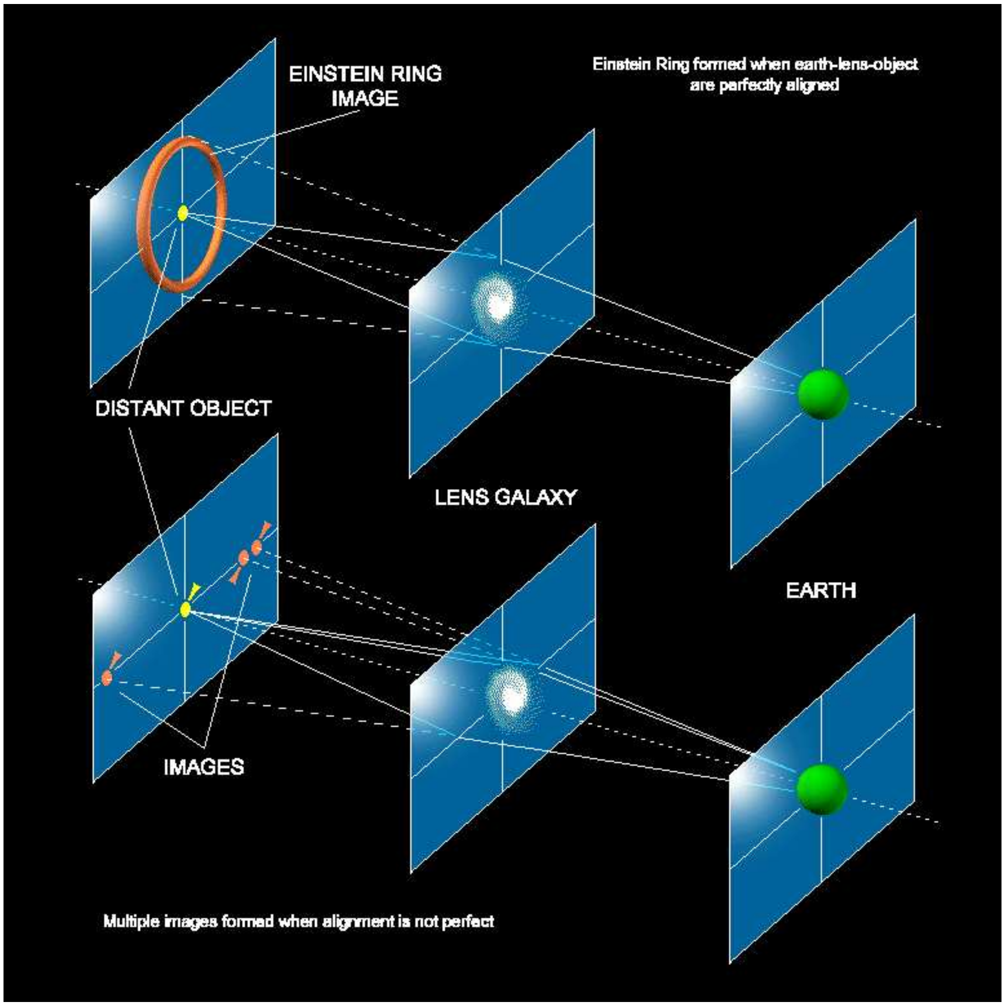

FIGURE 1.3— Two different geometries of the gravitational lens effect.

Lodge was the first researcher using the lens term to define this phenomenon in 1919, and it is still used nowadays although this term is not the most adequate. An ideal lens is an optical system whose focal distance is a constant (distance from focus to the object which bends the light). However, in the gravitational lens system the focal distance depends on the distance between the ray of light and the lens. Attending to this reason it could be better to call them gravitational mirages, because the mirage term explains their nature better (Refsdal & Surdej 1994). The mirages in nature are explained through the Fermat principle, which implies that light will always try to make its velocity the maximum, independently of the medium in which it is moving. A clear example are terrestrial mirages (see Fig. 1.4), which may significantly deform our view of distant objects because of refractive index variations in the air layers just above the ground.

FIGURE 1.4— Terrestrial mirage in Namibia. By Juan Carlos Casado, 2004.

When the light ray bundle from a background source intersects the lens galaxy it can be affected by "discrete" components (star, planet or any dark matter condensation) which do not generate spatially resolved images but do amplify the flux of one of the images generated by the lens galaxy (microlensing; see Fig. 1.5).

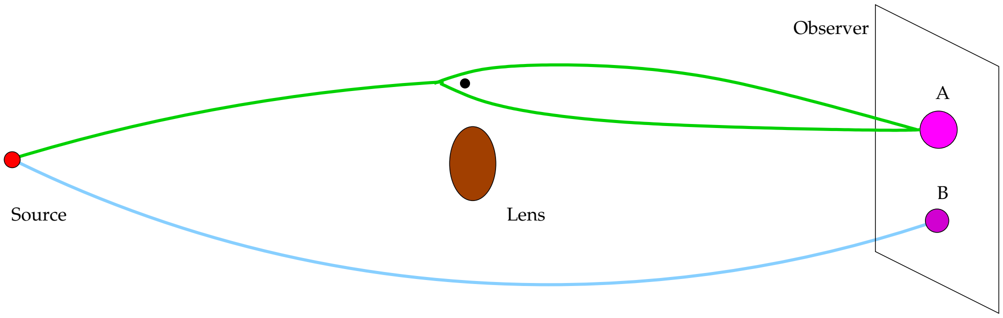

FIGURE 1.5— Microlensing effect.

1.2.1 Some history

At the beginning of the 18th century Newton (1704) had already wondered whether gravity could influence the behaviour of light and if celestial objects could bend the ray of light. He estimated the deflection angle of a ray of light travelling near a spherical body. At the end of this century, Michell (1784) and Laplace (1795) realized that a body with a high enough density would not allow the light to escape from it, so that it would appear completely black. A few years later, and bearing these ideas in mind, Soldner (1804) calculated the deflection angle of a light ray close to the solar limb, assuming that light consists of material particles and using Newtonian gravity.

Once the Theory of General Relativity (TGR) had been developed by Einstein in 1915, this deflection angle was recalculated, predicting an angle twice the value obtained by Soldner (the factor two arises because of the curvature of the metric). The deflection angle computed by Einstein, $\alpha = 1\farcs75$, was confirmed in 1919 during a total solar eclipse when the apparent angular shift of star positions close to the limb of the Sun was measured by Eddington (1920). This experiment meant compelling evidence in support of the TGR.

During the next decades the deflection of light was investigated only in a theoretical way. The existence of multiple images when two stars are sufficiently aligned was suggested by Eddington in 1920, who calculated, although wrongly, the dependence of the flux of the images with the alignment. In 1924 Chwolson pointed out that if the alignment between the stars were perfect, an image with ring form would be obtained. We now call these images Einstein rings. Einstein (1936) discussed the same problem and concluded that the lensing phenomena caused by stars in our Galaxy were difficult to observe. However, Zwicky (1937a,b) noticed that the probability of observing this phenomenon is greater if galaxies are considered, because they produce angular separations which can be observed with telescopes. He noted that observing such an effect would supply an additional test of General Relativity, would allow one to see galaxies at larger distances due to the magnification effect, and would determine the masses of these galaxies acting as lenses.

The great development in the theoretical study of the gravitational lens happened in the 1960's when Klimov (1963), Liebes (1964) and Refsdal (1964a) studied the geometry of the gravitational lens in an independent way. Refsdal (1964b) considered potential applications of gravitational lensing, and he established the relationship between the time delay and the Hubble constant, H_0. Moreover, he considered the possibility of testing cosmological theories by using the lens effect (Refsdal 1966a), and of determining the distances and masses of stars from lensing (Refsdal 1966b).

Chang & Refsdal (1984) suggested the existence of a microlensing effect if a star in the lens galaxy produces flux variations of a distant quasar, in a time scale of a year or less, splitting an image of the source into two or four images separated microarcseconds.

1.2.2 First discoveries

The gravitational lensing became an observational fact in 1979 when Walsh, Carswell & Weymann discovered the first distant quasar with two multiple images lensed by a massive galaxy, Q0957+561. The first gravitationally lensed object with four multiple images was discovered the next year, PG1115+080 (Weymann et al. 1980), but it was necessary to wait until 1986 to discover the first two gravitationally lensed systems generating giant arcs, Abell 370 and Cl2244-02 (Lynds & Petrosian 1986, Soucail et al. 1987). These arcs are produced when both background source and foreground lens are extended objects. Nowadays several radio sources with ring emission shape are known, with MG1131+0456 being the first system discovered in 1988 (Hewitt et al.). The microlensing effect was observed at first in the quadruple lens system Q2237+0305 by Irwin et al. (1989), found by Huchra et al. (1985). The first real detection of weak lensing, little distortions induced by a foreground cluster over a background galaxy cluster, was measured in 1990 around the galaxy cluster Abell 1689 and CL1409+52 (Tyson, Valdes & Wenk 1990).

1.2.3 Applications

In theory, gravitational lenses can be used as versatile tools to address astrophysical problems such as the cosmological model, the structure and evolution of galaxies, and the structure of quasar accretion discs[5].

---

[5] Detailed reviews with cosmological applications of gravitational lensing can be found in

One of the most interesting cosmological applications of gravitational lensing is the determination of the Hubble constant via the measurement of the time delay between different images of a multiple lens system, and a model for the lens. Analyzing statistically the density of gravitational lenses, their separation and redshift distribution, important constraints on the current cosmological models can be supplied, such as the density of the universe, Ω_M, and the cosmological constant, Ω_Λ.

The microlensing in a multiple lens system can produce fluctuations in the light curve of any image. These microlens-induced fluctuations contain information about the lensing objects (mass, density, transverse velocity) and about the lensed source (size of continuum region or BLR of the quasar, brightness profile). When the observations are compared with the microlensing simulations, it is possible to extract conclusions about the density and mass scale of the microlenses. So, it is a method to detect and study the dark condensations, and it would make it possible to detect compact objects in the lens galaxy and in our galaxy (galactic microlensing). It could even be possible to detect planets around other stars.

The study of gravitational arcs in clusters of galaxies make it possible to analyze the properties of galaxies with high redshifts, whose luminosity has been amplified by the lens cluster. The observation of these amplified distorted galaxies clarifies the history of very distant galaxy evolution and estimates the mass and the mass distribution of the cluster without a hypothesis about the relationship between mass and luminosity, supporting the claim that dark matter is the principal constituent ($\geq 90\%$) of galaxy clusters.

The weak lensing is one of the two subdisciplines within the field of gravitational lensing with the highest rate of growth in the last few years (along with galactic microlensing). Weak lensing is due to a mass distribution of large angular size acting as a lens. The effects can be a small deformation of the shape of a cosmic object, or a small modification of its brightness, or a small change in its positions. Weak lensing deals with effects of light deflection that can only be measured in a statistical way. It is used to qualitatively reconstruct the surface mass distribution of foreground galaxies and clusters.

All these applications show that the gravitational lens field promises important results over the next few years. In the next chapter the formal development of the gravitational lensing theory is presented in enough detail for the purposes of this thesis.

Blandford & Narayan (1992), Schneider, Ehlers & Falco (1992), Refsdal & Surdej (1994), Schneider (1996), Wambsganss (1998), Bartelmann & Schneider (2001). This section gives an overview following these papers.

1.3 Motivation and objectives

Gravitational microlensing is now a well known observational phenomenon. The degree of microlensing amplification depends on the scale-size of the source, with smaller sources being more susceptible to suffering large amplifications (e.g. Wambsganss & Paczyński 1991). Microlensing of the continuum is expected, since the optical and UV continuum emission is thought to originate in a region that is comparable in size to the Einstein radius of a typical solar mass star and several studies have attempted to resolve the structure of the region generating the optical and UV continuum by using the microlensing effect as a gravitational telescope (e.g. Yonehara et al. 1999; Wyithe et al. 2000).

On the basis of the standard model for AGN it was accepted that the region generating the BELs of quasars was too large (0.1–1 pc based on simple ionization models) to be substantially affected by stellar-mass lenses (Nemiroff 1988; Schneider & Wambsganss 1990). As reported by these previous studies it was possible to detect only fractional deviations in the magnitude and shape of the lensed from the unlensed line profiles.

However, as mentioned in the previous sections, new results concerning the BLR structure and kinematics could substantially change the common view about the expected influence of microlensing events on the BEL profiles. The above commented study by Wandel, Peterson & Malkan (1999), see §1.1.3, inferred a size of the BLR in the range of a few light days to a few light weeks, one order of magnitude smaller than in previous works.

According to these new findings, the main objective in this PhD Thesis is studying the influence of gravitational microlensing on the BELs of quasars, taking into account the new estimates for the BLR size. The stages in the progression towards this target are:

1. A search for candidates in which microlensing of BLR would be relevant. Estimate of the amplification in these potential candidates.

2. As there is no consensus among the scientific community as regards the velocity field of clouds in BLR or its geometry, different plausible geometries and velocity fields for the BLR -the background source- will be considered.

3. Three relevant approximations for the lens in a gravitational lens system will be used:

    - an isolated compact object,
    - straight fold caustic with infinite length, and

  - a caustic network produced by a random distribution of microdeflectors placed in the lens galaxy.

  Then, several simple models of BLR are used to study the effects of microlensing (under these approximations) on the broad line profiles.

4. A program will be developed to reproduce the necessary magnification patterns for the study of the caustic network approximation case.

5. The effects of microlensing on the continuum of QSOs are compared with those on the BLR.

6. Analyze the possible use of our models in a real case.

2

Theory of gravitational lensing

Las coincidencias no existen.
Todo lo que sucede
forma parte
del fluir universal.
Anónimo

The gravitational lens phenomenon occurs mainly with distant extragalactic sources at $z \geq 1$ and deflectors at $z \geq 0.05$. This chapter gives an overview of the theory of gravitational lenses using the standard cosmological model, a much simpler approximate description of light rays than using Einstein's Theory of General Relativity. In the same way, useful parameters that will be used throughout this PhD Thesis are defined.

For almost all the relevant cases in which the gravitational lens effect takes place it is possible to suppose that the overall geometry of the universe is well described by the Friedmann-Lemaitre-Robertson-Walker metric (see Appendix A). To study light deflection close to the lens it is assumed that the gravitational field is weakly perturbed (small deflection angles), that the matter distribution on the lens is stationary, i.e., the velocity of the matter on the lens is much smaller than the velocity of light, and that all the action of deflection, due to the local matter inhomogeneities, is thought to take place at the same distance to the observer ("thin lens approximation").

Throughout this thesis the standard notation for gravitational lensing is used (Schneider, Ehlers & Falco 1992).

2.1 Deflection angle

The deflection angle $\hat{\alpha}$ of a light ray that passes by a point-like mass M within a distance or impact parameter ξ is, according to General Relativity,

$$\hat{\alpha} = \frac{4GM}{c^2\xi}, \tag{2.1}$$

where G is the gravity constant and c is the speed of light. If $\xi \gg 2GMc^{-2} \equiv R_s$, with R_s being the Schwarzschild radius associated with the mass M, then the deflection angle is small, $\hat{\alpha} \ll 1$, and the gravitational field is weak. In this case, the field equations of General Relativity (Eq. A.2) can be linearized.

This deflection angle, using the weak field limit, can be extended to a surface mass distribution by defining $dm = \sum(\vec{\xi})d^2\vec{\xi}$, where $d^2\vec{\xi}$ is the surface element of the lens plane and $\sum(\vec{\xi})$ is the surface mass density at position $\vec{\xi}$, which is the mass density projected onto the lens plane. Then, Eq. 2.1 can be written as

$$\hat{\alpha}(\vec{\xi}) = \frac{4G}{c^2}\int_{R^2} d^2\xi' \sum(\vec{\xi'})\frac{\vec{\xi}-\vec{\xi'}}{|\vec{\xi}-\vec{\xi'}|^2}. \tag{2.2}$$

Since the gravitational deflection is independent of wavelength, gravitational lenses are achromatic, although indirect chromatic effect may be induced by microlensing since the amplification factor depends on the source size, and this size depends on wavelength (e.g. Refsdal & Surdej 1994).

2.2 Lens Equation

The equation describing the gravitational lensing phenomenon is an equation that relates the true position of the source to its observed position in the sky, and it is called the lens equation. The source and lens planes are defined as planes perpendicular to a straight line (the optical axis) from the observer to the lens, at the distance of the source and of the lens, respectively. The exact definition of the optical axis does not matter because of the smallness of the angles involved in a typical lens situation, and the distance to the lens is well defined for a geometrically-thin matter distribution. Let $\vec{\eta}$ denote the two-dimensional position of the source on the source plane and $\vec{\xi}$ the two-dimensional separation between the light ray and the optical axis on the lens plane. The deflection angle, $\hat{\alpha}$, relates both angular distances through the lens equation:

$$\vec{\eta} = \frac{D_s}{D_d}\vec{\xi} - D_{ds}\hat{\alpha}(\vec{\xi}), \tag{2.3}$$

with D_s, D_d and D_{ds} being the angular diameter distances between observer-source, observer-lens, and lens-source, respectively[1].

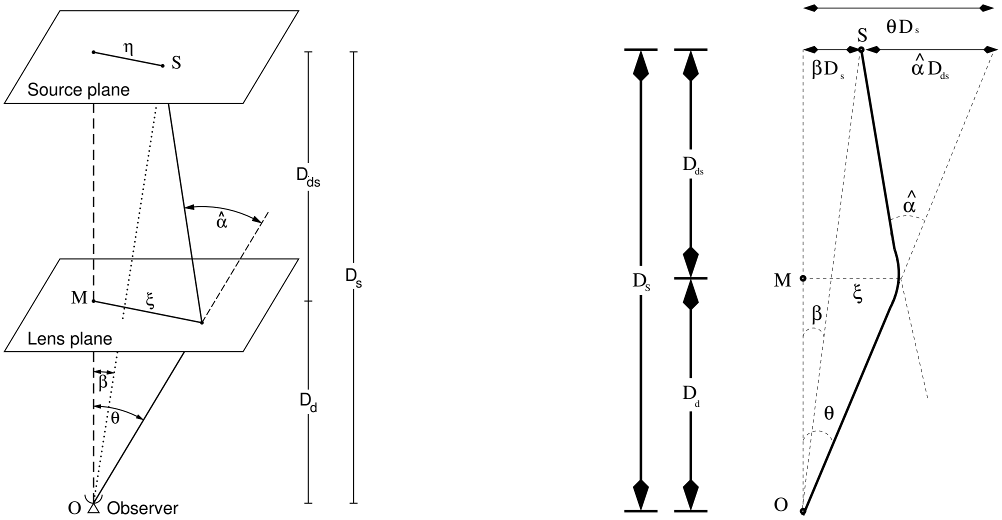

FIGURE 2.1— Sketches of a typical gravitational lens system for a point mass lens M at a distance D_d from an observer O, and a source S at a distance D_s from O. A light ray from S with angular separation β that passes the lens at distance ξ is deflected by $\hat{\alpha}$; the observer sees an image of the source at angular position $\theta = \xi/D_d$. The left-hand panel shows a three-dimensional sketch of a gravitational lens and the right-hand panel shows the corresponding sketch for two dimensions.

Introducing angular coordinates by $\vec{\eta} = D_s\vec{\beta}$ and $\vec{\xi} = D_d\vec{\theta}$, Eq. 2.3 can be transformed to

$$\vec{\beta} = \vec{\theta} - \frac{D_{ds}}{D_s}\hat{\alpha}(D_d\vec{\theta}). \tag{2.4}$$

The interpretation of this lens equation is that a source with true position $\vec{\beta}$ can be seen by an observer at angular position $\vec{\theta}$ satisfying Eq. 2.4 as sketched in Fig. 2.1.

Depending on the matter distribution on the deflector and the position of the source, $\vec{\beta}$, Eq. 2.4 can have more than one solution, i.e the lens can produce multiple images at several positions in the sky.

The ray-trace equation (Eq. 2.3) allows us to determine directly the true source position $\vec{\beta}$ if an image position $\vec{\theta}$ and the deflection law $\hat{\alpha}$ are known. However, the typical problem in the gravitational lens theory is to invert the lens

---

[1] Gravitational lensing occurs in the universe on large scales and a cosmological model must be used. In general the angular diameter distance $D_{ds} \neq D_s - D_d$. For a correct calculation of distances using a Friedmann cosmology see Appendix A.

equation, i.e. to find all the images of a source for a given matter distribution or to find, for given image positions, a suitable matter distribution. These problems can only be solved numerically for general deflectors.

Finally, it is very useful to rewrite the lens equation (Eqs. 2.3, 2.4) in a dimensionless way. For this purpose a new set of vectors are defined, $\vec{x}$ for the lens plane and $\vec{y}$ for the source plane

$$\vec{y} = \frac{\vec{\eta}}{\eta_o}, \quad \vec{x} = \frac{\vec{\xi}}{\xi_o}, \tag{2.5}$$

where η_o y ξ_o are characteristic lengths on the source plane and the lens plane, respectively, with $\eta_o = D_s/D_d\ \xi_o$. Moreover, η_0 is known as the Einstein radius and it defines the angular scale of the lensing scenario. It can be written as

$$\eta_0 = \sqrt{\frac{4GM}{c^2}\frac{D_s D_{ds}}{D_d}}, \tag{2.6}$$

with $\theta_0 = \eta_0/D_s$. If a source lies exactly behind the lens, on the optical axis, then the image of the source is a ring, with angular radius η_0 (see Fig. 2.2).

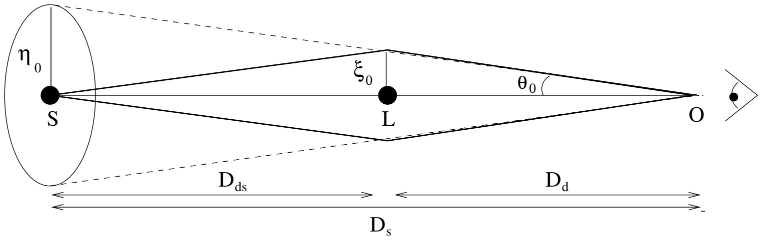

FIGURE 2.2— A source S on the optical axis behind a circular symmetric lens L is imaged as a ring with an angular radius, η_0, given by the Einstein radius θ_0.

The matter distribution on the deflector can be quantified by the dimensionless surface mass density or convergence:

$$k(\vec{x}) = \frac{\sum(\xi_o\vec{x})}{\sum_{cr}}, \quad \text{with} \quad \sum_{cr} = \frac{c^2 D_s}{4\pi G D_d D_{ds}}, \tag{2.7}$$

where $\sum_{cr}$ is called the critical surface mass density. A sufficient condition for producing multiple images of a background source is that $\kappa \geq 1$, i.e. $\Sigma \geq \Sigma_{cr}$, but this is not strictly necessary.

Using these definitions (Eqs. 2.5, 2.7), the ray-trace equations (Eqs. 2.3, 2.4) are transformed to:

$$\vec{y} = \vec{x} - \vec{\alpha}(\vec{x}), \tag{2.8}$$

with the scaled deflection angle being:

$$\vec{\alpha}(\vec{x}) = \frac{1}{\pi}\int_{R^2} d^2x' k(\vec{x}')\frac{\vec{x}-\vec{x}'}{|\vec{x}-\vec{x}'|^2} = \frac{D_d D_{ds}}{D_s \xi_o}\hat{\alpha}(\xi_o \vec{x}). \tag{2.9}$$

The length scale ξ_0 is arbitrary and it can be chosen, for each specific lens model under consideration, such that the lens equation 2.8 is the simplest. For $\xi_0 = D_d$, $\vec{x}$ and $\vec{y}$ are the angular positions of the image, $\vec{\theta}$, and the unlensed source, $\vec{\beta}$, respectively, as can be seen from Eq. 2.4

2.3 Deflection potential

It is possible to define the deflection angle as the gradient with respect to $\vec{x}$ of a deflection potential ψ, using the identity $\nabla|\vec{x}| = \vec{x}/|\vec{x}^2|$ in Eq. 2.9, getting

$$\vec{\alpha}(\vec{x}) = \nabla\psi(\vec{x}), \tag{2.10}$$

where

$$\psi(\vec{x}) = \frac{1}{\pi}\int_{R^2} \kappa(\vec{x}) \ln|\vec{x}-\vec{x}'| d^2x' \tag{2.11}$$

is the logarithmic potential associated with the surface density $\kappa(\vec{x})$.

The ray-trace equation can be rewritten using the deflection potential ψ (Eq. 2.11) as

$$\vec{y} = \nabla\left[\frac{1}{2}\vec{x}^2 - \psi(\vec{x})\right], \tag{2.12}$$

which can also be expressed in terms of the scalar function

$$\phi(\vec{x},\vec{y}) = \frac{1}{2}(\vec{x}-\vec{y})^2 - \psi(\vec{x}) \tag{2.13}$$

and the lens equation can be shown as

$$\nabla\phi(\vec{x},\vec{y}) = 0, \tag{2.14}$$

which is the formulation of Fermat's principle in the gravitational lens theory. The Fermat potential ϕ allows the calculation of the time delay for image pairs of a particularly simple source.

2.4 Amplification

Gravitational light deflection can lead to multiple imaging because of the differential deflection across a light bundle, and to different properties of the images of a source. Between these properties are the shape or size of images.

If the cross section area of a light bundle is distorted by deflection, the flux of the observed image will change (see Fig. 2.3). The magnification μ of an image is the ratio between the fluxes observed from the image and from the unlensed source. It is important to bear in mind that Liouville's theorem[2] and the absence of emission and absorption of photons in gravitational light deflection imply that lensing conserves surface brightness. Hence, the magnification of an image can be expressed as the local solid angle distortion of an image due to the lens, which is described by the Jacobian matrix of lens equation (Eq. 2.8)

$$A(\vec{x}) = \frac{\partial \vec{y}}{\partial \vec{x}}, \quad A_{ij} = \frac{\partial y_i}{\partial x_j}, \tag{2.15}$$

which, using Eqs. 2.12 and 2.13, implies

$$A_{ij} = \phi_{ij} = (\delta_{ij} - \psi_{ij}), \quad \text{with} \quad \psi_{ij} = \frac{\partial^2 \psi(\vec{x})}{\partial x_i \partial x_j}. \tag{2.16}$$

The magnification, $\mu(\vec{x})$, is the inverse of this matrix $A(\vec{x})$

$$\mu(\vec{x}) = \left| \frac{\partial \vec{x}}{\partial \vec{y}} \right| = \frac{1}{detA(\vec{x})}. \tag{2.17}$$

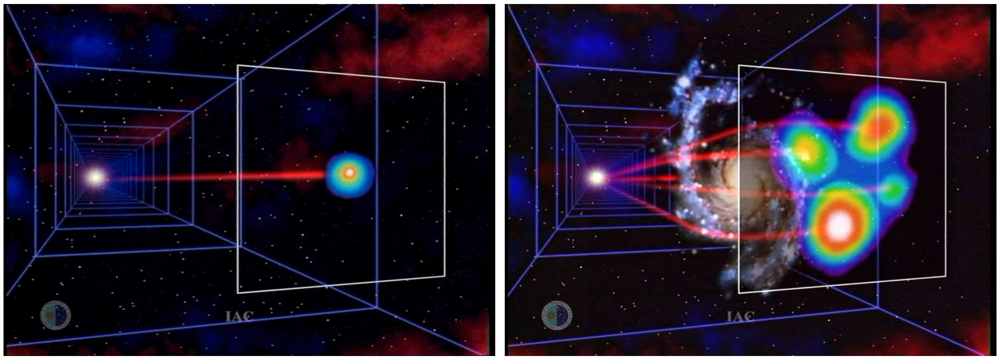

FIGURE 2.3— On the left-hand panel an image of a background source is represented. On the right-hand panel gravitational light deflection by a galaxy is illustrated, with multiple images of the background source, Q2237+0305, appearing with different shapes, sizes and fluxes.

---

[2] When one member of an ensemble and its trajectory (q(t),p(t)) in the phase space is considered, Liouville's theorem states that the time derivative of the density $\rho(q(t), p(t), t)$ as we move along the trajectory is zero, i.e., ρ describes an incompressible fluid.

2.5 Convergence and shear

The deflection potential $\psi(\vec{x})$ is the two dimensional analogue of the Newtonian gravitational potential and satisfies the Poisson equation (inverting Eq. 2.11)

$$\Delta\psi(\vec{x}) = 2\kappa(\vec{x}). \tag{2.18}$$

Since the Laplacian of ψ is twice the convergence, we have

$$\kappa = \frac{1}{2}\left(\psi_{11} + \psi_{22}\right). \tag{2.19}$$

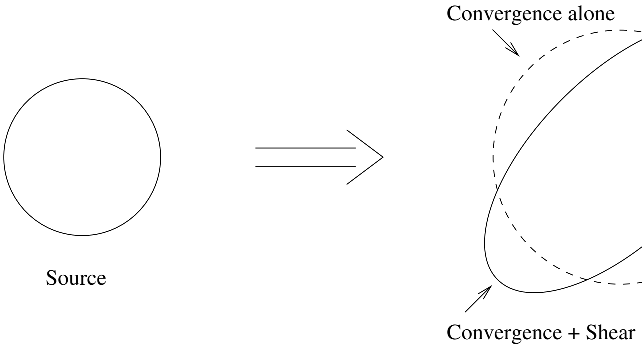

FIGURE 2.4— Illustration of the effects of convergence and shear on a circular source. Convergence magnifies the image isotropically, and shear deforms it to an ellipse.

Two additional linear combinations of ψ_{ij} are important, and these are the components of the shear tensor,

$$\begin{aligned} \gamma_1 &= \tfrac{1}{2}\left(\psi_{11} - \psi_{22}\right) = \gamma\cos 2\varphi, \\ \gamma_2 &= \psi_{12} = \psi_{21} = \gamma\sin 2\varphi. \end{aligned} \tag{2.20}$$

With these definitions, the Jacobian matrix can be written as

$$A = \begin{pmatrix} 1-\kappa-\gamma_1 & -\gamma_2 \\ -\gamma_2 & 1-\kappa+\gamma_1 \end{pmatrix}. \tag{2.21}$$

The meaning of the terms convergence and shear now becomes clear. Convergence acting alone causes an isotropic focusing of light rays, leading to an isotropic magnification of a source. The source is mapped onto an image with the same shape but larger size. It depends only on the distribution of mass inside the light beam. On the other hand, the contribution due to the mass distribution outside the light beam could be significant and it is described by the shear, which introduces anisotropy into the lens mapping; the quantity $\gamma = (\gamma_1^2 + \gamma_2)^{1/2}$ describes the magnitude of the shear and φ describes its orientation. As shown in Fig. 2.4, a circular source of unit radius becomes, in the presence of both κ and γ, an elliptical image with major and minor axis $(1-\kappa-\gamma)^{-1}$ and $(1-\kappa+\gamma)^{-1}$, respectively.

The magnification is

$$\mu = \frac{1}{detA} = \frac{1}{(1-\kappa)^2 - \gamma^2}. \qquad (2.22)$$

Since A is different for different multiple images, the image fluxes are different. In particular, if the image separation in a point mass lens system is substantially larger than $2\xi_0$, the secondary image is very strongly demagnified and thus invisible.

2.6 Critical curves

Formally, $detA$ can vanish for certain values of $\vec{x}$ in the lens equation: then the magnification factor diverges for those values. The sets of points in the lens plane for which this happens are called critical lines and the corresponding lines in the source plane are called caustics[3]. The number of images changes by ±2 if the source position crosses a caustic; then two images appear or merge.

For spherically symmetric mass distributions, the critical curves are circles. For a point lens, the caustics degenerate into a point. For elliptical lenses or spherically symmetric lenses plus external shear, the caustics can consist of cusps and folds. In Figs. 2.5 and 2.6 the caustics and critical curves for a Singular Isothermal Sphere, SIS, plus external shear galaxy model are computed. The SIS model for the mass distribution in a galaxy assumes that the stars and other mass components behave like particles of an ideal gas, confined by their combined, spherically symmetric gravitational potential. The mass distribution is $\kappa(x) = 1/(2x)$ and the deflection angle is $\alpha(x) = x/|x|$ (Schneider, Ehlers & Falco 1992). Since most galaxies are not isolated, but are part of a cluster which contains intracluster gas and dark matter, the environment of the galaxy can be modelled as an external shear.

In Fig. 2.5 the position of the point-like source with respect to the caustic and their respective lensing images on the lens plane have been calculated and represented. In Fig. 2.6 we compute the different positions of an extended

---

[3] Mathematically, the magnification factor becomes infinite, however the sources are extended (not point-like), so that the magnification has a finite value.

source with respect to the caustic when it is moving towards a fold or a cusp, and their respective lensing images with respect to the critical curves.

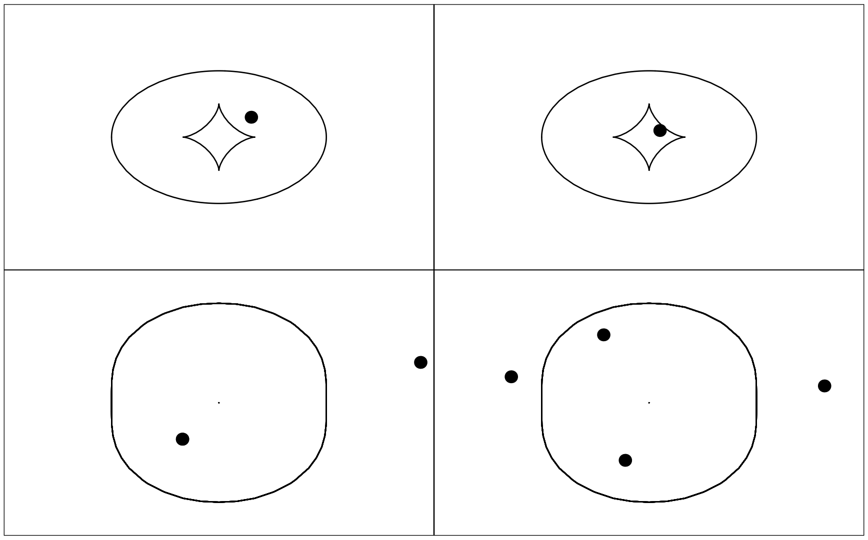

FIGURE 2.5— Imaging of a point source by a singular isothermal sphere plus an external shear lens. On the bottom panels the image positions and the critical lines are represented. On the top panels the source positions and the caustics are sketched. Notice that when the source crosses a caustic (top left-hand panel to top right-hand panel) two additional images appear (bottom left-hand panel to bottom right-hand panel).

Solving the lens equation, the position of the caustics for a given configuration can be calculated. For a low number of lenses ($n \leq 2$) this can be done analytically. When the number of lenses is high ($n > 2$), the distribution of caustics is more easily produced with inverse ray-shooting techniques, in which rays are traced backwards from the observer to the source through the distribution of lenses in the lens plane (Kayser, Refsdal & Stabell 1986; Schneider & Weiss 1987; Wambsganss 1990). In this way the two dimensional magnification distribution in the source plane is obtained. These distributions are called magnification patterns.

2.7 Simple lens model

A model of a gravitational lens system consists of describing mathematically the gravitational potential of the deflector, which can be a point-like ("Schwarzschild lens") or an extended mass distribution.

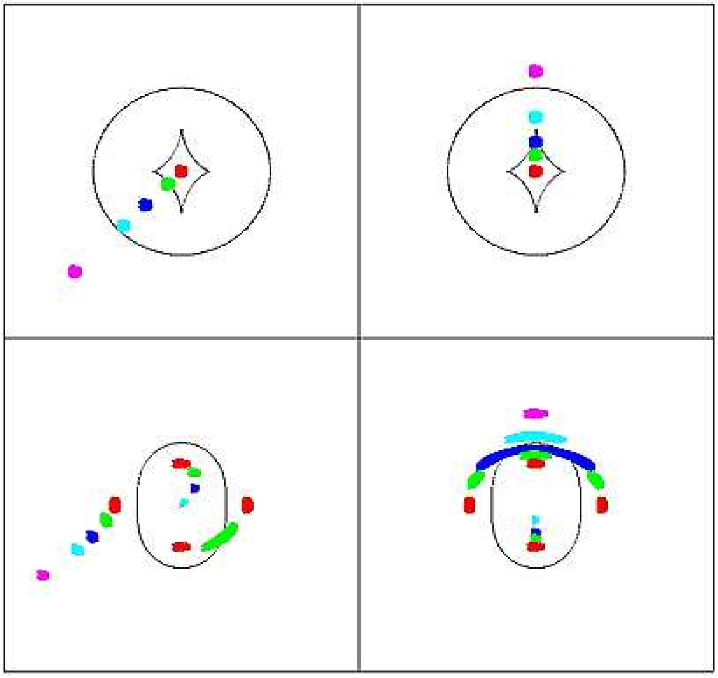

FIGURE 2.6— Imaging of an extended source at several locations (different colors) by a singular isothermal sphere plus an external shear lens. On the bottom panels the image positions and the critical lines are represented. On the top panels the source positions and the caustics are sketched. A source behind the center of the lens, inside the diamond formed by the caustic, has four images forming a cross-shaped pattern. When the source is moved towards a fold caustic (left-hand panels), two of the four outer images move towards each other, merge and disappear as the source approaches and then crosses the caustic. Just after the source has passed the fold caustic, the two merging images have totally disappeared. When the source moves towards a cusp point (right-hand panel), three images merge to form a single image, one luminous arc, whereas the fourth one appears as a faint image.

When a "point mass" is considered as a lens at the origin of a lens plane ($\vec{x} = 0$), the surface mass density is $\Sigma(\vec{x}) = M\delta^2(\vec{x})$, and the lens equation appears as,

$$\vec{y} = \vec{x}(1 - \frac{1}{x^2}), \tag{2.23}$$

which has two solutions

$$x_{1,2} = \frac{1}{2}\left(y \pm \sqrt{y^2 + 4}\right), \tag{2.24}$$

one image on each side of the lens. Since the amplification is $\mu = (1 - x^{-4})^{-1}$, the total magnification for a point source μ_p is

$$\mu_p = \frac{y^2 + 4}{y\sqrt{y^2 + 2}}. \tag{2.25}$$

The magnification of an extended source by a Schwarzschild lens is obtained by integrating μ_p over the source. If the source is a disc with radius R and uniform surface brightness, the maximum magnification is

$$\mu_{\max} = \frac{\sqrt{4 + R^2}}{R}. \tag{2.26}$$

In Fig. 2.7 we calculate how an extended source is lensed by a point-like lens. When the lens, the source and the observer are in the same optical path an "Einstein ring" is observed (left-hand panel), but when the alignment is not perfect, the Einstein ring disappears and two images become visible for each point in the extended source, one on each side of the lens.

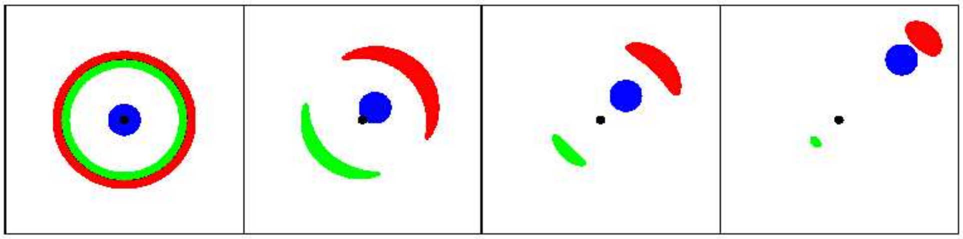

FIGURE 2.7— Imaging of an extended source by a point-like lens. The source is represented in blue, the lens is black, and the images of the lensed source are shown in red (x_1) and green (x_2). When the lens, the source and the observer are in the same optical path ($y = 0$), an "Einstein ring" is observed with $x = 1$, in η_0 units (left-hand panel). When the source moves away from the optical path ($y \neq 0$), the Einstein ring disappears and two images are drawn for each point in the extended source, $x_{1,2} = (y \pm \sqrt{y^2 + 4})/2$. The source radius is $0.25\eta_0$

However, in spite of the success of the Schwarzschild lens in describing several astrophysical scenarios, it is mandatory to consider the influence of the galaxy or galaxies around the isolated lens, distorting its gravitational field. In this case, the deflector is usually modelled either with an elliptical mass distribution or with a spherical mass distribution plus an external shear, because an external shear breaks the circular symmetry of a lens and it often has the same effect as introducing ellipticity in the lens (Kovner 1987).

2.8 Ray-shooting

The ray-shooting method, also known as the inverse ray-shooting method, is used to find the total magnifications for each image of a gravitational lens system by a large number of sources in the lens plane. Light rays are traced backwards from the observer to the source plane, on which the magnification pattern is calculated by collecting the rays. So, the number density of rays is proportional to the magnification. If a background source traverses the magnification regions due to either the motion of the source itself or the velocity dispersion of the stars associated with the lens galaxies, the apparent luminosity of the source will vary as a function of time (Kayser, Refsdal & Stabell 1986; Schneider & Weiss 1987; Wambsganss 1990; Wambsganss, Paczyński & Katz 1990).

The section where the image goes across the galaxy is characterized, on the one hand, by the surface mass density of the compact objects, κ_* and, on the other hand, by a shear term, γ, that includes the perturbing effect of the mass distribution of the lensing galaxy as a whole, together with the surface mass density of the interstellar matter, κ_c. The surface mass density or optical depth is $\kappa = \kappa_* + \kappa_\mathrm{c}$ (Kayser, Refsdal & Stabell 1986; Schneider & Weiss 1987; Wambsganss, Paczyński & Katz 1990)

The normalized lens equation for a field of point-like masses with an external shear, γ, and a smooth mass distribution, κ_c, where the coordinate frame has been oriented such that the shear acts along one of the coordinate axes, is (Schneider, Ehlers & Falco 1992)

$$\mathbf{y} = \begin{pmatrix} 1 - \kappa_\mathrm{c} + \gamma & 0 \\ 0 & 1 - \kappa_\mathrm{c} - \gamma \end{pmatrix} \mathbf{x} + \sum_{i=1}^{N_*} m_i \frac{(\mathbf{x} - \mathbf{x}_i)}{|\mathbf{x} - \mathbf{x}_i|^2}. \tag{2.27}$$

$\mathbf{x}$ and $\mathbf{y}$ are the normalized image and source positions, respectively, and $\mathbf{x}_i$ and m_i are the normalized positions and masses of the microlenses. Each lens is characterized by its mass and position, and the number of stars, N_*, depends on κ_* and the area of the lens plane, A_x, as $N_* = \kappa_* A_x / \pi$.

The ray-shooting method to compute all the magnification maps in this case (a field of point-like masses) can be described as follows. First, all lenses are randomly distributed on an area of the lens plane, $A_x = L_{x1} * L_{x2}$, and this area is mapped with a uniform grid of points x via the lens equation onto the source plane. The magnification map, with an area $A_y = L_y^2$ on the source plane, is divided into N_p^2 pixels, and the total magnification of each pixel is computed as the ratio of the number of rays that hit it, and the number it would contain in the absence of the lens (e.g. Schneider, Ehlers & Falco 1992).

If the deflecting mass distribution were smoothed out, a rectangle of sides L_{x1} and L_{x2} would be mapped onto the square in the source plane, with $L_{x1} = cte * L_y/(1-(\kappa_c+\kappa_*+\gamma))$ and $L_{x2} = cte * L_y/(1-(\kappa_c+\kappa_*-\gamma))$, with $cte = 1$. But due to the graininess of the deflector, a much larger area of the lens plane must be mapped onto the source plane (Schneider & Weiss 1987), $A_x > A_y$, with $cte \geq 1.5$.

2.9 Magnification patterns

This ray-shooting method is the technique used to develop all the magnification patterns which will be necessary to study the influence of microlensing at high optical depth. It is a very highly time-consuming technique because a large number of rays are traced between the observer and the source (aproximately 10^9 to 10^{11} rays). Bearing this in mind, our Fortran program was paralleled and sent to a cluster, composed by 150 PC's and 100 work-stations (SUNs), with Condor[4].

Caustic maps corresponding to one, two, three, four, eight and nine lenses are represented in Fig. 2.8. The positions of the lenses are fixed deliberately with an aesthetic purpose, except on the bottom right-hand panel where the positions are random. It is important to point out that when the number of lenses is increased, the complexity of the caustic structure increases as well. A high optical depth case is contemplated in Fig. 2.9, the magnification pattern of Q2237+0305C image with 1405 lenses placed randomly in the lens plane and taking into account an external shear. The parameters considered for the mass distribution and external component are (κ, γ)=(0.69,0.71) (Schmidt, Webster & Lewis 1998). This map covers an area of $16\eta_0 \times 16\eta_0$ at the source plane. It was computed covering an area of $80\xi_0 \times 80\xi_0$ in the lens plane, and was obtained at a resolution of 1000×1000 pixels. 256 rays were shot per unlensed pixel, which means $6.4 \cdot 10^9$ rays traced between the observer and the source. The number of stars was determined by supposing that the entire optical depth is in compact objects, $\kappa_c = 0$. The theoretical mean amplification $<\mu_{th}>= |(1-\kappa)^2-\gamma^2|^{-1}$ is 2.451, and the mean amplification of the map is 2.491.

In Fig. 2.10 it is possible to observe how one or several lenses could distort an image, depending on the number of lenses, their masses or positions. On the top right-hand panel a very massive microlens placed in the center of the image is considered. On the bottom left-hand panel ten microlenses with small mass

---

[4] Condor is developed by the Condor Team at the University of Wisconsin-Madison, and it is a specialized batch system for managing compute-intensive jobs. Like most batch systems, Condor provides a queuing mechanism, scheduling policy, priority scheme, and resource classifications.

are placed randomly, and on the bottom right-hand panel twelve microlenses with predetermined positions and small mass are used.

The longest developed magnification pattern needed one month in the Condor queue to be computed, with the parameters being: (κ,γ)=(0.39,0.64), $\kappa_c = 0.2\kappa$, 9000 stars, $3.6 \cdot 10^{11}$ rays traced from an area of $600\xi_0 \times 600\xi_0$ in the lens plane to an area of $16\eta_0 \times 16\eta_0$ in the source plane, with 1000×1000 pixels. The theoretical mean amplification of the pattern is $< \mu_{th} >= 23.261$ and the mean amplification is 20.708.

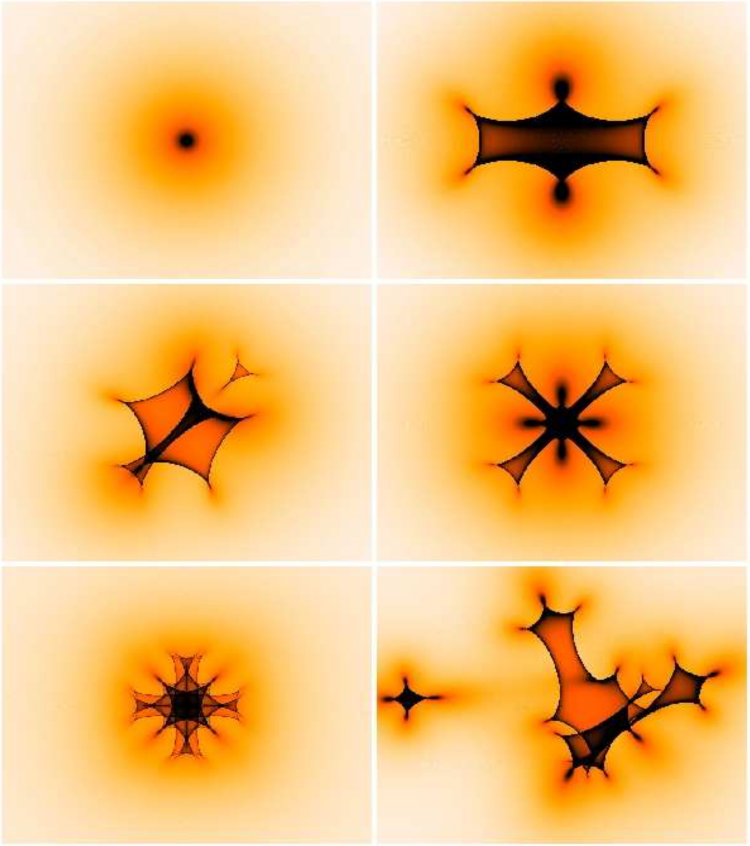

FIGURE 2.8— Six different magnification patterns are represented, for one (top left-hand panel), two (top right-hand panel), three (middle left-hand panel), four (middle right-hand panel), eight (bottom left-hand panel) and nine (bottom right-hand panel) lenses, without including external shear. The positions of the lenses are fixed deliberately with an aesthetic purpose, except on the bottom right-hand panel where the positions are random.

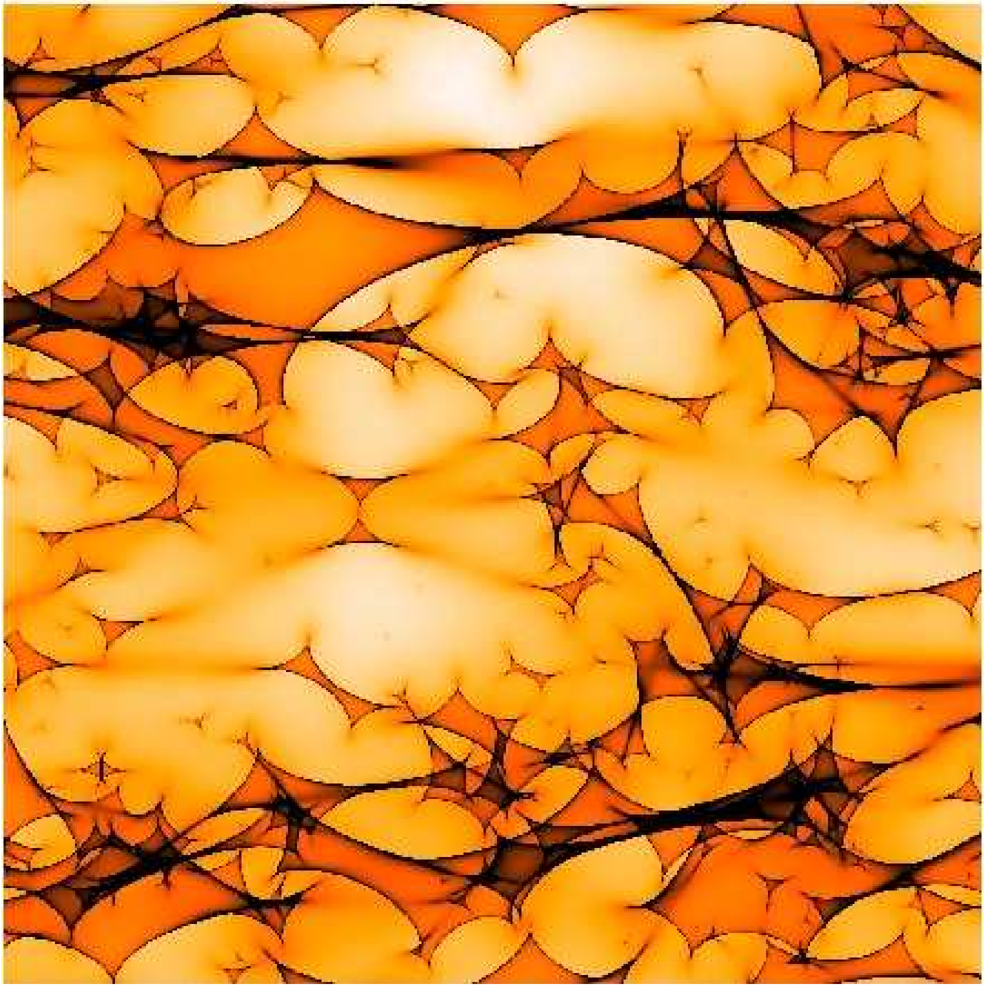

FIGURE 2.9— The magnification pattern of Q2237+0305C image for high optical depth with an external shear is shown (see text for details).

2.10 Summary

Once the theory of gravitational lensing has been introduced, and fundamental parameters such as the lens equation, the deflection angle, the magnification, the convergence or the shear are stated, and taking into account the general ideas about AGN on §1, we have the essential tools to begin to study the influence of gravitational microlensing on the broad emission lines of AGN.

FIGURE 2.10— Logo of the Instituto de Astrofísica de Canarias (top left-hand panel) suffering the gravitational lens effect. On the top right-hand panel this logo is affected by a massive lens. On the bottom right-hand panel this logo is affected by several lenses, of which the positions are fixed. On the bottom left-hand panel, the lenses are randomly located.

3

Microlensing by an isolated lens

> *No puedo cambiar la dirección del viento*
> *pero sí ajustar mis velas*
> *para llegar siempre a mi destino.*
> Jimmy Dean

3.1 Introduction

THE change in the continuum flux of quasars by stars or compact objects in intervening galaxies (gravitational microlensing) is now a well-established observational phenomenon (Wambsganss, Paczyński & Schneider 1990; Rauch & Blandford 1991; Gould & Miralda-Escude 1997; Wyithe et al. 2000; Yonehara 2001). Several studies have attempted to resolve the structure of the region generating the optical and UV continuum by using the microlensing effect as a gravitational telescope (see Yonehara et al. 1999, and references therein). However, as was mentioned in §1.1.3, it has usually been assumed that the size of the region generating the broad emission lines of quasars is too large (0.1–1 pc within the framework of the standard model, Rees 1984) to be substantially affected by stellar-mass lenses. According to previous studies (Nemiroff 1988; Schneider & Wambsganss 1990), by comparing one line in different components of a multiple-imaged quasar we would be able to detect only fractional deviations of the lensed from the unlensed profile. Even using optimistic estimates for the microlens masses, these deviations would amount to a modest 10–30% range. Nevertheless, new results concerning the BLR structure and kinematics are relevant to these studies, and could substantially change the common view about the expected influence of microlensing events on the BEL profiles. A recent study (Wandel, Peterson & Malkan 1999) that compares the BLR size determinations obtained using both the reverberation and the photoionization techniques (see §1.1.3 for a description of both methods) for a sample of 19 low luminosity AGN (mainly Seyferts) inferred a size in the range of a few light days to a few light weeks. For AGN of greater luminosity (QSOs) Kaspi et al. (2000) derived sizes from the Balmer lines in the range from 13 to 514 light days, finding a global scaling of the BLR size as a function of the intrinsic luminosity, $r_{\rm blr} \propto L^{0.7}$.

In this chapter the influence of microlensing by an isolated lens on the BELs will be revisited by incorporating these new results (Abajas et al. 2002). In §3.2 the possibilities of microlensing on the BLR of different known multiple-image quasars are estimated. In §3.3 we use simple, but not kinematically unrealistic, models of BLRs to study qualitatively the effects that microlensing can produce on the line profiles. In §3.4 the observational implications and applications will be discussed. Finally, the main conclusions are summarized in §3.5.

3.2 Estimates for some known systems of multiple image QSOs

Only extended objects of sizes comparable to or smaller than the Einstein radius associated with the gravitational lens will experience appreciable amplifications (e.g., Schneider, Ehlers & Falco 1992). Thus, in the framework of the AGN standard model where the BLR is supposed to have a radius in the 0.1–1 pc range, only massive deflectors could give rise to significant amplifications. On the other hand, recent results from the MACHO project indicate that the most likely microdeflector masses in the Galactic halo are in the range 0.15–0.9 $M_\odot$ (Alcock et al. 2000b). In the Galactic bulge the microdeflector masses are in good agreement with normal-mass stars (Alcock et al. 2000a). Estimates from the light-curve of Q 2237+0305 (Wyithe, Webster & Turner 2000) are also in reasonable agreement with these values. Consequently, significant amplifications of the BEL would not be expected according to the standard model. This result has been pointed out by other authors (Nemiroff 1988; Schneider & Wambsganss 1990), even if they were somewhat optimistic concerning the distribution of the microlens mass adopted.

However, recent research on the BEL seems to indicate that the BLR could be substantially smaller than expected in the standard model (Wandel et al. 1999). Based on the idea that 'the continuum/emission line cross-correlation function measures the responsivity-weighted radius of the BLR (Koratkar & Gaskell 1991)', Wandel et al. (1999) have obtained reliable size measurements. The sizes obtained using this technique (reverberation mapping) are consistent with the substantially more extensive but less accurate measurements inferred from the photoionization method. The results summarized by Wandel et al. (1999) exhibited a large scatter (from 1.4 to 107 days) which could be attributed to: i) the different size/structure of the BLR in different objects, and ii) the different sizes of the regions associated with emission lines of different degrees of ionization. The latter possibility has been neatly exemplified in the case of NGC 5548, in which luminosity-weighted radii ranging from $\sim$ 2.5 days for the He II λ1640 line to the 28 days corresponding to the [C III] λ1909 line have been found (Peterson & Wandel 1999). NGC 5548 and the other objects in the sample of Wandel et al. (1999) are AGN of relatively low luminosity. Nevertheless, there is a wide range of luminosities among the lensed QSOs. To take this fact into account the relationship between the BLR size and the intrinsic luminosity of the AGN (Kaspi et al. 2000) is used.

3.2.1 Search for candidates

For a typical lens configuration ($z_{\rm l} = 0.5$ and $z_{\rm s} = 2$), the projected Einstein radius of the microlens on the source is $\eta_0 \sim 20(M/M_\odot)^{(1/2)}$ light-days (for a $\Omega_{\rm M} = 0.3$ flat cosmology and $H_0 = 70$ km s^{-1} Mpc^{-1})[1]. Objects with $r_{\rm blr} \lesssim \eta_0$ are significantly affected by microlensing. So the relevant question is whether in the sample of the $\sim$ 70 known gravitational lens systems there exist some lensed quasars with BLR radius $r_{\rm blr} \lesssim \eta_0$. To answer this question we can apply the relationship $r_{\rm blr} \propto L^{0.7}$ (Kaspi et al. 2000) using NGC 5548 as a reference object. We adopt two values for the BLR size of NGC 5548 in order to account for its stratification: 21.2 light-days (Balmer lines, Kaspi et al. 2000) and 2.5 light-days (high ionization, He II line, Peterson & Wandel 1999). One can straightforwardly verify that a $z = 2$ quasar with $m_V = 24.3$ (or a quasar with $z = 1$ and $m_V = 22.5$) would have the same $r_{\rm blr}$ as NGC 5548, i.e. the microlensing on the BLR would be quite pronounced. Multiple-image objects of this apparent magnitude can be detected and, in fact, there are several examples among the currently known gravitational lens systems.

We can refine this rough estimate by taking into account the redshift and apparent magnitude of each lensed object. With this aim, in Fig. 3.1 we show contour plots of the BLR radius as a function of the source redshift and apparent magnitude using both reference values for the BLR of NGC 5548 and the $r_{\rm blr} \propto L^{0.7}$ law. We have also included in Fig. 3.1 the observed redshift–magnitude values corresponding to a sample of 31 QSOs selected from the $\sim$ 70 known

---

[1] This projected Einstein radius is calculated using Eq. 2.6. The angular diameter distances involved in the equation are computed in Appendix A using the Friedmann cosmology (Eqs. A.13 and A.15).

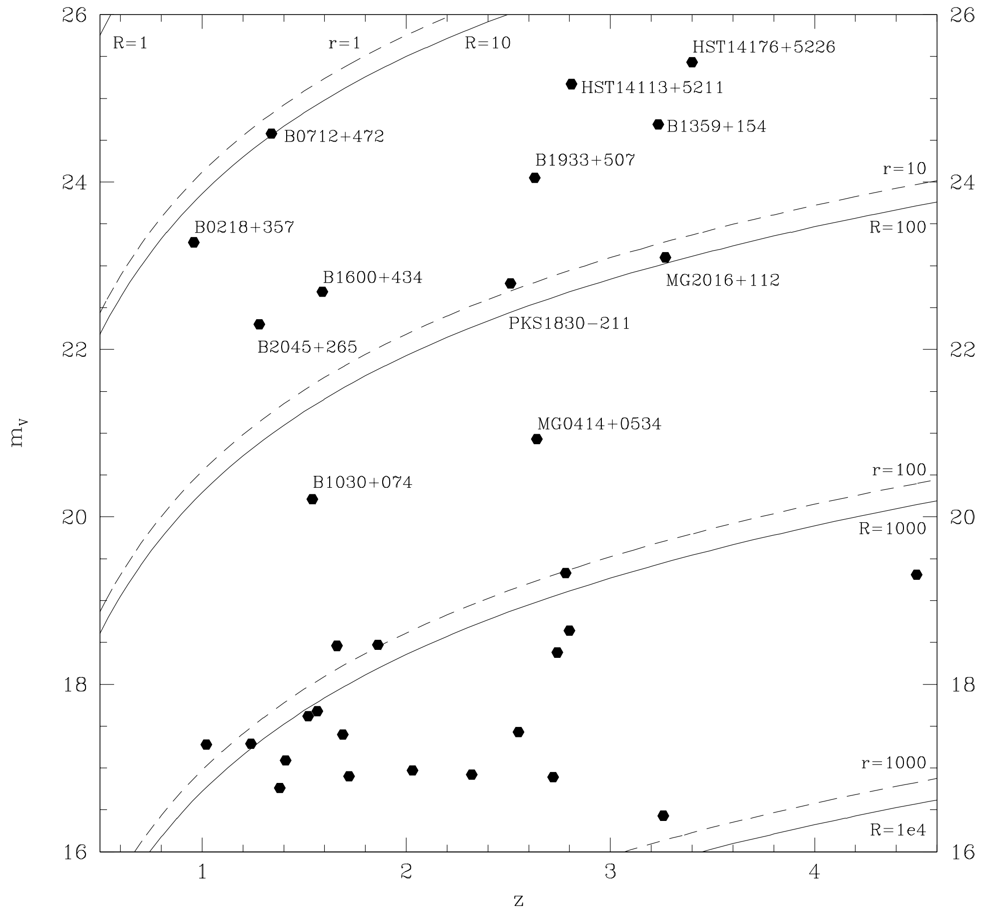

FIGURE 3.1— Contour plots of the BLR radius (in light-days) as a function of source redshift and apparent magnitude using both reference values for the BLR of NGC 5548 (R when $r_{\rm BLR}$(NGC 5548) = 21.2 light-days and r when $r_{\rm blr}$(NGC 5548) = 2.5 light-days) and the Kaspi et al. 2000 relationship $r_{\rm blr} \propto L^{0.7}$ (for an $\Omega = 0.3$ flat cosmology and $H_0 = 70$ km s^{-1} Mpc^{-1}). Points represent a sample of 31 QSOs whose redshift–magnitude values have been observed. No extinction or amplification corrections are taken into account.

gravitational lenses with the criteria of having the lens and source redshifts and the optical magnitude well determined. We have used the V magnitude of the brightest lensed image (in B 1933+507, B 2045+265, MG 0414+0534, PKS 1830-211 and another four unlabeled objects we have inferred V from I using $V - I = 0.50$; in HST 1413+5211 and another unlabeled object we have inferred

V from R using $V - R = 0.11$). The data have been mainly obtained from the CASTLES web page (http://cfa-www.harvard.edu/castles). For the previous and subsequent calculations we have adopted the optical magnitude and redshift of NGC 5548, $m_V = 13.3$ and $z = 0.017$ from the NASA Extragalactic Database (NED). To transform apparent magnitudes, m, into intrinsic luminosities we have made use of the equation $L = 4\pi D_{\rm lum}^2 S(1+z)^{(\alpha-1)}$ (Lang 1980), which relates the absolute luminosity of the source, the luminosity distance, $D_{\rm lum}$, the apparent flux, $S = 10^{-0.4m}$, and the spectral index, α, defined by a power law of the spectral flux density as $F_\nu \propto \nu^{-\alpha}$ (Netzer 1990; Robson 1996; Krolik 1999). We have considered an $\Omega = 0.3$ flat cosmology and a value for the spectral index $\alpha = 0.5$ (e.g., Richards et al. 2001).

In Figure 3.1 we can identify a group of ten systems with magnitude $m_V > 21$ that would lie in the region $R \lesssim 100$ light-days (Balmer lines) and in the region $r \lesssim 10$ light-days (high-ionization lines, HILs). These systems are possibly affected by microlensing, with particular strength in the case of the HILs. However, the observed magnitudes of the lensed QSOs should be corrected by extinction and gravitational lens amplification. The amount of extinction in the gravitational lenses is unknown for most of them, but it can be in the range from dust-free lenses to strongly reddened systems (e.g., Falco et al. 1999; Muñoz et al. 2001 and references therein). We selected the magnitude from the brightest QSO image, which in most of the cases is the less reddened. As a first approximation to the expected amount of obscuration we can adopt the mean extinction, $\langle \Delta m \rangle = 0.6$, derived by Falco, Kochanek & Muñoz (1998) comparing the statistics of radio and optical lensed quasars. On the other hand, the quasar source is amplified by the gravitational lens and the true luminosity of the unlensed quasar should be calculated by fitting a lens model to each system. The exact amplification of each gravitational lens system depends on the lens model and on the particular configuration of the system, but an average expected amplification between the brightest image and the unlensed source is ~ 1.5 mag (e.g., Lehár et al. 2000). Thus, a roughly averaged correction of the combined effects of extinction and lens amplification can be made by adding ~ 1 mag to the apparent QSO magnitude.

Taking into account the +1 mag shift, the number of possible candidates affected by microlensing (at least in the HILs) is increased to 12 ($\sim 40\%$ of the sample, see Fig. 3.1). Our selection procedure could include not only intrinsically low-luminosity but also reddened objects in the list of candidates. As we have seen, a 1 mag shift due to underestimation of the extinction will not substantially modify the set of candidates. This moderates the impact of the extinction uncertainties in the selection of candidates, but we cannot discard the possibility that our statistics were biased by heavily reddened objects of intrinsically high luminosity. This is the case for B 0218+357, which according to the rest-frame $E(B-V)=1.52$ obtained from Falco et al. (1999) would be an intrinsically high-luminosity object reddened by extinction. MG 0414+0534 is also a very reddened object, but in this case probably owing to a very red intrinsic spectral distribution ($F_\nu \propto \nu^{-9}$ was measured at optical wavelengths by Hewitt et al. 1992). This implies that MG 0414+0534 could have a high intrinsic rest-frame V luminosity but also indicates that this object is probably a radio galaxy rather than a QSO.

The identification of the candidates available in the literature supports the hypothesis that most of them are intrinsically low-luminosity objects, since in most cases the objects cannot be clearly classified as bright QSOs but admit alternative classifications as objects with lower levels of activity (radio galaxies, underluminous QSOs, starburst galaxies, Seyfert 2 galaxies, or other types of AGN). This also implies that we have probably overestimated the luminosities of the candidate objects because we have not removed the contribution from the galaxy, which is probably far from negligible.

3.2.2 Estimate of the amplification in B 1600+434

It would be very useful to compute the expected amplifications for each object in the list of candidates. However, lack of knowledge of the extinction in each system and, to some extent, of a precise classification of the source, could affect the results significantly. We have selected the gravitational lens discovered by Jackson et al. (1995), B 1600+434, a double-imaged typical quasar at $z_{\rm s} = 1.59$, lensed by an edge-on spiral galaxy at $z_{\rm l} = 0.42$, in which both the lens amplification and the extinction might be reasonably well known. To calculate the amplification induced in B 1600+434 by the lens galaxy we have fitted a singular isothermal ellipsoid (SIE)[2] to this double-imaged quasar. Thus, we obtain an amplification of 0.96 mag for the brightest quasar image, which has an observed V-band magnitude of $m_V = 22.69$. For the extinction we have used the result from Falco et al. (1999), $A_V = 1.02$ mag. From the intrinsic luminosity obtained after correcting for amplification and extinction ($m_V = 22.63$) and using the Kaspi et al. relationship, we have estimated radii of 45 and 5.3 light-days for the Balmer and He II BLRs, respectively (according to the two values of reference adopted for NGC 5548).

---

[2] The singular isothermal ellipsoid is a generalization of the singular isothermal sphere, whose mass distribution is $\kappa = 1/(2x')$, with $x'^2 = (q^2x_1^2 + x_2^2)/(1-\epsilon)^2$. x' is constant on ellipses with axis ratio $q = (1-\epsilon)/(1+\epsilon)$. When the ellipticity $\epsilon = 0$, both models are equivalent. This lens model has been considered in some detail in Kassiola & Kovner (1993) and Kormann, Schneider & Bartelmann (1994).

To estimate the maximum amplification, $\mu_{\rm max}$, we adopt the expression (e.g., Schneider et al. 1992):

$$\mu_{\rm max} \sim \frac{\sqrt{(\frac{r_{\rm blr}}{\eta_0})^2+4}}{(\frac{r_{\rm BLR}}{\eta_0})}, \tag{3.1}$$

where $r_{\rm blr}$ is the BLR radius, and η_0 is given by Eq. 2.6.

If we apply these formulae to B 1600+434, we find that a solar-mass stellar microlens would induce a modest, albeit potentially observable, amplification of 1.4 in the Balmer lines and a strong amplification of 8.2 in He II. A 0.1 $M_{\odot}$ microlens would also induce an appreciable amplification of 2.76 in the He II lines. We do not calculate the amplification by microlensing on the BEL for the other objects in the list because the exact amount of extinction is unknown for most of them, and because we can no longer suppose that the $F_\nu \propto \nu^{-0.5}$ dependence of the energy distribution is a realistic approach for some of the objects.

In summary, although most of the lensed quasars ($\gtrsim$ 70% of the total) are intrinsically high-luminosity quasars (so that no strong microlensing on the BEL is expected) we found that $\lesssim$ 30% of the lensed sources are faint enough to be considered as possibly affected by microlensing on the BEL.

3.3 Microlensing effects on the profile of the broad emission lines

When an organized velocity field governs the kinematics of the BLR, microlensing can give rise to a selective amplification of the emission line profile (Nemiroff 1988). The shape of the line depends on the location of the source with respect to the optical axis (defined by the observer and the microlens) and can change with the relative movement between the microlens and the BLR. In this section we adopt the kinematic models for the BLR used by Robinson (1995) to study the range of profile shapes that exists among AGN in the context of a simple parameterization of some basic properties of the BLR such as the emissivity and the velocity law. Our intention is to study, in this framework, the effects induced in the line profile by a microlens in different locations with respect to the center of the BLR.

We assume that a single microdeflector is affecting the BLR. A more realistic approach based on the existence of a random distribution of microdeflectors will be analyzed in §5.

In accordance with Robinson (1995), we consider three different geometries (spherical, biconical and cylindrical) and adopt the following radial dependences for the emissivity:

$$\epsilon(r) = \epsilon_0 \left(\frac{r}{r_{\rm in}}\right)^{\beta}, \tag{3.2}$$

and the magnitude of the velocity:

$$v(r) = v_0 \left(\frac{r}{r_{\rm in}}\right)^{p}. \tag{3.3}$$

We adopt inner ($r_{\rm in}$) and outer ($r_{\rm blr}$) radii for the BLR.

The emission line profile can be computed from the expression

$$F_\lambda = \int_V \epsilon(r)\ \delta\left[\lambda - \lambda_0\left(1 + \frac{v_{||}}{c}\right)\right]\ \mu(\vec{r})\ dV, \tag{3.4}$$

where

$$\mu(\vec{r}) = \frac{u^2+2}{u\sqrt{u^2+4}}, \quad \left(u = \frac{|\vec{r}-\vec{r}_0|}{\eta_0}\right) \tag{3.5}$$

is the amplification associated with the microlens, $\vec{r}_0 \sim (r_0, \varphi_0)$ is the position of the microlens, η_0 is the Einstein radius and $v_{||}$ is the projected line-of-sight velocity.

Line profiles without amplification are shown in Fig. 3.2 for each considered geometry in this context (see also Robinson 1995).

It is convenient to scale the distances to the Einstein radius associated with the microlens. In this way, the relevance of the microlens effect can be characterized by the quantity

$$\tilde{r}_{\rm BLR} = \frac{r_{\rm blr}}{\eta_0}. \tag{3.6}$$

We consider two values (1 and 4) for $\tilde{r}_{\rm BLR}$ to study strong and mild magnification effects. The ratio between the inner and outer radii is a controversial issue and can change from one system to another. Thus, we simply assume that the inner radius is one order of magnitude smaller than the outer radius, $r_{\rm in} = 0.1\ r_{\rm blr}$.

To study the effects produced by the relative off-centering between the microlens and the BLR, we compute line profiles corresponding to a grid of displacements of the microlens relative to the center of the BLR. We consider 25 positions in the positive XY quadrant ranging from 0 to $\tilde{r}_{\rm BLR}$ in both the X and Y axes (Fig. 3.3).

The initial program language used to compute the line profiles in this chapter is Mathematica, a useful and intuitive graphic environment. However, the biconical model for intermediate inclinations became a highly time-consuming

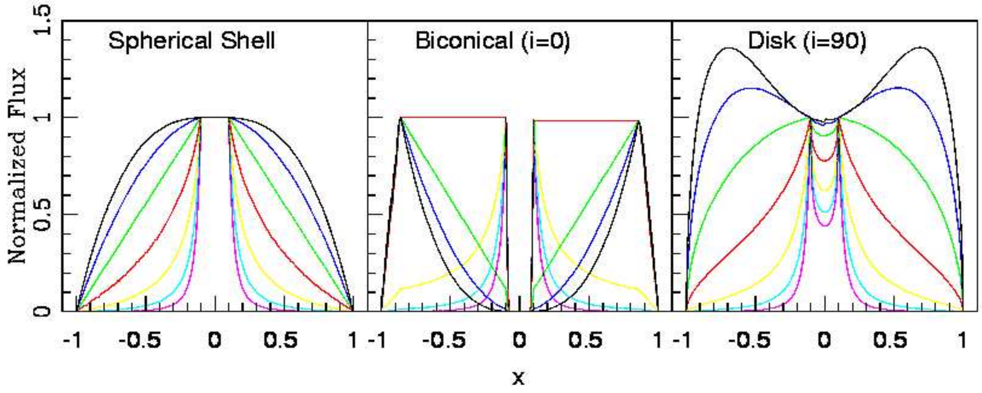

FIGURE 3.2— Line profiles for each model described in the text: spherical (left panel), biconical (middle panel) and cylindrical (right panel) shell. On the x-axis $x = c(\lambda - \lambda_0)/(v_{\max}\lambda_0)$ is represented whilst the normalized flux, F_x, is represented on the y-axis. Each family of profiles corresponds to different values of the wing curvature parameter η. This parameter is $\eta = (\beta + 3 - p)/p$ for the spherical and biconical shell, and $\eta = (\beta + 2 - p)/p$ for the cylindrical shell. The cone half-angle used in the biconical model is $\theta_c = 30°$. The values of η for each model are: -3 (color line: magenta), -2 (cyan) , -1 (yellow), 0 (red), 1 (green), 2 (blue), 3 (black). The core width parameter is fixed, $x_m = 0.1$, with $x_m = (r_{in}/r_{blr})^p$.

program. Thus, the program language was changed to Fortran. All line profiles in the next chapters are calculated with Fortran and represented with SuperMongo.

In the Appendix B we collect all the formal development and formulae and concentrate on the results in the following sections.

3.3.1 Spherical shell

In the case of a spherical ensemble of emitters flowing radially, the projected line-of-sight velocity corresponding to an emitter at a position (r, θ) is given by

$$v_{\|} = v_0 \left(\frac{r}{r_{\rm in}}\right)^p \cos\theta \quad (p > 0)\,. \tag{3.7}$$

We have used the same notation as Robinson (1995) for the parameters related to the relative velocity,

$$x = \frac{\lambda - \lambda_0}{\lambda_0}\frac{c}{v_{\rm max}}, \tag{3.8}$$

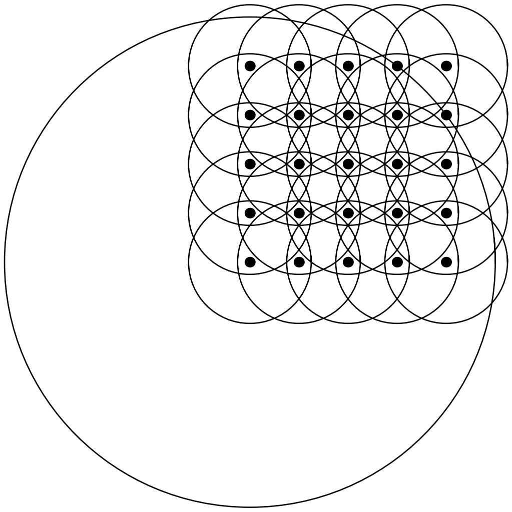

FIGURE 3.3— Grid of relative displacement between the microlens and the BLR. The large disc represents the BLR. The small discs correspond to the Einstein circle associated with the microlens, represented by a point, in the case $\eta_0 = r_{\rm blr}/4$. For each point (corresponding to a displacement of the microlens in the positive quadrant) we compute an emission line profile.

and we refer to the line parameter that defines the line shape:

$$\eta = \frac{\beta + 3}{p} - 1. \tag{3.9}$$

The line profile (see Appendix B.1) is obtained by integrating

$$F_x = \begin{cases} \frac{\epsilon_0 r_{\rm int}^2 c}{\lambda_0 v_0} \int_0^{2\pi} \int_{{\rm Max}[r_{\rm in}, r_{\rm lim}]}^{r_{\rm blr}} \left(\frac{r}{r_{\rm in}}\right)^{\beta+2-p} [\mu(x, r, \varphi)]_{f=0} dr d\varphi & \\ & \text{for } r_{\rm lim} < r_{\rm blr}, \\ 0 & \text{for } r_{\rm lim} > r_{\rm blr}, \end{cases} \tag{3.10}$$

where $r_{\rm lim} = r_{\rm in}\ (x/x_{\rm m})^{1/p}$, $x_{\rm m} = v_0/v_{\rm max} = (r_{\rm in}/r_{\rm BLR})^p$, and $[\mu(x, r, \varphi)]_{f=0}$ is given by Eq. 3.5, inserting Eq. B.9 into Eq. B.11.

Following Robinson (1995), we take η as the parameter defining the emission-line profile. For the spherical case we consider two values, 1) $\eta = 2$ and 2) $\eta = -0.25$, which in absence of microlensing would correspond to concave and convex profile wings, respectively. In absence of microlensing, only this parameter is needed to characterize the line profile. In the presence of microlensing we need also to fix another parameter. We select the emissivity exponent

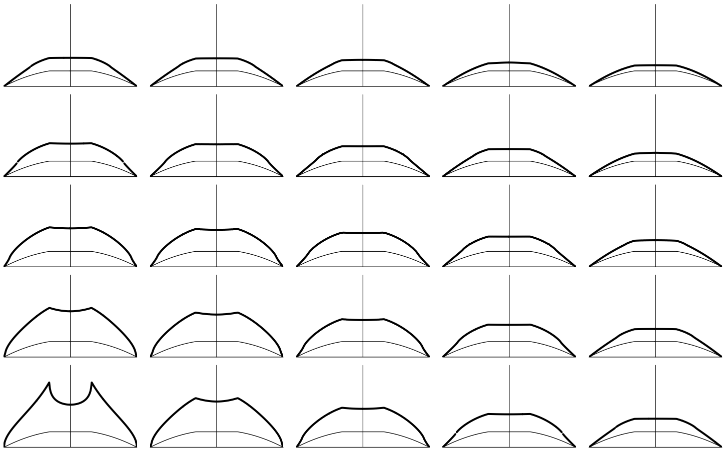

FIGURE 3.4— Spherical model with $p = 0.5$, $\beta = -1.5$, and $\eta_0 = r_{\rm blr}$. On the x-axis we represent $x = c\,(\lambda - \lambda_0)/(v_{\rm max}\lambda_0)$, which varies between -1 and 1. On the y-axis we represent the flux. The heavy solid line is the amplified line profile and the solid line is the unamplified line profile.

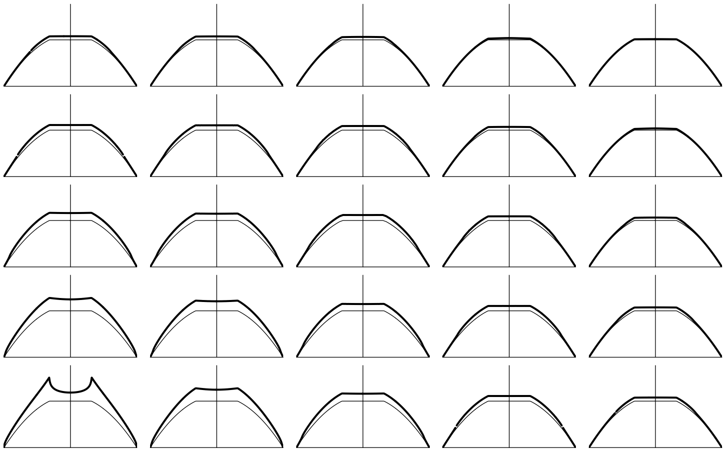

FIGURE 3.5— The same as in Fig. 3.4, but for $\eta_0 = r_{\rm blr}/4$.

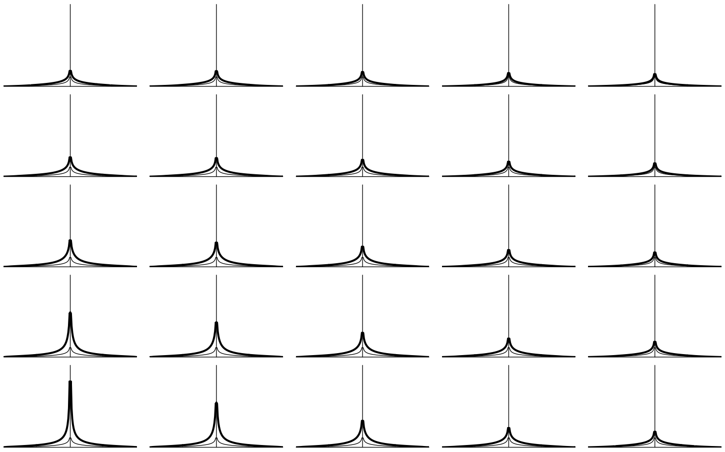

FIGURE 3.6— Spherical model with $p = 2$, $\beta = -1.5$, and $\eta_0 = r_{\rm blr}$. On the x-axis we represent $x = c\,(\lambda - \lambda_0)/(v_{\rm max}\lambda_0)$, which varies between -1 and 1. On the y-axis we represent the flux. The heavy solid line is the amplified line profile and the solid line is the unamplified line profile.

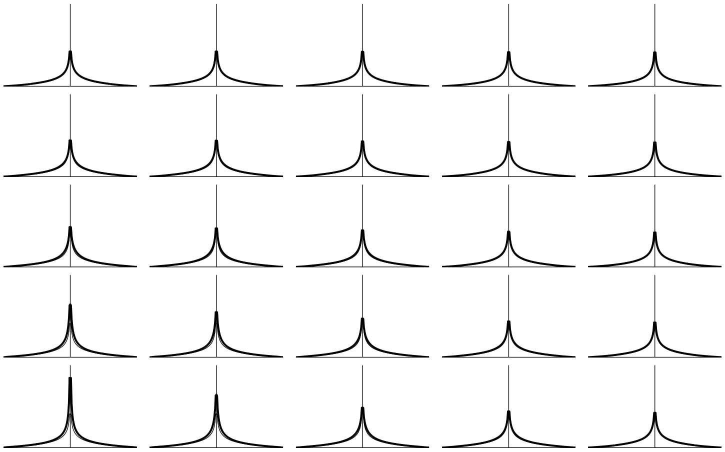

FIGURE 3.7— The same as in Fig. 3.6, but for $\eta_0 = r_{\rm blr}/4$.

$\beta = -1.5$ (see Eq. 3.2). The exponent of the velocity law, p, is then obtained from Equation 3.9. Thus, for case 1) we have $p = 0.5$ and for case 2) $p = 2$.

We present the grids of profiles for $\tilde{r}_{\rm BLR} = 1$ and 4 in Figures 3.4 and 3.5 for case 1) and in Figures 3.6 and 3.7 for case 2). The influence of microlensing on the line profiles would be observable when the microlens is centered on the BLR, and also in many other cases in which the microlens is off-centered. The displacement of a microlens across the BLR would induce changes in the relative strength of different parts of the line profile, relatively enhancing the wings when the microlens is centered on the BLR and the core when it is sited in the outer parts. However, no relative enhancements between the blue and red parts of the profile would appear due to the high symmetry of the spherical model.

As mentioned previously, one notable property of Robinson's models is that the profile shape depends only on η. This implies that from the study of the line profile it is not possible to derive direct information on the velocity field or the emissivity law. Could the presence of microlensing break this degeneracy for a spherical shell? Such questions as the existence of a monotonically increasing or decreasing dependence with radial distance of the velocity field may have a formal answer. In principle, it would be possible to invert the line-profile expression (Eq. 3.10) obtained for several different positions of the microlens to recuperate, making suitable suppositions, the law for radial velocities. Nevertheless, it is not easy to decide on direct observational criteria to carry out this study.

To illustrate the difficulties in deriving information from the microlensed line profile in the spherical case, notice that not even a simple question like the existence of outflow or inflow can be answered. (For the spherical case there is always the same contribution of receding and approaching emitters along the line of sight which would undergo the same magnification.)

3.3.2 Biconical shell

Much observational evidence (Zheng, Binette & Sulentic 1990; Marziani, Calvani & Sulentic 1992) and theoretical work (Goldman & Bahcall 1982) supports the idea that the flow of emitting gas is anisotropic, preferentially confined to a pair of oppositely directed cones. In this model we need three polar coordinates (r, θ, φ) measured with respect to the cone axis to express the projected line-of-sight velocity corresponding to an emitter,

$$v_{||} = v_0 \left(\frac{r}{r_{\rm in}}\right)^p \xi \quad (p > 0), \tag{3.11}$$

$$\xi = \sin\theta \sin\varphi \sin i + \cos\theta \cos i, \tag{3.12}$$

where i is the inclination of the cone axis with respect to the line of sight.

This model can give rise to a variety of line profiles (see Fig. 3.8). We consider the two limiting cases: $i = 0°$ and $i = 90°$, and an intermediate case: $i = 45°$. We adopt the cone half-angle $\theta_c = 30°$, and $\beta = -1.5$.

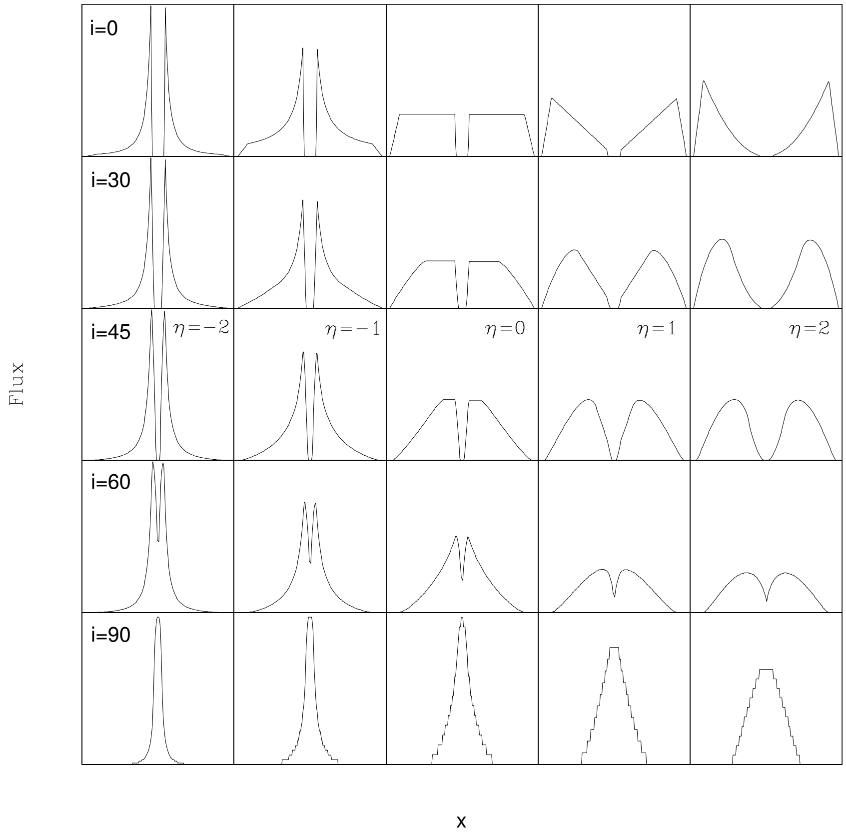

FIGURE 3.8— Part of a two-parameter grid, showing the variation of line profile shapes with the wing curvature (η) and axial inclination (i) for the biconical model. The inclination varies from $i = 0°$ (axis aligned with the line of sight) to $i = 90°$ (axis perpendicular to the line of sight). The core width parameter is fixed, $x_m = 0.1$. The cone half-angle is $\theta_c = 30°$. This is the Figure 5 of Robinson (1995).

$i = 0^\circ$

The line profile (see Appendix B.2.1) is obtained by integrating

$$F_x = \begin{cases} \frac{\epsilon_0 r_{\mathrm{int}}^2 c}{\lambda_0 v_0} \int_0^{2\pi} \int_{\mathrm{Max}[r_{\mathrm{lim}}, r_{\mathrm{in}}]}^{\mathrm{Min}[r_{\mathrm{sup}}, r_{\mathrm{blr}}]} \left(\frac{r}{r_{\mathrm{in}}}\right)^{\beta+2-p} [\mu(x, r, \varphi)]_{f=0} dr d\varphi & \\ & \text{for } r_{\mathrm{lim}} < r_{\mathrm{blr}} \text{ and } r_{\mathrm{sup}} > r_{\mathrm{in}}, \\ 0 & \text{in the other cases,} \end{cases} \tag{3.13}$$

where $r_{\mathrm{lim}} = r_{\mathrm{in}} \left(|x|/x_{\mathrm{m}}\right)^{1/p}$, $r_{\mathrm{sup}} = r_{\mathrm{BLR}} \left(|x|/\cos\theta_{\mathrm{c}}\right)^{1/p}$, and $[\mu(x, r, \varphi)]_{f=0}$ is given by Eq. 3.5, inserting Eq. B.9 into Eq. B.11, with $x_{\mathrm{m}} = v_0/v_{\mathrm{max}} = (r_{\mathrm{in}}/r_{\mathrm{blr}})^p$.

In Figures 3.9 and 3.10 we present the grids of profiles for $\tilde{r}_{\mathrm{BLR}} = 1$ and 4 corresponding to $\eta = 2$, and in Figures 3.11 and 3.12 the grids corresponding to $\eta = -0.25$. In both cases we obtain two-peaked profiles. As in the case of the sphere, the influence of microlensing when the microdeflector is centered with the BLR is very noticeable. However, in the biconical case, the change in the relative enhancements of different parts of the line profile caused by the displacement of the microlens with respect to the center of the BLR is more noticeable than in the spherical one.

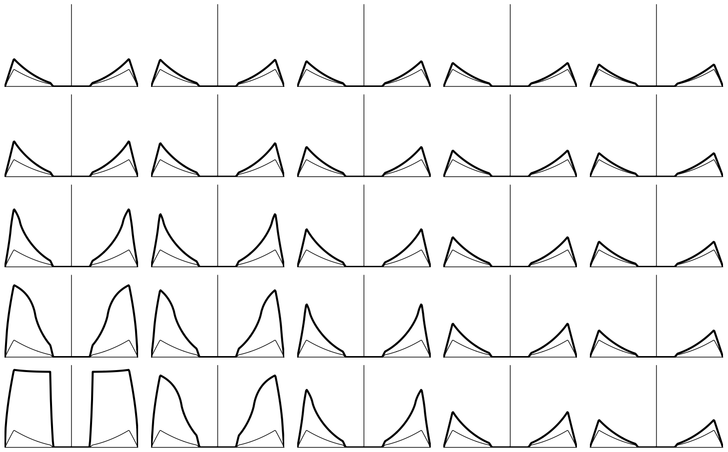

FIGURE 3.9— Biconical model with $i = 0^\circ$, $p = 0.5$, $\beta = -1.5$, and $\eta_0 = r_{\mathrm{blr}}$. On the x-axis we represent $x = c\ (\lambda - \lambda_0)/(v_{\mathrm{max}}\lambda_0)$, which varies between -1 and 1. On the y-axis we represent the flux. The heavy solid line is the amplified line profile and the solid line is the unamplified line profile.

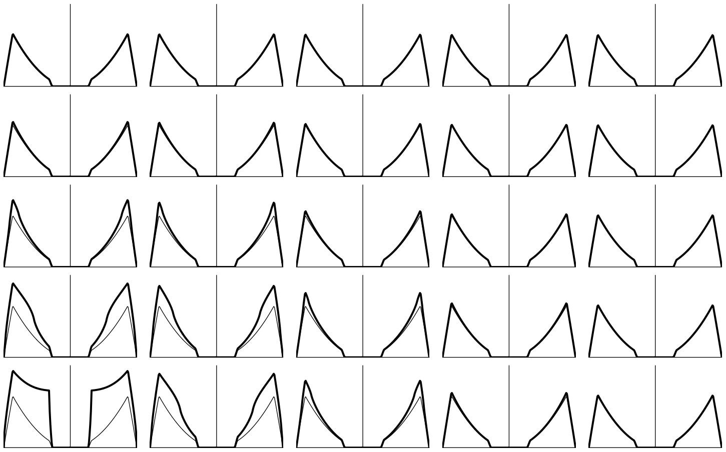

FIGURE 3.10— The same as in Fig. 3.9, but for $\eta_0 = r_{\rm blr}/4$.

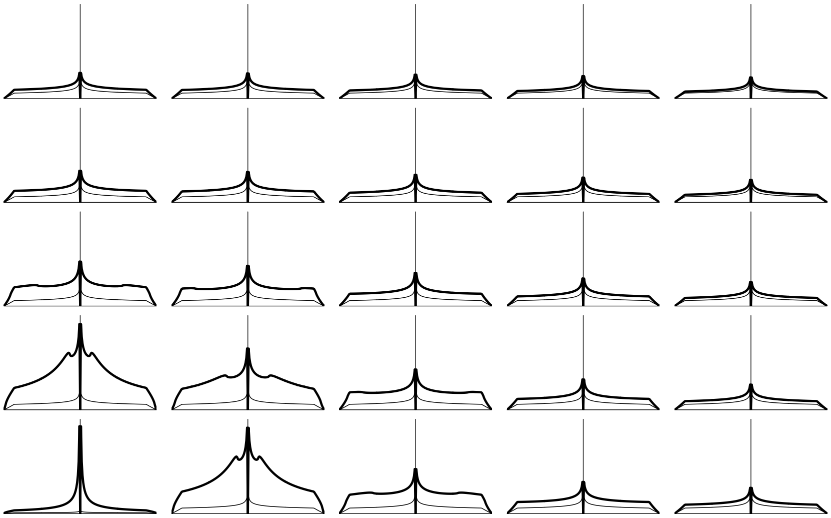

FIGURE 3.11— Biconical model with $i = 0°$, $p = 2$, $\beta = -1.5$, and $\eta_0 = r_{\rm blr}$. On the x-axis we represent $x = c\ (\lambda - \lambda_0)/(v_{\rm max}\lambda_0)$, which varies between -1 and 1. On the y-axis we represent the flux. The heavy solid line is the amplified line profile and the solid line is the unamplified line profile. The figure in the bottom left-hand corner has been multiplied by a factor of 7.2 for display purposes.

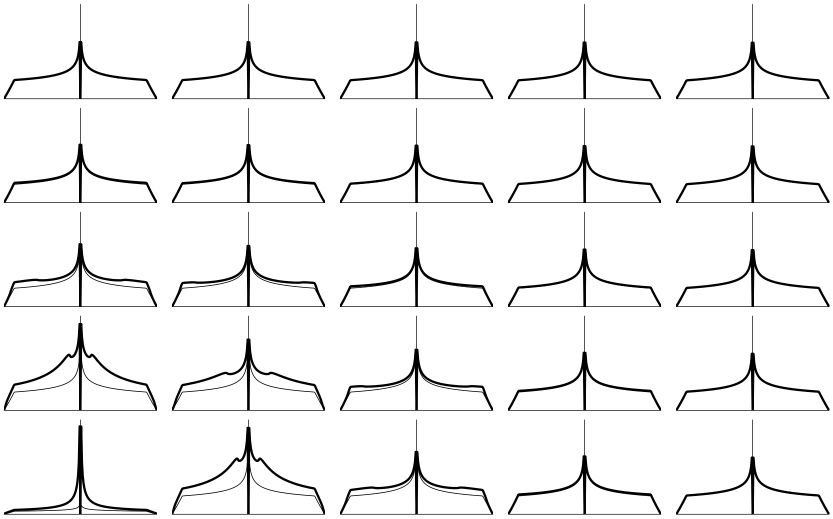

FIGURE 3.12— The same as in Fig. 3.11, but for $\eta_0 = r_{\rm blr}/4$. The figure in the bottom left-hand corner has been multiplied by a factor of 6.0 for display purposes.

$i = 90°$

The line profile (see Appendix B.2.2) is obtained by integrating

$$F_x = \int\limits_{{\rm Max}[r_{\rm lim},r_{\rm in}]}^{r_{\rm blr}} \left(\left[\int\limits_{\theta_{\rm lim}}^{\theta_{\rm c}} + \int\limits_{\pi-\theta_{\rm c}}^{{\rm Min}[\pi-\theta_{\rm lim},\pi]} \right] f(x,r,\theta)\ d\theta \right) dr, \tag{3.14}$$

where

$$f(x,r,\theta) = \begin{cases} \dfrac{\epsilon_0 r_{\rm in}^2 c}{\lambda_0 v_0} \left(\dfrac{r}{r_{\rm in}}\right)^{\beta+2-p} \dfrac{\sin\theta\ [\mu_+(x,r,\theta)+\mu_-(x,r,\theta)]_{f=0}}{\sqrt{\sin^2\theta - \left[\frac{x}{x_{\rm m}}\left(\frac{r}{r_{\rm in}}\right)^{-p}\right]^2}} & \\ & \text{for } \theta > \theta_{\rm lim}, \\ 0 & \text{in other cases,} \end{cases} \tag{3.15}$$

with $\theta_{\rm lim} = \arcsin[(|x|/x_{\rm m})(r/r_{\rm in})^{-p}]$, $x_{\rm m} = v_0/v_{\rm max} = (r_{\rm in}/r_{\rm blr})^p$. The amplification $[\mu_\pm(x,r,\theta)]_{f=0}$ is given by Eq. 3.5, inserting Eq. B.26 into Eq. B.28.

In Figures 3.13 and 3.14 we present the grids of profiles for $\tilde{r}_{\rm BLR} = 1$ and 4 corresponding to $\eta = 2$ and in Figures 3.15 and 3.16 the grids corresponding to $\eta = -0.25$. In this case, $i = 90°$, we obtain single-peaked profiles, convex for $\eta = 2$, and concave for $\eta = -0.25$. The effects of microlensing are very strong,

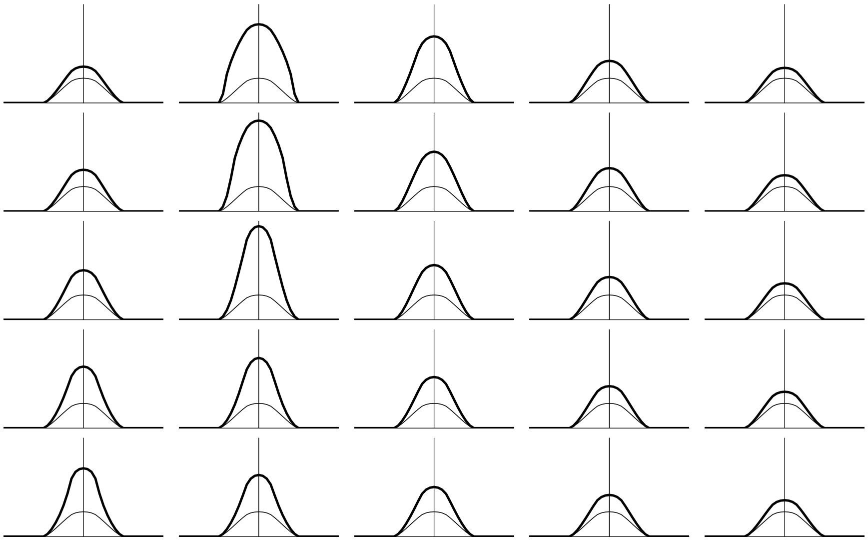

FIGURE 3.13— Biconical model with $i = 90°$, $p = 0.5$, $\beta = -1.5$, and $\eta_0 = r_{\rm blr}$. On the x-axis we represent $x = c\ (\lambda - \lambda_0)/(v_{\rm max}\lambda_0)$, which varies between -1 and 1. On the y-axis we represent the flux. The heavy solid line is the amplified line profile and the solid line is the unamplified line profile.

even for the case $\eta_0 = r_{\rm blr}/4$ (Figs. 3.14 and 3.16). Although the amplification strongly depends on the distance between the microlens and the source, in this case very off-centered line profiles suffering a larger amplification than other line profiles with smaller off-centered positions are found.

$i = 45°$

The line profile (see Appendix B.2) is obtained by integrating

$$F_x = \int_0^{\pi} \left(\left[\int_0^{\theta_{\rm c}} + \int_{\pi-\theta_{\rm c}}^{\pi} \right] [g(x,\varphi,\theta)]_{f=0}\ \sin\theta d\theta \right) d\varphi, \tag{3.16}$$

where

$$[g(x,\varphi,\theta]_{f=0} = \begin{cases} \frac{\epsilon_0 r_{\rm in}^3 c}{\lambda_0 v_0 p} \left(\frac{x}{x_{\rm m}}\right)^{\eta} \frac{[\mu(x,\varphi,\theta)]_{f=0}}{|\xi|^{\eta+1}} & \text{for } x_m|\xi| < |x| < |\xi|, \\ 0 & \text{in other cases,} \end{cases} \tag{3.17}$$

with $x_{\rm m} = v_0/v_{\rm max} = (r_{\rm in}/r_{\rm blr})^p$, and $[\mu_\pm(x,\varphi,\theta)]_{f=0}$ is given by Eq. 3.5, inserting Eq. B.17 into Eq. B.19.

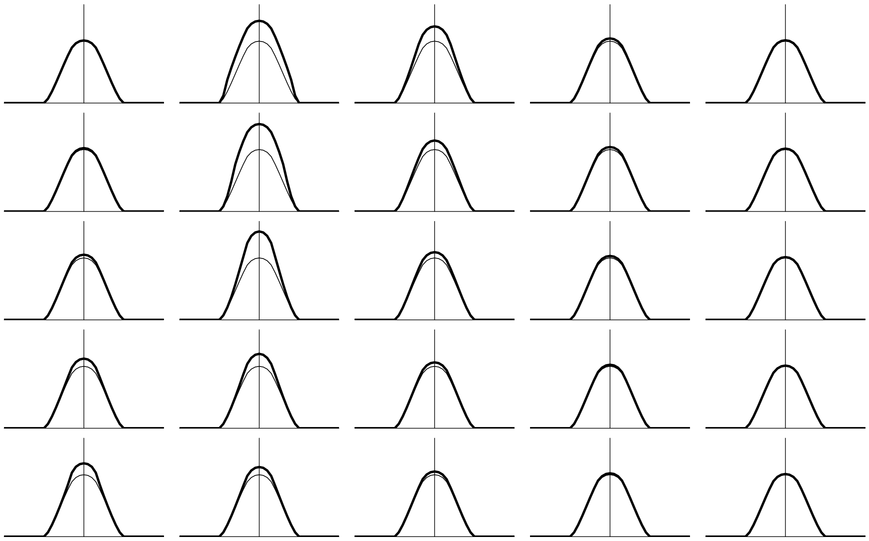

FIGURE 3.14— The same as in Fig. 3.13, but for $\eta_0 = r_{\rm blr}/4$.

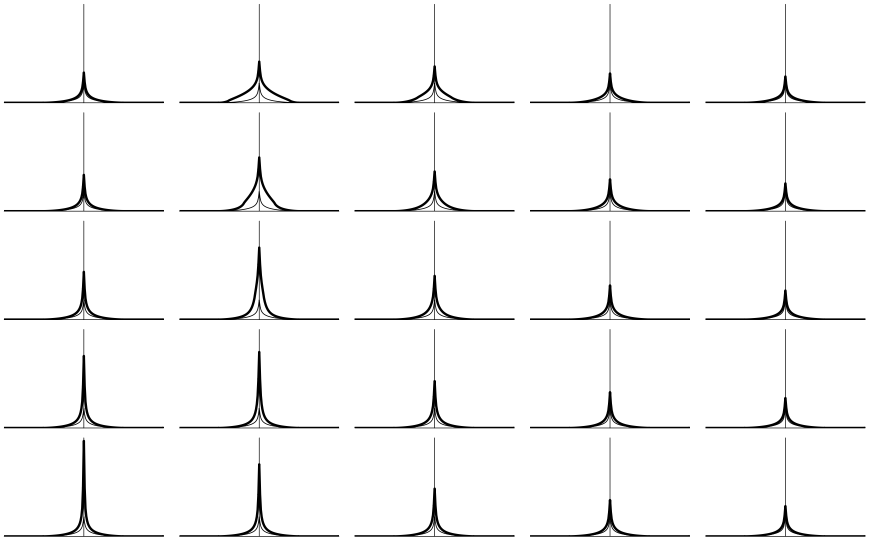

FIGURE 3.15— Biconical model with $i = 90^\circ$, $p = 2$, $\beta = -1.5$, and $\eta_0 = r_{\rm blr}$. On the x-axis we represent $x = c\ (\lambda - \lambda_0)/(v_{\rm max}\lambda_0)$, which varies between -1 and 1. On the y-axis we represent the flux. The heavy solid line is the amplified line profile and the solid line is the unamplified line profile.

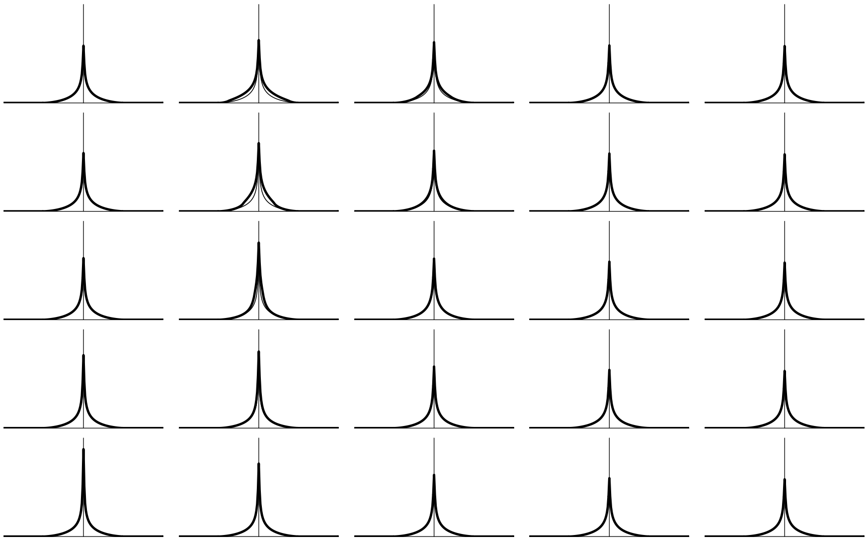

FIGURE 3.16— The same as in Fig. 3.15, but for $\eta_0 = r_{\rm blr}/4$.

In Figures 3.17 and 3.18 we present the grids of profiles for $\tilde{r}_{\rm BLR} = 1$ and 4 corresponding to $\eta = 2$ and in Figures 3.19 and 3.20 the grids corresponding to $\eta = -0.25$. In this case, $i = 45°$, we can observe asymmetrical enhancements. The effects of microlensing are very strong, even for the case $\eta_0 = r_{\rm blr}/4$ (Figs. 3.18 and 3.20).

For the limiting geometries considered here ($i = 0°, 90°$) there are no asymmetries induced by the microlensing in the line profile. However, for an arbitrary inclination, an off-centered microlens induces relative enhancements of the blue and red parts. Due to the loss of symmetry of the projected velocity field with respect to that of the spherical case, the inversion of the profile equation to study the velocity field should be easier. For instance, in the case of small cone aperture, the crossing of a microlens along the biconical axis would serve to virtually map the radial dependence of the velocity field.

3.3.3 Cylindrical shell

Rotation in a plane disc has often been considered in relation to the kinematics of the BLR and is typically characterized by the presence of a central dip (Mathews 1982) in the line profile arising from the finite extension of the outer radius of the disc. This feature is not usually found in the observed line profiles, but there are several ways to avoid it in the models (see Robinson

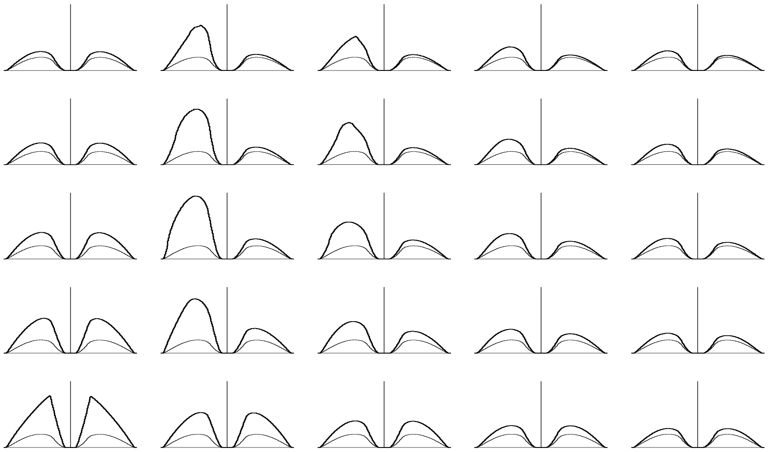

FIGURE 3.17— Biconical model with $i = 45°$, $p = 0.5$, $\beta = -1.5$, and $\eta_0 = r_{\rm blr}$. On the x-axis we represent $x = c\ (\lambda - \lambda_0)/(v_{\rm max}\lambda_0)$, which varies between -1 and 1. On the y-axis we represent the flux. The heavy solid line is the amplified line profile and the solid line is the unamplified line profile.

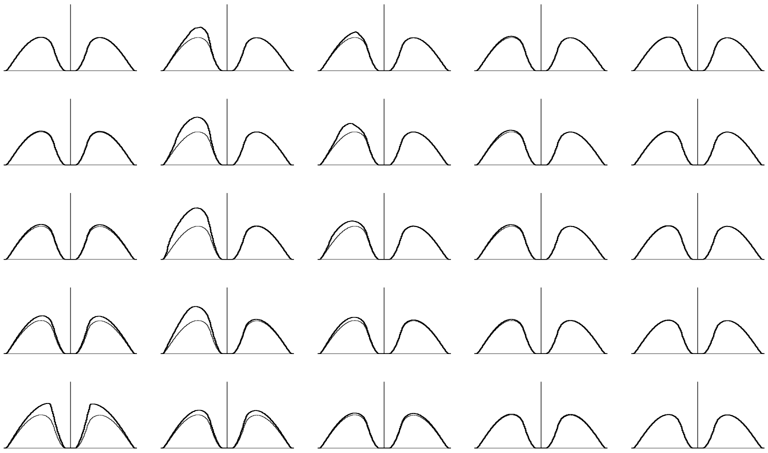

FIGURE 3.18— The same as in Fig. 3.17, but for $\eta_0 = r_{\rm blr}/4$.

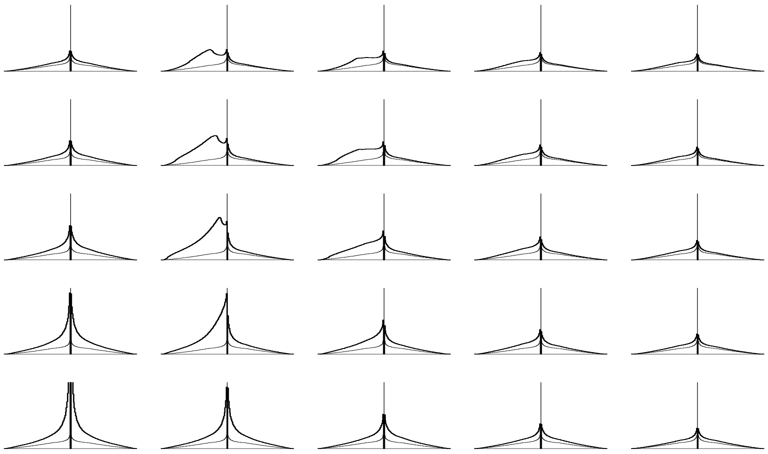

FIGURE 3.19— Biconical model with $i = 45°$, $p = 2$, $\beta = -1.5$, and $\eta_0 = r_{\rm blr}$. On the x-axis we represent $x = c\ (\lambda - \lambda_0)/(v_{\max}\lambda_0)$, which varies between -1 and 1. On the y-axis we represent the flux. The heavy solid line is the amplified line profile and the solid line is the unamplified line profile.

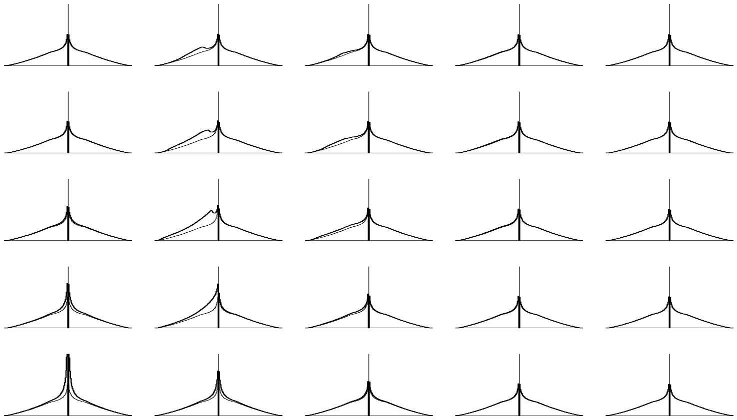

FIGURE 3.20— The same as in Fig. 3.19, but for $\eta_0 = r_{\rm blr}/4$.

1995). Nevertheless, the existence of rotation is strongly supported by recent observational work (Peterson & Wandel 1999).

We consider two different velocity laws for emitters in this model. A Keplerian velocity with the exponent of the velocity law $p = -0.5$, which produces double-peaked profiles, and a modified Keplerian velocity, with $p = -0.5$ too but producing this time single-peaked profiles. Thus, we want to study the effects of each model, covering both shapes of spectral lines.

Keplerian disc

The Keplerian disc is a particular case of the cylindrical disc with velocity field

$$v_{||} = v_0 \left(\frac{r}{r_{\rm in}}\right)^p \cos\varphi \sin i \quad (p = -0.5), \tag{3.18}$$

where r and φ are polar coordinates of an emitter in the disc.

The line profile is given by (see Appendix B.3):

$$F_x = \begin{cases} \frac{\epsilon_0 r_{\rm in} c}{\lambda_0 v_0 \sin i} \int_{r_{\rm in}}^{{\rm Min}[r_{\rm lim}, c]} \left(\frac{r}{r_{\rm in}}\right)^{\beta+1-p} \frac{[\mu_+(x,r)+\mu_-(x,r)]_{f=0}}{\sqrt{1-\left[\frac{x}{\sin i}\left(\frac{r}{r_{\rm in}}\right)^{-p}\right]^2}}\, dr & \\ & \text{for } r_{\rm lim} > r_{\rm in}, \\ 0 & \text{for } r_{\rm lim} < r_{\rm in}, \end{cases} \tag{3.19}$$

where $r_{\rm lim} = r_{\rm in}\ (|x|/\sin i)^{1/p}$, $x_{\rm m} = (r_{\rm in}/r_{\rm BLR})^{-p}$ and $[\mu_\pm(x,r)]_{f=0}$ is given by Eq. 3.5, inserting Eqs. B.33 and B.34 into Eq. B.36.

In Figures 3.21 and 3.22 we present the grid of profiles for $\tilde{r}_{\rm BLR} = 1$ and 4 with $i = 45°$, $\beta = -1.5$, and $\eta = (\beta + 2)/p - 1$. The most noticeable feature associated with the Keplerian case (and with the cylindrical case in general) is the presence of strong asymmetries in the line profiles induced by the microlensing.

Modified Keplerian disc

An easy way of generating a single-peaked profile in the cylindrical case is to modify the velocity field increasing the contribution of low velocities. For our purpose we adopt

$$v_{||} = v(r) \cos\varphi \sin i \quad (p = -0.5), \tag{3.20}$$

and

$$v(r) = v_0 \left(\frac{\frac{1}{r} - \frac{1}{r_{\rm blr}}}{\frac{1}{r_{\rm in}} - \frac{1}{r_{\rm blr}}}\right)^{-p} = v_0\ u(r), \tag{3.21}$$

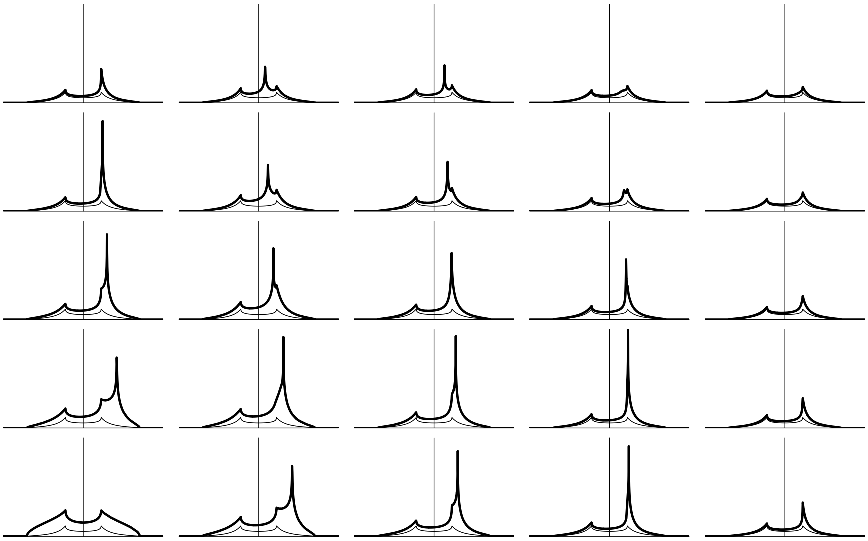

FIGURE 3.21— Model of Keplerian disc with $i = 45°$, $p = -0.5$, $\beta = -1.5$, and $\eta_0 = r_{\rm blr}$. On the x-axis we represent $x = c\ (\lambda - \lambda_0)/(v_{\rm max}\lambda_0)$, which varies between -1 and 1. On the y-axis we represent the flux. The heavy solid line is the amplified line profile and the solid line is the unamplified line profile.

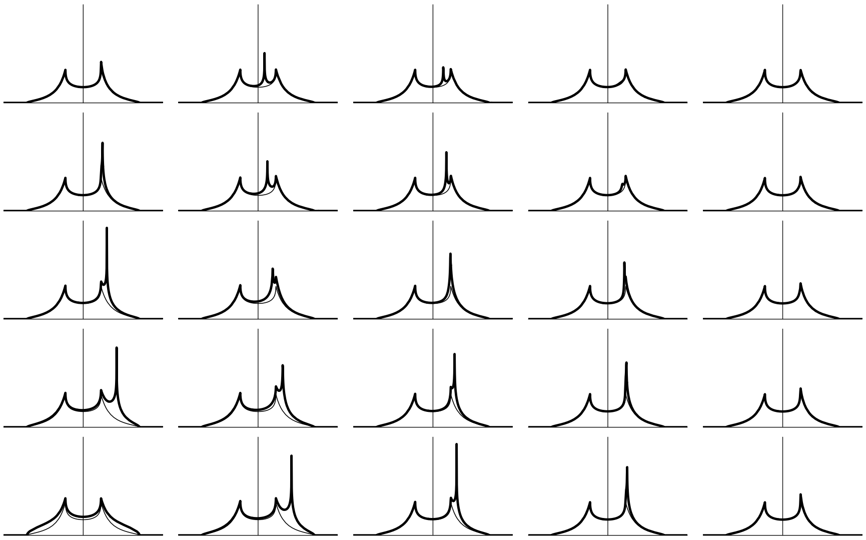

FIGURE 3.22— The same as in Fig. 3.21, but for $\eta_0 = r_{\rm blr}/4$.

where r and φ are polar coordinates of an emitter in the disc.

In this case, the line profile is given by (see Appendix B.3)

$$F_x = \begin{cases} \frac{\epsilon_0 r_{\rm in} c}{\lambda_0 v_0 \sin i} \int_{r_{\rm in}}^{{\rm Min}[r_{\rm lim}, r_{\rm blr}]} \left(\frac{r}{r_{\rm in}}\right)^{\beta+1} \frac{[\mu_+(x,r)+\mu_-(x,r)]_{f=0}}{u(r)\sqrt{1-\left(\frac{x}{u(r)\sin i}\right)^2}} dr \\ \qquad\qquad\qquad\qquad\qquad\qquad\qquad\qquad \text{for} \quad r_{\rm lim} > r_{\rm in}, \\ 0 \qquad\qquad\qquad\qquad\qquad\qquad\qquad\qquad \text{for} \quad r_{\rm lim} < r_{\rm in}, \end{cases} \tag{3.22}$$

where $r_{\rm lim} = \left[(|x|/\sin i)^{-1/p}\,(1/r_{\rm in} - 1/r_{\rm BLR}) + 1/r_{\rm blr}\right]^{-1}$, $x_{\rm m} = r_{\rm in}/r_{\rm blr}$, and $[\mu_\pm(x,r)]_{f=0}$ is given by Eq. 3.5, inserting Eqs. B.33 and B.34 into Eq. B.36.

In Figures 3.23 and 3.24 we present the grid of profiles for $\tilde{r}_{\rm BLR} = 1$ and 4 with $i = 45°$and $\beta = -1.5$. In addition to the asymmetries, the most interesting effect of microlensing on the line profiles corresponding to the Keplerian modified velocity field is the displacement of the line peak with respect to the centroid of the non-microlensed line profile, $\Delta x_{\rm p}$, (Fig. 3.25), which, independently of the mass considered ($\tilde{r}_{\rm BLR} = 1, 4$), can be of the order of as much as $\sim$ FWZI/4[3].

3.4 Discussion

If the models and assumptions of the previous sections constitute a good description of BLR microlensing, we could conclude that the effects of this phenomenon on the line profiles should be not only noticeable but also easily detectable in some lens systems.

The experimental situation, however, is more complex. In the first place, the BELs are blended with the narrow emission lines, which come from the much more extended narrow-line region (NLR), which would not be affected by microlensing. In fact, it is likely that diverse transition regions between the BLR and the NLR could also contribute to the core of the line profile. Second, the compactness of the lens systems makes observation very difficult. For instance, in the case (B 1600+434) in which we have obtained a realistic estimate for microlensing amplification there are two compact images, the lens galaxy (an edge-on spiral), and some additional extended emission, all within a separation of $\sim 2''$. This is a major setback when trying to obtain individual spectra, and only modern spectroscopic techniques (2D spectroscopy, Mediavilla et al. 1998 and references therein) or observation from space avoid the problems induced by source blending and differential atmospheric refraction. In any case, to detect microlensing we should obtain spectra (preferably of high-ionization lines) with

---

[3] FWZI: Full width at zero intensity.

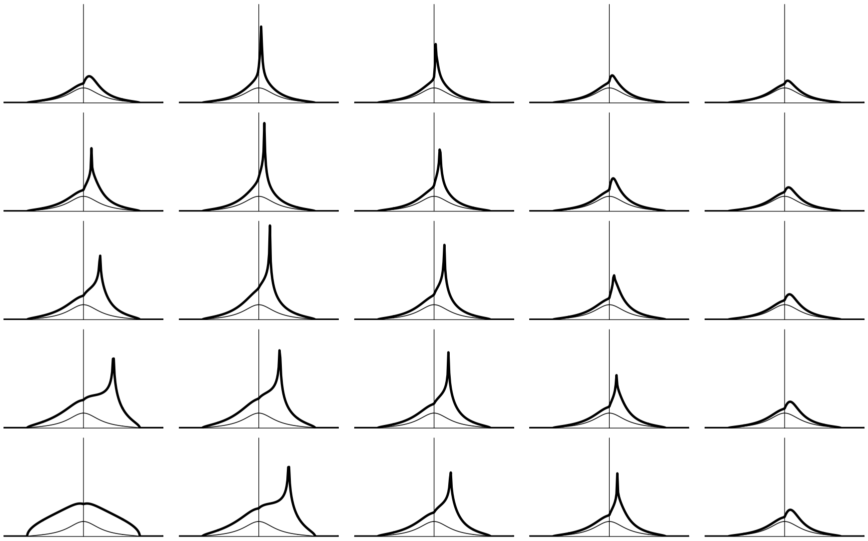

FIGURE 3.23— Model of modified Keplerian disc with $i = 45°$, $p = -0.5$, $\beta = -1.5$, and $\eta_0 = r_{\rm blr}$. On the x-axis we represent $x = c\ (\lambda - \lambda_0)/(v_{\rm max}\lambda_0)$, which varies between -1 and 1. On the y-axis we represent the flux. The heavy solid line is the amplified line profile and the solid line is the unamplified line profile.

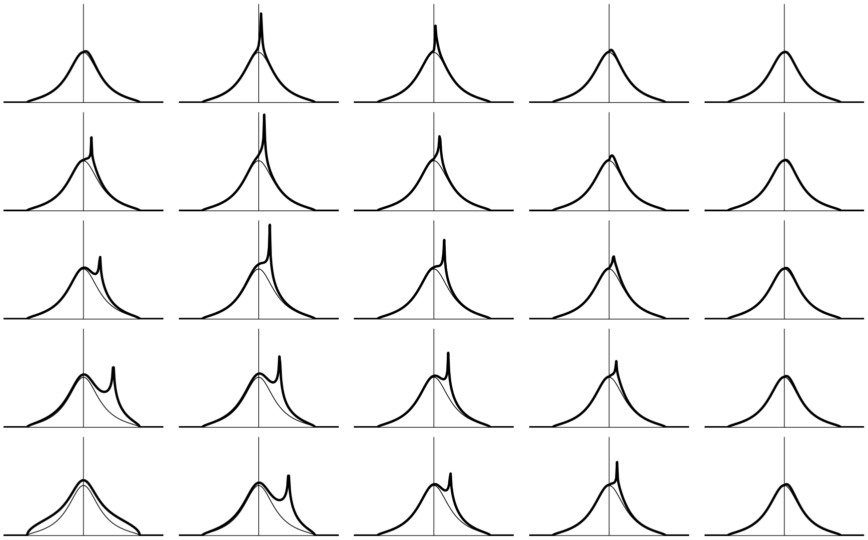

FIGURE 3.24— The same as in Fig. 3.23, but for $\eta_0 = r_{\rm blr}/4$.

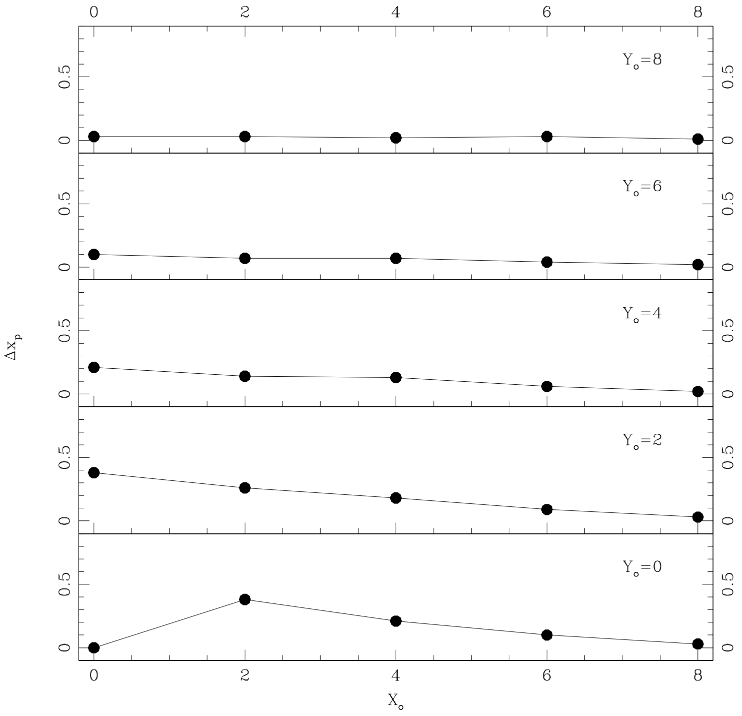

FIGURE 3.25— Displacements of the line peaks, $\Delta x_{\rm p}$, in the modified Keplerian disc model with $i = 45°$, $p = -0.5$, $\beta = -1.5$, and $\eta_0 = r_{\rm blr}/4$ in the different positions (X_0, Y_0).

a high S/N ratio in the wings of the line profile, where the contribution from the BLR would be dominant.

The emissivity is another important parameter that can affect the detection of microlensing on BELs. In Figure 3.26 we present the ratio of the amplified to unamplified line profiles corresponding to the modified Keplerian case, where we have changed the emissivity parameter, β. For a highly concentrated BLR ($\beta = -4$) the effect is stronger when the BLR is almost centered on the microlens and weak for larger displacements of the microlens with respect to the center of the BLR. But when the emissivity is constant (for a disc of uniform brightness, $\beta = 0$) the effects of microlensing remain noticeable for all displacements considered and are hence more likely to be observed.

In Figure 3.1 we have labeled the gravitational lens systems in which significant BEL microlensing could be detected (30% of the total). Even so, in other systems a modest effect could be detectable by looking at high-ionization

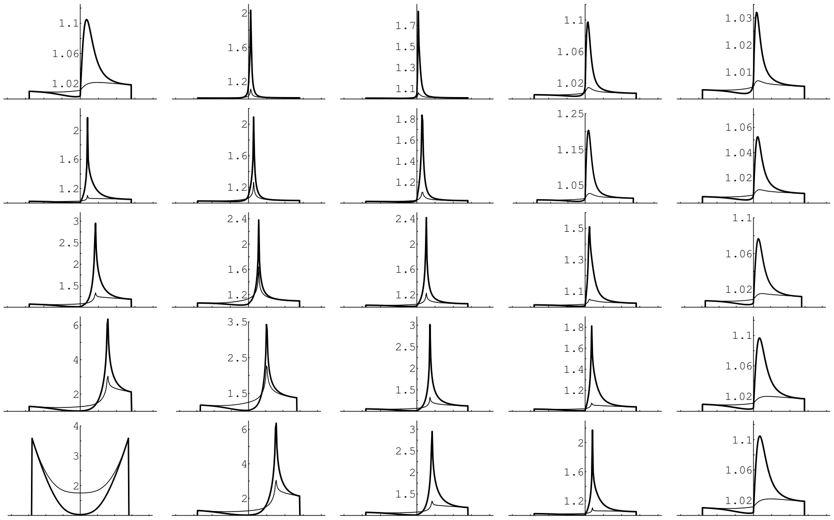

FIGURE 3.26— Model of modified Keplerian disc with $i = 45°$, $p = -0.5$, and $\eta_0 = r_{\rm blr}/4$. On the x-axis we represent $x = c\ (\lambda - \lambda_0)/(v_{\rm max}\lambda_0)$, which varies between -1 and 1. On the y-axis we represent the ratio between the amplified flux and the unamplified flux of the line profile. The heavy solid line is for $\beta = 0$ and the solid line is for $\beta = -4$.

lines. This is important because other different questions from the amplification, such as the crossing time of the microlens across the BLR or the frequency of the events, can lead us to study a gravitational lens system in particular. For instance, in a favorable case it would be possible not only to compare the line profile corresponding to microlensed and non-microlensed images but also to observe in the line profile of an image changes attributable to the microlens crossing. The most favorable case from this perspective is Q 2237+0305. This gravitational lens system was discovered by Huchra et al. (1985), and consists of a distant quasar, at $z_{\rm s} = 1.695$, quadruply imaged by a nearby barred spiral galaxy, at $z_{\rm s} = 0.039$. The proximity of the lens galaxy gives rise to the predicted very short time delays among the four images, of the order of a day. Thus, intrinsic variability detected in only one of the components is certainly produced by microlensing. Microlensing events in this lensed quasar are reported each year with crossing times of the order of a year or less. However, this is a bright QSO in which only very modest amplifications of 30% or less can be expected in the high-ionization lines. This estimation of the amplification is, in any case, subject to changes in the BLR-size vs QSO-luminosity relationship, and also to the expected intrinsic dispersion from object to object.

In spite of the last comment, the amplifications associated with the high-ionization lines could be high in many cases, and only a strong departure from the assumptions made in this study (e.g., a severe underestimate of the extinction, very different behaviour of the BLR-size/QSO-magnitude relationship, or an unexpectedly low-mass population of microlenses) could avoid the detection of microlensing on the BELs by comparing the high-ionization line profiles of a microlensed and a non-microlensed image in the most favorable cases. According to this, the study of the incidence of microlensing on BELs could become a tool for studying the BLR size and stratification, especially when lines of different ionization are observed.

3.5 Conclusions

In the light of recent discoveries concerning the BLR size and its scaling with AGN luminosity, currently accepted values for microlens masses, and a variety of kinematic models for the BLR, we have revisited in this chapter the influence of microlensing on the BEL. We have computed grids of line profiles corresponding to different displacements of the microlens with respect to the BLR center. Some results are worth summarizing:

1.- The global amplification of the BEL induced by microlensing events could be relevant. We identify a group of ten gravitational lens systems (about 30% of the total sample) for which the microlensing effect could be observable, especially in high-ionization lines. In other gravitational lenses the microlensing amplifications would be much more modest.

2.- Even for relatively small microlenses corresponding to high values of the BLR radius/Einstein radius quotient, ($r_{\rm blr}/\eta_0 \sim 4$), the effects produced by the differential amplification of the line profile (relative enhancement of different parts of the line profile, line asymmetries, displacement of the peak of the line, etc.) would be easily detectable except for highly symmetric velocity fields. The displacement of the peak of the line profile caused by microlensing is especially interesting, since it could otherwise induce inexplicable redshift differences between the different images in a gravitational lens system.

3.- The study of the changes between the BEL profiles corresponding to microlensed and non-microlensed images, or among the BEL profiles of lines with different ionization in a microlensed image could be useful for probing current ideas about BLR size and stratification.

4

Microlensing by a straight fold caustic crossing

Ningún pesimista ha descubierto nunca
los secretos de las estrellas,
ni navegado a tierras inexploradas,
ni encontrado la paz de su espíritu.
Anónimo

4.1 Introduction

In most cases we can not simply think that microlensing is caused by an isolated compact object but we must consider a distribution of microdeflectors, placed in an extended object (typically, the lens galaxy). In this case, an idealized situation of a straight fold caustic with infinite length passing over the disc is sometimes used (Grieger, Kayser & Refsdal 1988; Witt, Kayser & Refsdal 1993; Schneider, Ehlers & Falco 1992; Yonehara et al. 1999; Popović et al. 2003), getting large amplifications which produce a typical asymmetric peak in the light curve. This is a crude but interesting approximation if the size of the source (i.e. disc) is small enough to consider that the microlensing event is produced by the crossing of one single caustic fold.

This chapter is a transitional work whose main aim is to improve the results obtained in the previous chapter, studying the influence of microlensing on BEL at low optical depth. The straight fold caustic crossing approximation is described in §4.3, where simple models of BLR are used to study the effects of microlensing under this approximation on the broad line profiles. In §4.4 microlensing by a straight fold caustic crossing on the Fe K_α line profile and X-ray continuum is discussed.

4.2 Microlensing and the Fe K_α line in AGN

The X-rays of AGN are generated in the innermost region of an accretion disc around a central supermassive black hole (§1.1.3). The emission line from iron K_α, Fe K_α, has been observed in the vast majority of AGN (see e.g. Nandra et al. 1997; Fabian et al. 2000), and it is probably produced in the very compact region near the black hole (Iwashawa et al. 1999; Nandra et al. 1999; Fabian et al. 2000). Observations of two lens systems seem to support the idea that the Fe K_α line could be strongly affected by microlensing (Oshima et al. 2001; Chartas et al. 2002).

In Figure 4.1 it is possible to see a comparison between the projected magnification pattern in the source plane of Q2237+0305A image and an accretion disc with a typical size of $1000\mathrm{R_s}$ equivalent to $0.09\eta_0$. Since the dimension of the X-ray emission region is of only several tens of $\mathrm{R_s}$, the approximation of the straight fold caustic can be assumed for the study of microlensing of the AGN Fe K_α X-ray emission line.

The magnification pattern of Q2237+0305A image shown in Fig. 4.1 was computed using the ray-shooting method described in §2.8. The parameters considered are (κ,γ)=(0.36, 0.40) (Schmidt, Webster & Lewis 1998). This map covers an area of $16\eta_0 \times 16\eta_0$ at the source plane, it was computed covering an area of $80\xi_0 \times 80\xi_0$ in the lens plane, and was obtained at a resolution of 1000 × 1000 pixels. 256 rays were shot per unlensed pixel, which means $6.4 \cdot 10^9$ rays traced between the observer and the source. The number of stars considered was 733, assuming that the entire optical depth is in compact objects, $\kappa_\mathrm{c} = 0$, and $M_\mathrm{microlenses} = 1M_\odot$. The theoretical mean amplification is 4.0064, and the mean amplification of the map is 4.0204.

4.3 Straight fold caustic crossing

The amplification factor of a straight fold caustic crossing is given by (Chang & Refsdal 1984; Schneider, Ehlers & Falco 1992):

$$\mu(\zeta) = \begin{cases} A_0 + \frac{\epsilon}{\sqrt{\zeta}} & \text{If } \zeta > 0, \\ A_0 & \text{If } \zeta < 0, \end{cases} \tag{4.1}$$

where ζ is the separation from the caustic in units of η_0, A_0 is the amplification outside the caustic, and ϵ represents a constant amplification factor of order

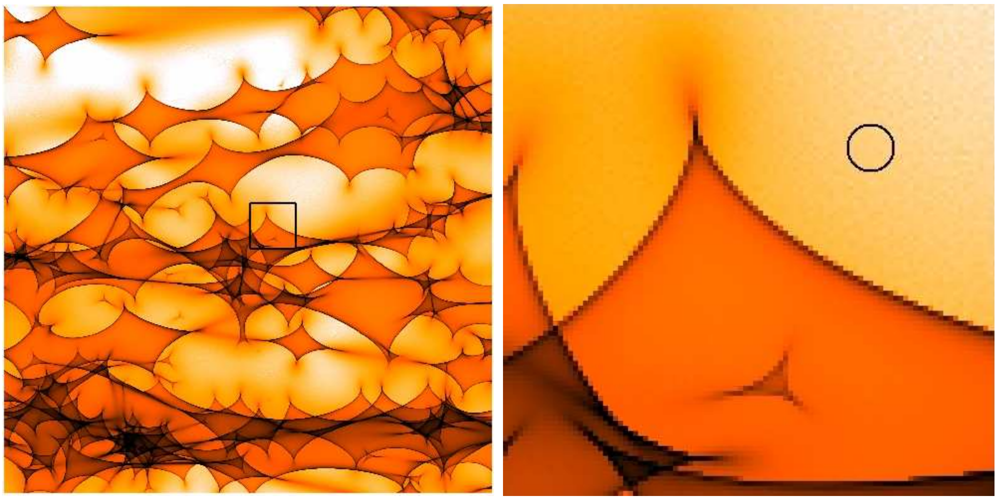

FIGURE 4.1— On the left-hand panel, a microlensing map of Q2237+0305A image is shown, with $16\eta_0$ on the side (Abajas 2005). On the right-hand panel a portion of the microlensing pattern is shown, marked with a square in the left-hand figure, and compared to a face-on accretion disc. The assumed outer radius of the disc is $0.09\eta_0$ (Popović et al. 2006).

of unity, which depends on the crossing point on the caustic (Witt, Kayser & Refsdal 1993). We will assume $A_0 = 1$ and $\epsilon = 1$, although higher values will cause higher amplification.

To illustrate the effects of microlensing by a straight fold caustic crossing we only have to insert Ec. 4.1 in

$$F_\lambda = \int_V \epsilon(r)\ \delta\left[\lambda - \lambda_0\left(1 + \frac{v_{||}}{c}\right)\right]\ \mu(\zeta)\ dV, \tag{4.2}$$

where the emissivity is $\epsilon(r) = \epsilon_0\,(r/r_{\rm in})^\beta$. Then, the correct expression for the projected line-of-sight velocity, $v_{||}$, which depends on the model: spherical, biconical or cylindrical, is (Abajas et al. 2005):

$$v_{||} = \begin{cases} v(r)\cos\theta & p > 0 \quad \text{spherical shell,} \\ v(r)(\sin\theta\sin\varphi\sin i + \cos\theta\cos i) & p > 0 \quad \text{biconical shell,} \\ v(r)\cos\varphi\sin i & p = -0.5 \quad \text{Keplerian disc,} \end{cases} \tag{4.3}$$

with the velocity law being $v(r) = v_0\,(r/r_{\rm in})^p$. In the modified Keplerian model the velocity is given by Ec. 3.21.

Using a development analogous to the one of Appendix B for each model we present the cases corresponding to a spherical shell, a Keplerian disc, and a modified Keplerian disc in Figures 4.2 to 4.5 and a bicone model in Figures 4.6 to 4.9. We have considered different orientations of the caustic (parallel, perpendicular and oblique) with regard to the X-axis.

There are no differences over the emission line profiles when the oblique caustic is leaned towards one or other side of the X-axis (Figs. 4.2, 4.3, 4.6 and 4.7), except for the biconical model with $i = 45°$ (Figs. 4.6 and 4.7) where there are asymmetrical enhancements of the line profile. Both Keplerian models and the biconical model with an intermediate inclination show asymmetric line profiles.

Figures 4.4 and 4.8 correspond to a parallel caustic crossing with respect to the X-axis. There are only asymmetrical enhancements of the line profile for $i = 45°$ of the biconical model. However, in Figure 4.9, that represents a caustic perpendicular to the X-axis, all the biconical models are symmetrical, including the $i = 45°$ cases, whereas the Keplerian and the modified Keplerian models with caustic perpendicular to the X-axis (Fig. 4.5) present asymmetrical enhancements of the line profile.

As can be seen in these figures, the effects of microlensing are also very significant under this approximation. In particular, the asymmetrical and alternating enhancements of the peaks of the biconical model (i= 45°) are very noticeable. We will discuss this result in more detail in §5.

However, the straight fold caustic approximation is only valid when the source is very small as compared with the caustic. This hypothesis is not, in general, realistic for the BLRs and the study of complex magnification patterns induced by the granulation of the mass distribution in the lens galaxies is needed.

4.4 Discussion

According to the ideas in §4.2, Popović et al. (2003) investigated the influence of microlensing on the AGN Fe K_α line shape originated in a compact accretion disc around a rotating (Kerr metric) and non-rotating (Schwarzschild metric) black hole, taking into account microlensing by an isolated compact object and by a straight fold caustic. They concluded that microlensing can give rise to significant changes in the iron line profiles, with the effects being two or three orders of magnitude greater than the ones inferred for the UV and optical lines (Popović, Mediavilla & Muñoz 2001). Strong asymmetries in the observed line profiles could be induced by straight fold caustic microlensing, being stronger in the blue part of the lines.

In a recent work (Popović et al. 2006) we have developed a model of microlensing by a straight fold caustic of a standard accretion disc to discuss the observed microlensing of the Fe K_α. This model has been used to study the relative enhancement between the X-ray continuum and the Fe K_α line emission, and also the chromaticity (see §2.1), i.e. the wavelength dependent geometry of the different emission regions (Wambsganss & Paczyński 1991; Lewis et al. 1998; Wisotzki et al. 2003). Several interesting results are that both the Fe K_α and the continuum may experience significant amplification, and the dependence with wavelength of the amplification can induce chromatic effects of about 30% during a microlensing event. When the emission is separated in two regions (an inner disc corresponding to the Fe K_α line and an outer annulus corresponding to the continuum, or vice-versa), this study can reproduce the observed enhancement of the iron line in the absence of corresponding continuum amplification found in three lensed QSOs -MG J0414+0534 (Chartas et al. 2002), QSO 2237+0305 (Dai et al. 2003), H1413+117 (Chartas et al. 2004)-, but only during limited time intervals. Then, continuum amplification is expected if a complete microlensing event is monitored.

4.5 Conclusions

After the isolated lens approximation we consider microlensing by a straight fold caustic. The main effects of microlensing amplification by an isolated star are also found in the case of microlensing by a straight fold caustic. We point out that, while the spherical and biconical ($i = 0°$ and $90°$) models are always symmetric, the Keplerian, modified Keplerian and biconical ($i = 45°$) models show strong asymmetrical red/blue enhancements.

As was commented in §4.1, the straight fold caustic crossing approximation is valid only when the size of the emission region is small as compared with the Einstein ring. For the continuum, this is true for a range of wavelengths from UV to X-Ray. For the lines, this is very important for the Fe K_α line, because it is generated in a tiny region. The study of this line is very relevant because it is likely to be generated close to the black hole horizon, and it could bring essential information about the plasma conditions and the space geometry around the black hole.

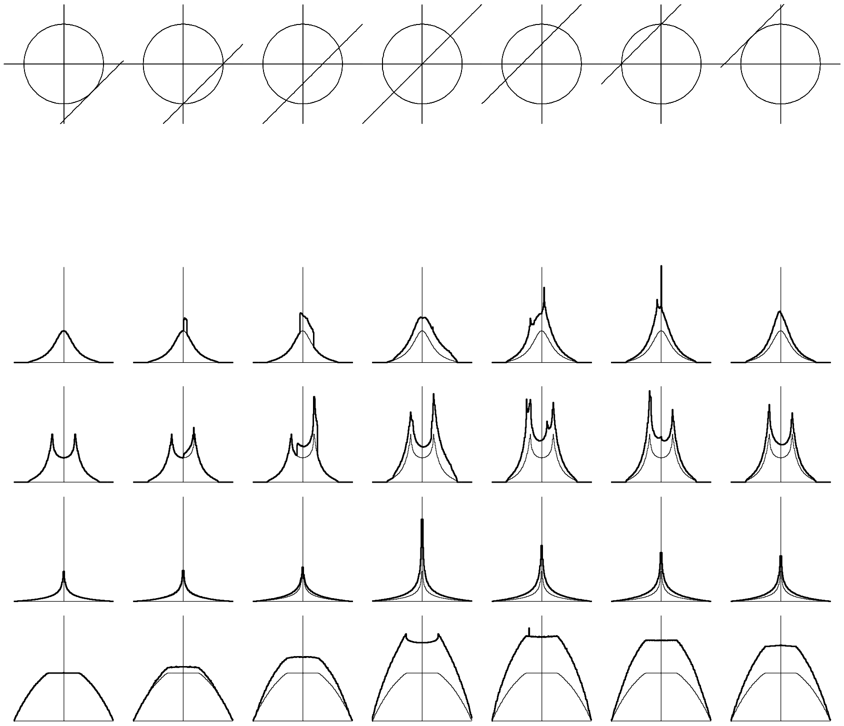

FIGURE 4.2— The models run vertically in this figure, there being from the bottom to the top two spherical models with $p = 0.5, 2$, a Keplerian model and a modified Keplerian model, both with $p = -0.5$. The different distances to the straight fold caustic run horizontally. On the x-axis we represent the velocity. On the y-axis we represent the flux of the line profile. The heavy solid line is the amplified line profile, and the lighter solid line is the unamplified line profile.

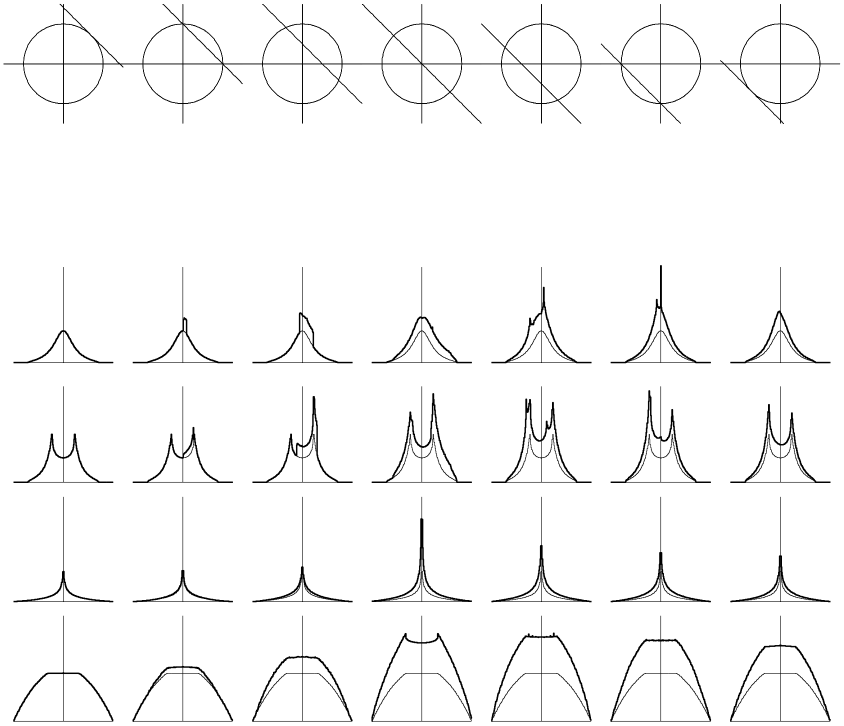

FIGURE 4.3— The same as in Fig. 4.2, but for another oblique straight fold caustic.

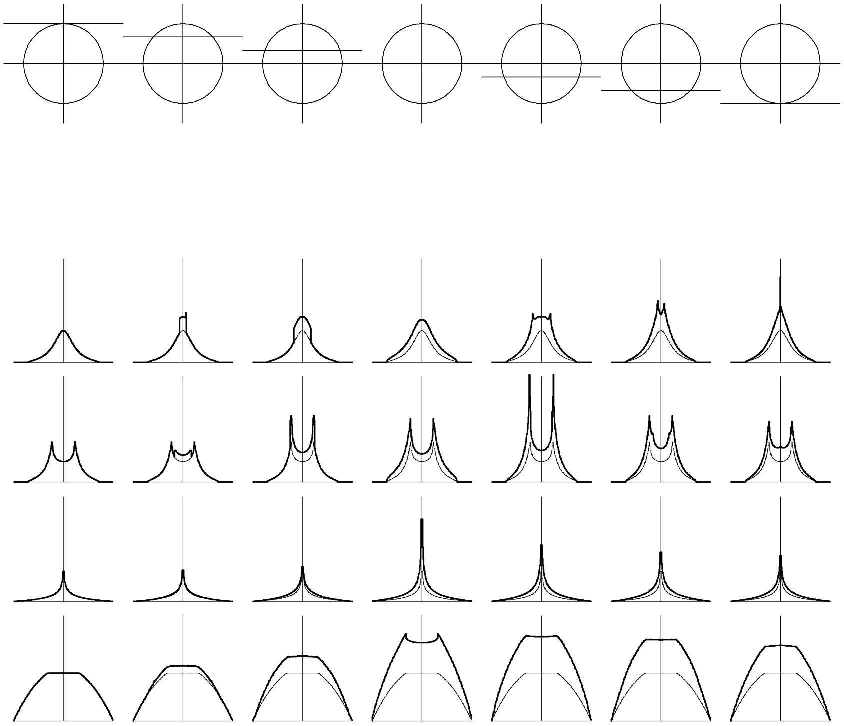

FIGURE 4.4— The same as in Fig. 4.2, but for a straight fold caustic parallel to the X-axis.

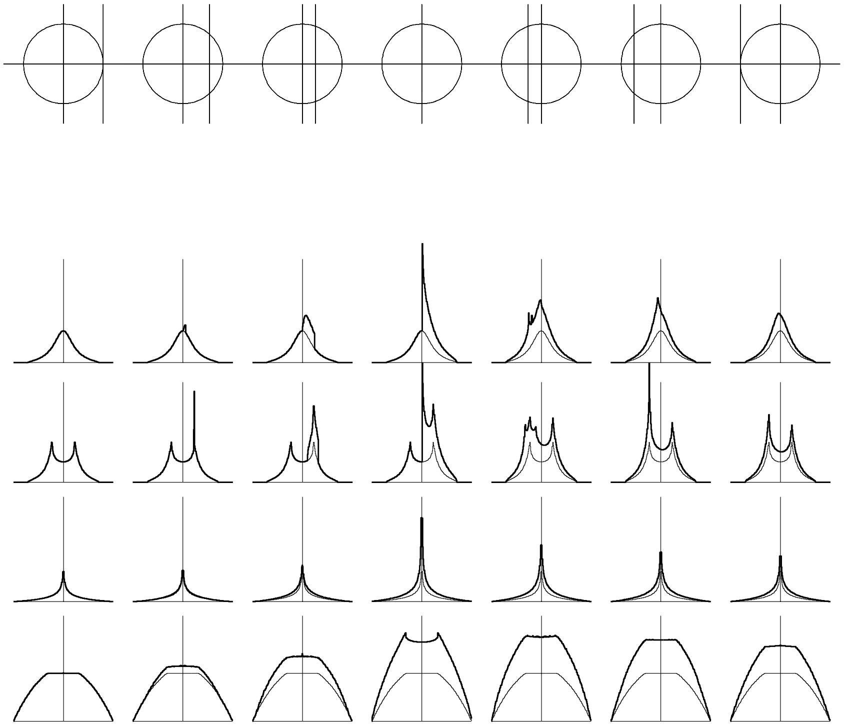

FIGURE 4.5— The same as in Fig. 4.2, but for a straight fold caustic perpendicular to the X-axis.

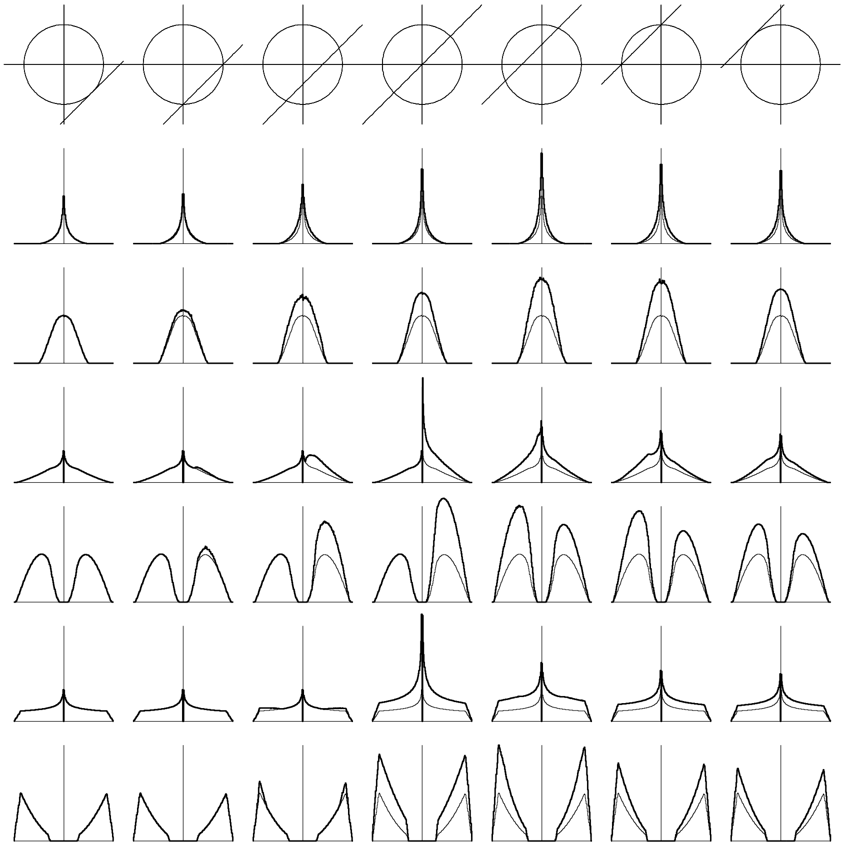

FIGURE 4.6— The models run vertically in this figure, there being from the bottom to the top six biconical models with these pairs of (p, i): (0.5, 0°), (2, 0°), (0.5, 45°), (2, 45°), (0.5, 90°), (2, 90°). The different distances to the straight fold caustic run horizontally. On the x-axis we represent the velocity. On the y-axis we represent the flux of the line profile. The heavy solid line is the amplified line profile, and the lighter solid line is the unamplified line profile.

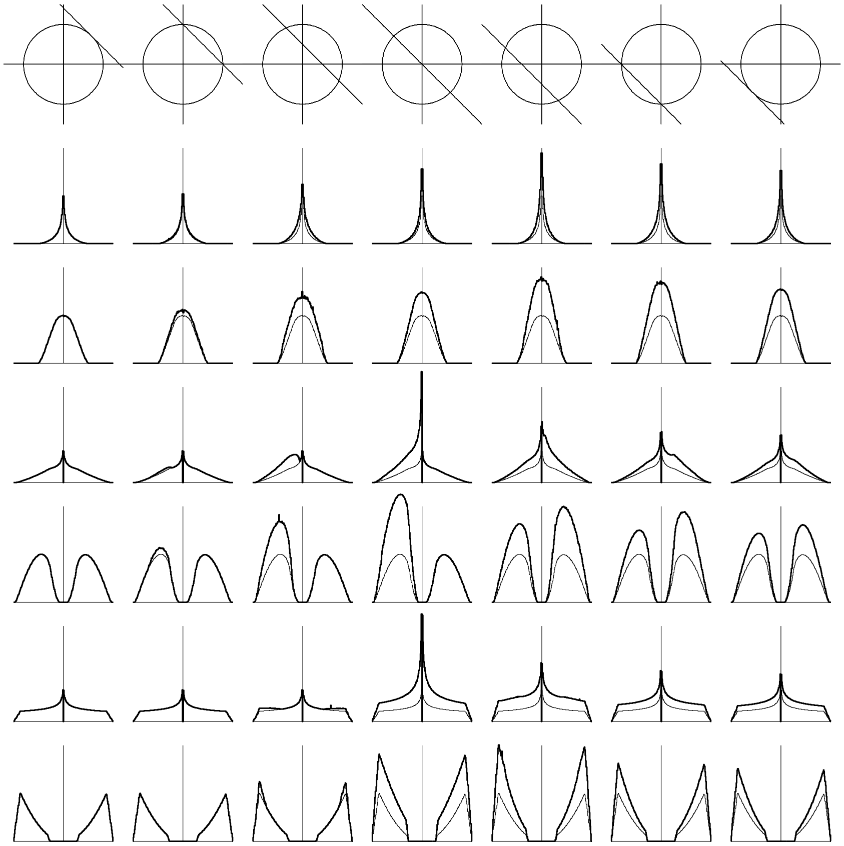

FIGURE 4.7— The same as in Fig. 4.6, but for another oblique straight fold caustic.

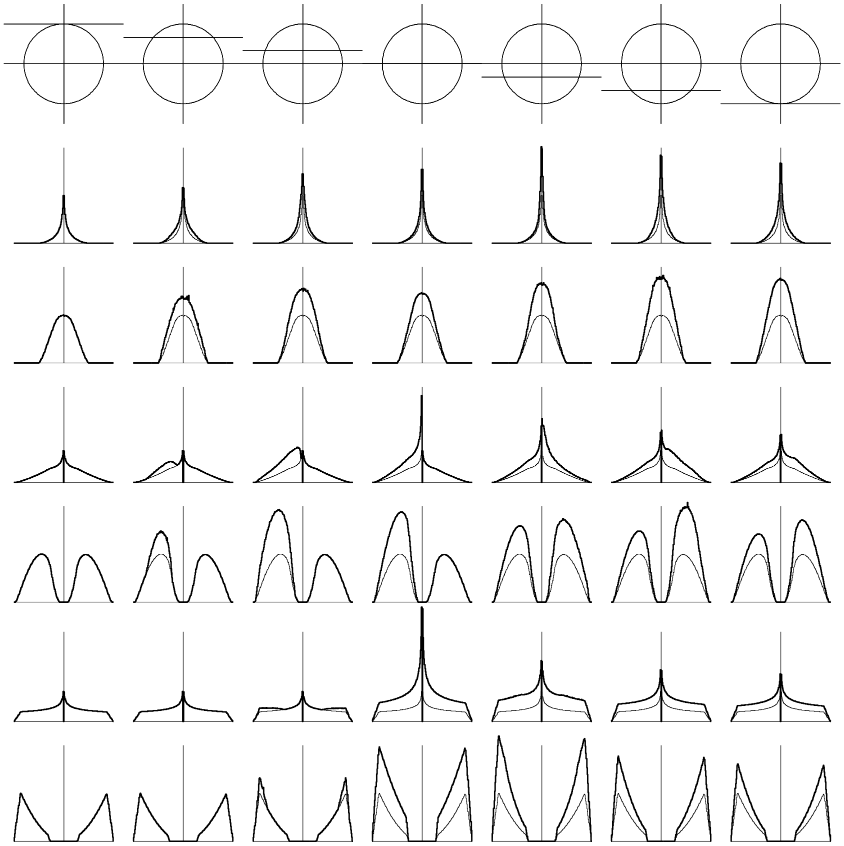

FIGURE 4.8— The same as in Fig. 4.6, but for a straight fold caustic parallel to the X-axis.

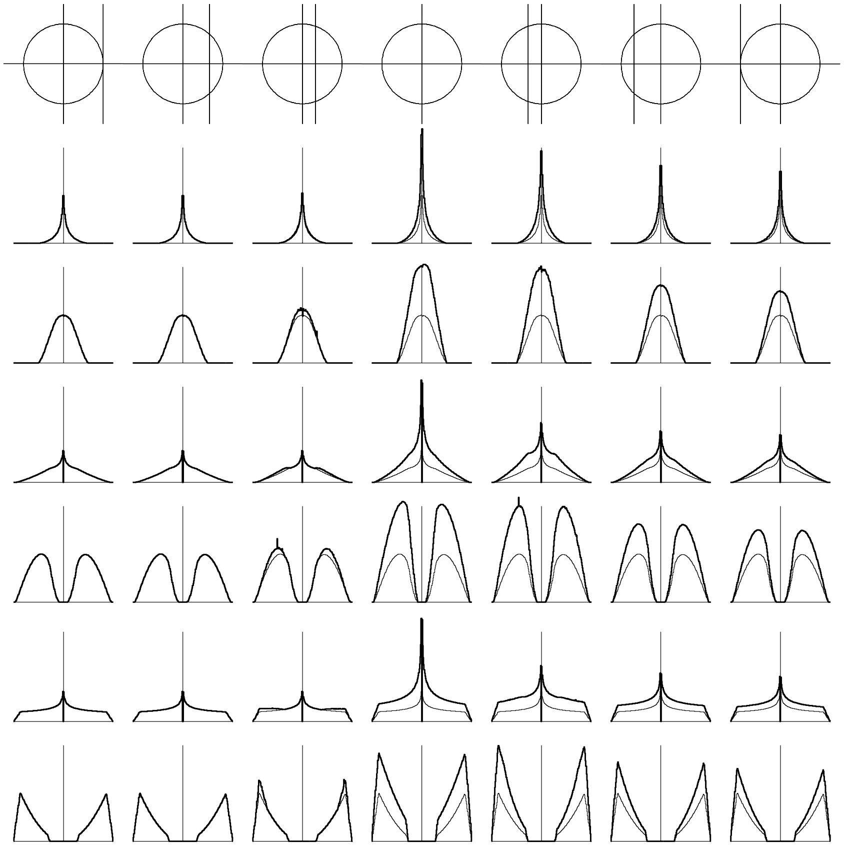

FIGURE 4.9— The same as in Fig. 4.6, but for a straight fold caustic perpendicular to the X-axis.

5

Microlensing by a caustic network

Las mentes son como los paracaídas,
sólo funcionan cuando están abiertos.
Anónimo

5.1 Introduction

The variability of the light-curve of a lensed object induced by the discretization of the mass distribution of the lens galaxy in stars or other compact objects (gravitational microlensing, Chang & Refsdal 1979; Young 1981; Paczyński 1986; Kayser, Refsdal & Stabell 1986; Schneider & Weiss 1987; Irwin et al. 1989; Witt 1990; Wambsganss 1990; Gil-Merino & Lewis 2005) offers a promising way of studying the unresolved source of the continuum of QSOs. Using microlensing the size of the quasar continuum source may be constrained by monitoring and studying quasar variations (Yonehara 1999), high-magnification event shapes (Wyithe & Webster 1999), fold caustic crossing events (Fluke & Webster 1999) and the microlens-induced centroid shift of a macrolensed image (Lewis & Ibata 1998). Additional AGN components such as the broad absorption line region may also be studied by microlensing (e.g. Belle & Lewis 2000; Chelouche 2005)

Studies in §3 (Abajas et al. 2002) and §4 (Abajas et al. 2005) have shown that the BLR can be significantly amplified by microlensing of stellar-sized objects. Different plausible geometries for the BLR were considered (Robinson 1995). An expected result, confirmed in these works and in Lewis & Ibata (2004), is that the less symmetrical models -cylindrical and biconical- induce the most interesting distortions in the line profiles. However, the microlensing at high optical depth of the biconical model has been studied in only two limiting cases, for inclinations 0° and 90° (Lewis & Ibata 2004), in which the crucial effects of differential amplification between the receding and approaching parts of the velocity field are absent. Another important and unnoticed characteristic of the biconical model is that the emissivity-weighted radius of a conical section of a sphere is the same independently of the cone aperture. This implies that the length of the cones (related to the emissivity-weighted radius) is not a direct estimate of the size of the projected surface of a biconical BLR and, hence, that the microlensing (de-)amplification can be strongly dependent on the orientation and aperture of the cones.

In this chapter we explore microlensing effects on a biconical model (Abajas et al. 2006) consistent with much experimental evidence (Marziani, Calvani & Sulentic 1992; Wilson & Tsvetanov 1994) and theoretical work (Goldman & Bahcall 1982) supporting the idea that the flow of emitting gas in AGN is anisotropic, preferentially confined to a pair of oppositely directed cones (Zheng, Binette & Sulentic 1990; Robinson 1995). We consider the microlensing effects at high optical depth on the profiles of the broad emission lines in §5.2. In §5.3 the effects on the continuum are compared with those on the BLR. We then analyze the possible use of this model in explaining the characteristic variability detected on the BEL of the quadruple quasar lensed system J1004+4112 (§5.4).

5.2 Microlensing effects at high optical depth on the profile of broad emission lines

Throughout this chapter all microlenses have a common mass, $1M_{\odot}$, and all distances are normalized to the Einstein radius, η_0, associated with this microlens mass (Eq. 2.6). A standard cosmology is assumed with $H_0 = 70$ kms^{-1}-Mpc^{-1}, $\Omega_{\rm M} = 0.3$ and $\Omega_{\Lambda} = 0.7$.

5.2.1 Magnification patterns

As an illustrative example for a general study of the microlensing of a biconical BLR we have selected the gravitational lens B 1600+434, because in §3.2 we have found it to be a well studied lens system and a good candidate for observing microlensing of the BLR. Given the low number of constraints for this double-imaged quasar we just fitted a singular isothermal sphere plus an external shear to estimate the microlensing parameters, the convergence or optical depth, κ, and the shear due to the external mass, γ. For A and B images the values for (κ, γ) are (0.30,0.16) and (0.80,0.72), respectively.

The ray-shooting method described in §2.8 was used to compute the magnification maps. The map of the B1600+434B image (Fig. 5.1) having the biggest optical depth, with an area of $16\eta_0 \times 16\eta_0$ at the source plane, was computed covering an area of $60\xi_0 \times 60\xi_0$ in the lens plane, and was obtained at a resolution of 1000×1000 pixels. 256 rays were shot per unlensed pixel, which means $3.6 \cdot 10^9$ rays traced between the observer and the source. The number of stars considered was 912, assuming that the entire optical depth is in compact objects, $\kappa_c = 0$. The theoretical mean amplification $< \mu_{th} >= |(1-\kappa)^2 - \gamma^2|^{-1}$ is 2.068, and the mean amplification of the map is 1.900.

5.2.2 Biconical broad emission line region

In this section we adopt the kinematic model for a biconical BLR (Robinson 1995) used in previous chapters to study the effects of microlensing over the line profile shapes in the context of a simple parameterization of some basic properties of the BLR, such as the emissivity, the velocity law, the cone aperture and the inclination.

In a biconical model we need three polar coordinates (r, θ, φ) measured with respect to the cone axis to express the projected line-of-sight velocity corresponding to an emitter,

$$v_{||} = v_0 \left(\frac{r}{r_{\rm in}}\right)^p \xi_{\perp,||} \quad (p > 0), \tag{5.1}$$

with

$$\begin{aligned} \xi_{\perp} &= \sin\theta \sin\varphi \sin i + \cos\theta \cos i, \\ \xi_{||} &= \sin\theta \cos\varphi \sin i + \cos\theta \cos i, \end{aligned} \tag{5.2}$$

where i is the inclination of the cone axis with respect to the line of sight, and $\xi_{\perp}$ and $\xi_{||}$ are the projections of the bicone when it turns around the x and y axes, respectively. Both projections fit when $i = 0°$. Figure 5.2 shows the perpendicular projection on the left-hand panel and the parallel projection on the right-hand panel.

Following the Appendix B, the line profile is obtained by integrating

$$F_x = \begin{cases} a\left(\frac{x}{x_{\rm m}}\right)^{\eta} \int\limits_0^{2\pi} \left(\left[\int\limits_0^{\theta_{\rm c}} + \int\limits_{\pi-\theta_{\rm c}}^{\pi} \right] \frac{[\mu(\vec{r})]^{\rm f=0}_{\perp,||} \; \sin\theta \, d\theta}{|\xi_{\perp,||}|^{\eta+1}} \right) d\varphi & \text{for } x_{\rm m}|\xi_{\perp,||}| < |x| < |\xi_{\perp,||}|, \\ 0 & \text{in other cases,} \end{cases} \tag{5.3}$$

where $x = c(\lambda - \lambda_0)/(v_{\rm max}\lambda_0)$, $a = (\epsilon_0 r_{\rm in}^3 c)/(\lambda_0 p v_0)$, $x_{\rm m} = v_0/v_{\rm max} = (r_{\rm in}/r_{\rm ex})^p$, $\theta_{\rm c}$ is the cone aperture half-angle, $\eta = (\beta + 3 - p)/p$ and

$$\begin{aligned} [\mu(\vec{r})]^{\rm f=0}_{\perp} &= \mu\left([r]^{\rm f=0}_{\perp} \sin\theta\cos\varphi, [r]^{\rm f=0}_{\perp}(\sin\theta\sin\varphi\cos i - \cos\theta\sin i)\right), \\ [\mu(\vec{r})]^{\rm f=0}_{||} &= \mu\left([r]^{\rm f=0}_{||}(\sin\theta\cos\varphi\cos i - \cos\theta\sin i), [r]^{\rm f=0}_{||} \sin\theta\sin\varphi\right). \end{aligned} \tag{5.4}$$

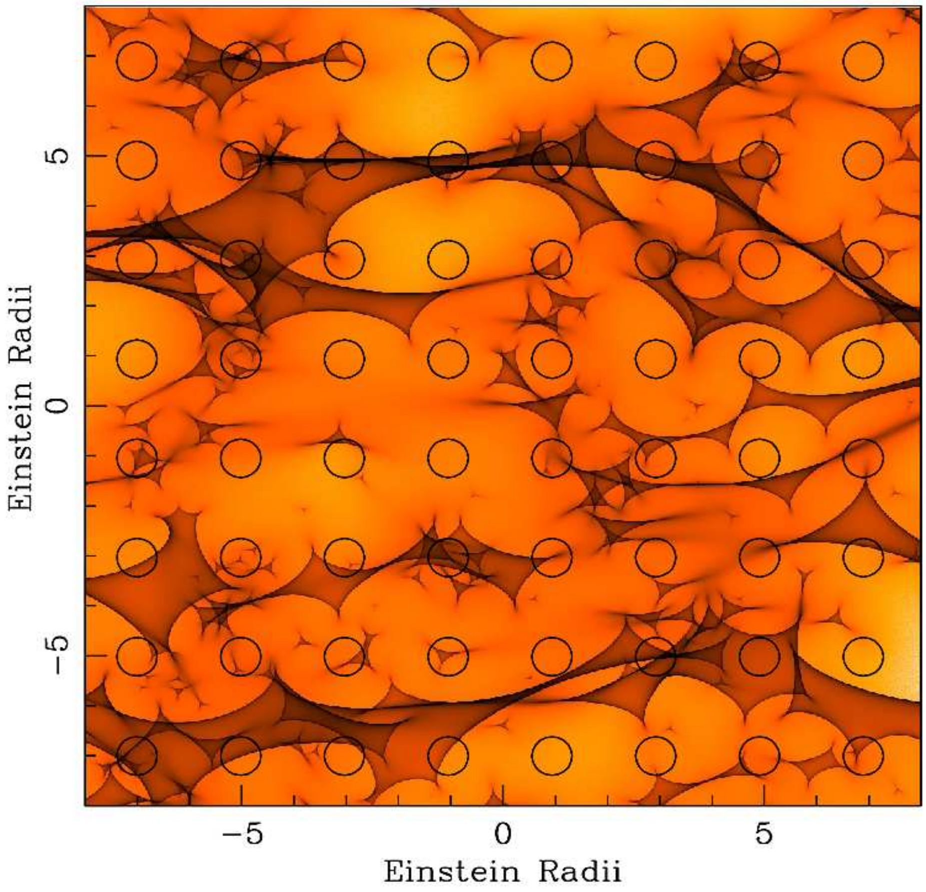

FIGURE 5.1— The magnification map, $\mu(\vec{r})$, for the B image of B1600+434, used here to calculate the changes in the shape of the line profile. Each circle represents the BLR in different positions over the magnification map with $r_{\rm ex} = 0.37\eta_0$.

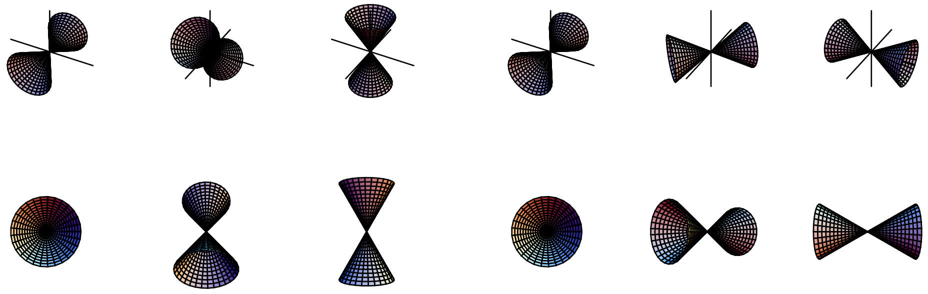

FIGURE 5.2— Projections of the bicone, perpendicular and parallel, from left to right with a cone half-aperture $\theta_c = 30°$.

5.2.3 Estimate of the broad line region radius for a biconical geometry

To estimate the BLR radius for B1600+434 we apply the relationship $r_{\rm BLR} \propto L^{0.67}$ from Kaspi et al. (2005) using NGC 5548 as a reference object. Following the same procedure as in §3.2.1, we have used the BLR size for high ionization lines of NGC 5548 as 2.5 light-days (He II line, Peterson & Wandel 1999) and from NED the visible magnitude and redshift of NGC 5548, $m_V = 13.3$ and $z = 0.017$. Apparent magnitudes are transformed into intrinsic luminosities by equation $L = 4\pi D_{\rm lum}^2 S(1+z)^{(\alpha-1)}$, with a spectral index $\alpha = 0.5$ (e.g., Richards et al. 2001). Then, the BLR radius for this double-imaged quasar is $r_{\rm BLR} = 4.95$ l-days for HILs, with the estimated intrinsic magnitude being $m_V = 22.63$ (§3.2.2).

The sizes measured by the reverberation method are in fact luminosity-weighted radii (Koratkar & Gaskell 1991) that correspond (Robinson & Pérez 1990) in the case of a biconical geometry to

$$\begin{aligned} r_{\rm BLR} = & \frac{\int_V r\epsilon(r)dV}{\int_V \epsilon(r)dV} = \frac{\int_{r_{\rm in}}^{r_{\rm ex}} r^{\beta+1}4\pi(1-\cos\theta_c)r^2dr}{\int_{r_{\rm in}}^{r_{\rm ex}} r^{\beta}4\pi(1-\cos\theta_c)r^2dr} = \\ & = \frac{\beta+3}{\beta+4}\,\frac{1-(r_{\rm in}/r_{\rm ex})^{\beta+4}}{1-(r_{\rm in}/r_{\rm ex})^{\beta+3}}\, r_{\rm ex}. \end{aligned} \tag{5.5}$$

We adopt an emissivity law with $\beta = -1.5$ and $r_{\rm in} = 0.1\ r_{\rm ex}$. Then $r_{\rm ex} = r_{\rm BLR}/0.618 = 0.37\eta_0$, with $1\eta_0(1M_\odot) = 21.58$ l-days in this gravitational lens.

5.2.4 Microlensed line profiles

Using Eq. 5.3 we have computed microlensed line profiles at different positions on the magnification pattern (Fig. 5.1). Different values for the inclination,

$i = 0°, 45°, 90°$, and the cone aperture half-angle, $\theta_{\rm c} = 10°, 30°$, are considered, as well as two different exponents for the velocity law, $p = 0.5, 2$.

Figure 5.3 corresponds to the $i = 0°$ case with a cone half-aperture of $\theta_{\rm c} = 30°$. The exponent of the velocity law, p, is 0.5 and 2.0 for the top and bottom panels, respectively. In this limiting case the bicone is projected along its axis and would appear projected as a circle of radius $r_{ex} \sin \theta_{\rm c}$. We obtain both strong amplification and significant deamplification of the line emission at different positions in the source plane.

Figure 5.4 corresponds to the $i = 90°$ case with a cone half-aperture of $\theta_{\rm c} = 30°$ (notice that now the main component of the velocity is perpendicular to the line of sight and the line profile has only one peak). In this other limiting case the bicone is projected perpendicular to its axis and would appear as a "bi-triangle". It is evident that for this inclination microlensing effects on the line profile depend on the orientation of the bicone axis with respect to the caustics when the source moves across the magnification pattern. In the absence of any privileged direction in the magnification pattern this would result in a random effect. However, in presence of shear, the orientation of the cone axis induces very interesting effects. In Fig. 5.4, for instance, a greater number of strong amplification events are found when the cone axis is parallel to the shear (lower panels) than when it is perpendicular (upper panels).

In Fig. 5.5 the bicone has an inclination of $i = 45°$. For the limiting geometries considered before ($i = 0°$ and $i = 90°$) there are no asymmetries induced by the microlensing in the line profile (Figs. 5.3 and 5.4). However, for any intermediate inclination microlensing induces relative enhancements between the blue and red parts of the profile depending on the position over the magnification map. It is even possible to obtain a line profile with one part of the line amplified and other part deamplified. Notice that microlensing effects also depend on the orientation of the projected cone axis with respect to the shear.

In the previous cases we have considered a rather wide cone aperture ($2 \cdot \theta_{\rm c} = 60°$). In the case of a narrower cone aperture ($2 \cdot \theta_{\rm c} = 20°$; see Fig. 5.6) the microlensing effects on the line profile can become extreme.

5.3 Comparison between the broad line region and continuum light curves

We assume a disc geometry for the region emitting the continuum radiation. We suppose this disc to have a uniform thickness, $h \ll r_{\rm in}$, and that the angle between its axis and the line of sight is i.

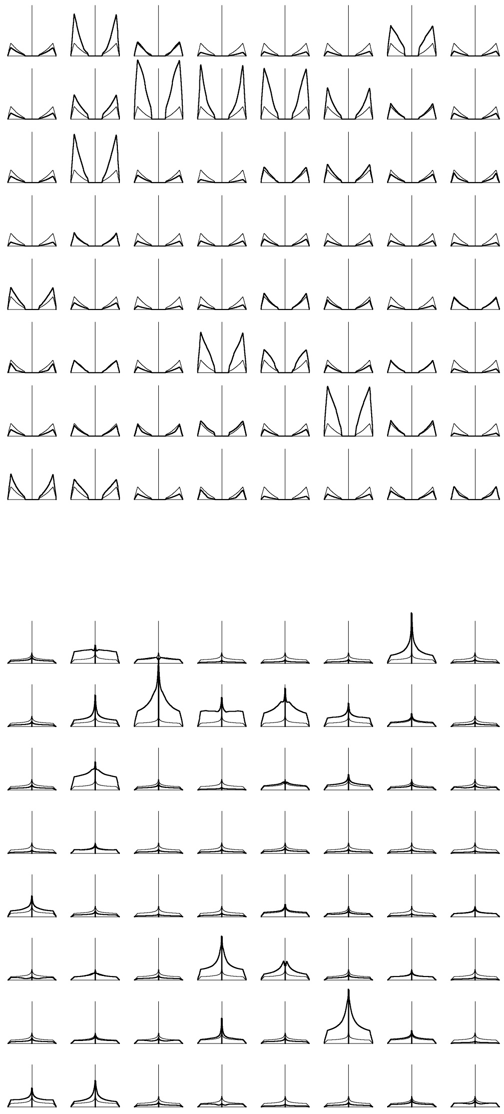

FIGURE 5.3— Biconical model with $i = 0°$, $\theta_c = 30°$, $p = 0.5$ for the top panel and $p = 2$ for the bottom panel. The heavy solid line is the amplified line profile and the lighter solid line is the line profile normalized to the mean amplification in the magnification map.

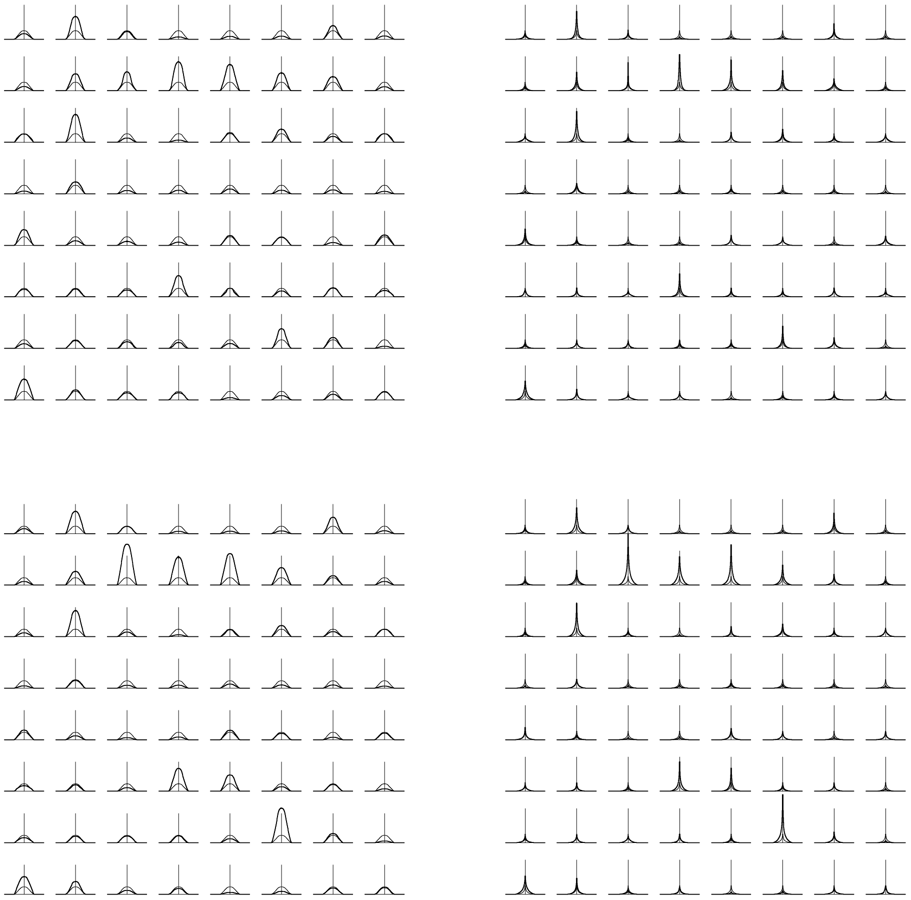

FIGURE 5.4— Biconical model with $i = 90°$, $\theta_c = 30°$, $p = 0.5$ for the left-hand panels and $p = 2$ for the right-hand panels. The perpendicular projections of the velocity correspond to the upper panels and the parallel projections correspond to the lower panels. The heavy solid line is the amplified line profile and the lighter solid line is the line profile normalized to the mean amplification in the magnification map.

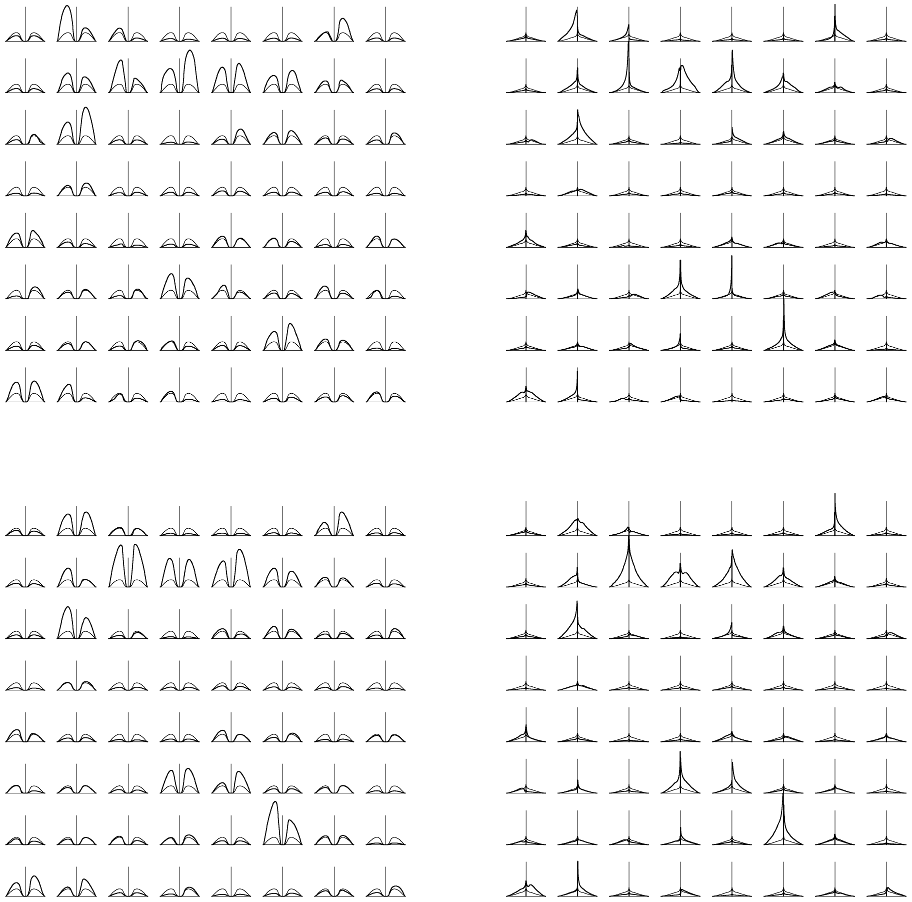

FIGURE 5.5— Biconical model with $i = 45°$, $\theta_c = 30°$, $p = 0.5$ for the left-hand panels and $p = 2$ for the right-hand panels. The perpendicular projections of the velocity correspond to the upper panels, the parallel projections correspond to the lower panels. The heavy solid line is the amplified line profile and the lighter solid line is the line profile normalized to the mean amplification in the magnification map.

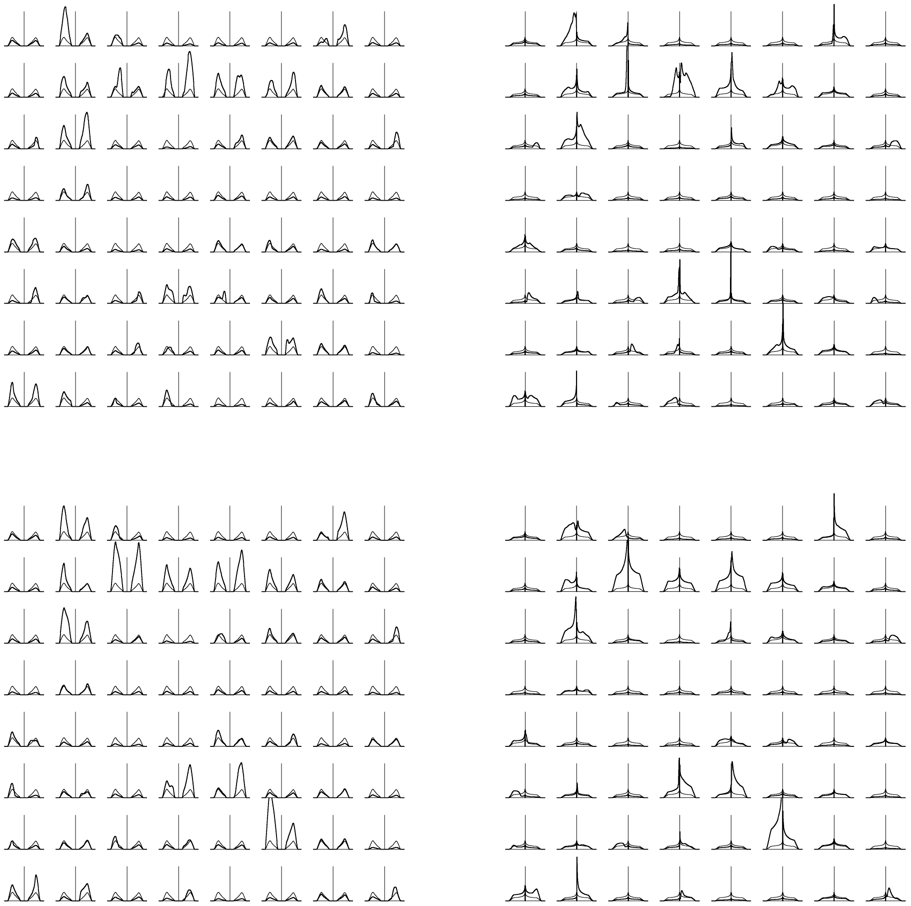

FIGURE 5.6— Same as in Fig. 5.5, but for $\theta_c = 10°$.

We adopt a brightness distribution for the continuum source,

$$I_{\rm ss}(r) = 2^{p_{\rm ss}} I_{\rm ss} \left(1 + \frac{r^2}{R_{\rm ss}^2}\right)^{-p_{\rm ss}} , \tag{5.6}$$

with a power-law index $p_{\rm ss} = 3/2$. This power-law model represents a rough version of the exact standard model (Shalyapin et al. 2002). Recent determinations by Kochanek (2004) (see also Shalyapin et al. 2002) indicate that the size of the continuum source is of about a few light days. We adopt a continuum radius of $0.096\eta_0$, i.e. a radius of 6 pixels over the magnification pattern that guarantee a good sampling for the continuum. This value corresponds to $r_{\rm cont} = 2.07$ l-days for B1600+434.

The microlensing light-curve of the continuum (or the BLR) is found by convolving the brightness profile of the source with the magnification map along the path of the source over the pattern. In the top left-hand panel of Fig. 5.7 several paths are plotted over the magnification pattern of B1600+434B. For the half-aperture of the cones we adopt $\theta_c = 30°$. In the top right-hand panel the light-curves for the BLR and continuum with $i = 0°$ are shown. The middle panels correspond to $i = 45°$ and the lower panels to $i = 90°$. Figure 5.8 is equivalent to Fig. 5.7, but with $\theta_c = 10°$. In these figures we see that the BLR amplification may be similar to or even greater than that of the continuum (BLR amplifications two magnitudes greater than the continuum ones can be found in the perpendicular cases). For inclinations different from $i = 0°$, the degree of correlation between both the BLR and continuum light-curves depends on the orientation of the projected bicone axis with respect to the shear. The correlation is strong when the projected bicone axis is parallel to the shear direction (left-hand panels in Figs. 5.7 and 5.8) but can be substantially reduced when it is perpendicular (right-hand panels in Figs. 5.7 and 5.8). To gain insight into this study (see Lewis & Ibata 2004), we have computed for each position (pixel) of the source in the magnification pattern pairs representing the BLR and continuum amplification, $(\mu_{\rm cont}, \mu_{\rm BLR})$. Color-scale histograms representing the frequency of these pairs (Lewis & Ibata 2004) for different values of inclination and cone aperture are represented in Figures 5.9 and 5.10. In Fig. 5.9 we confirm that the correlation is very strong for the case $i = 0°$, is less marked for the parallel to the shear projection of the bicone (cases $i = 45°$ and $i = 90°$), and is weaker for the perpendicular projection (cases $i = 45°$ and $i = 90°$). The probability of finding a microlensing event in a strip of $\mu_{\rm BLR} = \mu_{\rm cont} \pm 0.5$ decreases from 78% in the $i = 0°$ case to 65% in the $i = 90°$ perpendicular case. In the parallel case ($i = 90°$), the probability of finding a microlensing event in this strip is 71%. Similar results can be observed in Figure 5.10.

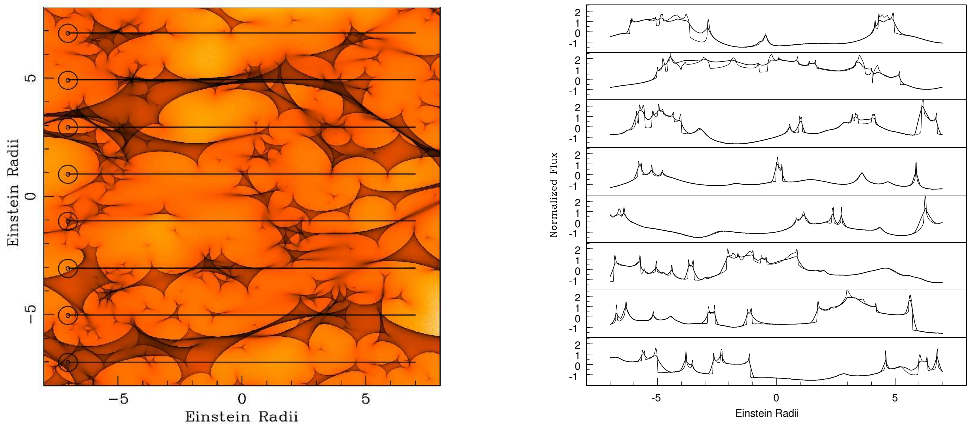

FIGURE 5.7— (a) Light-curves of the BLR and the continuum represented in solid and lighter solid lines, respectively. Each pair of light-curves is computed across different paths drawn in the left-hand panel, corresponding to the magnification map in Fig.5.1, where large circles represent the BLR with $r_{\rm ex} = 0.37\eta_0$, and small circles represent the continuum with $r_{\rm cont} = 0.096\eta_0$. The right-hand panel corresponds to the projection of the bicone with 0° and $\theta_{\rm c} = 30°$.

5.4 Is microlensing affecting the broad emission lines in SDSS J1004+ 4112?

BEL microlensing has been tentatively detected in the quadruple large-separation lensed quasar SDSS J1004+4112 (Inada et al. 2003). The quasar was discovered in the Sloan Digital Sky Survey (SDSS; York et al. 2000) and it is the first large-separation lensed quasar discovered (Fig. 5.11). Although gravitationally lensed galaxies (Colley, Tyson & Turner 1996) with large separations are known, quasars are more useful cosmological probes because of the simplicity of the resulting lens system. This gravitational lens consists of four lensed quasar components at $z_{\rm s} = 1.732$ with distances between components ranging from 3.″73 to 14.″62. Such a large separation means that the lensing object must be dominated by dark matter. In fact, the lensing object is a $z_{\rm l} = 0.68$ cluster centered among the four lensed images.

Blue-wing enhancements have been observed in the high ionization lines in component A spectra (Richards, Johnston & Hennawi 2004; Gómez-Álvarez et al. 2006). A first enhancement was detected in two epochs in May 2003 and was later undetectable in another four epochs from November to December 2003 (Richards et al. 2004). A second enhancement was independently detected in January 2004 (Gómez-Álvarez et al. 2006), March and April 2004

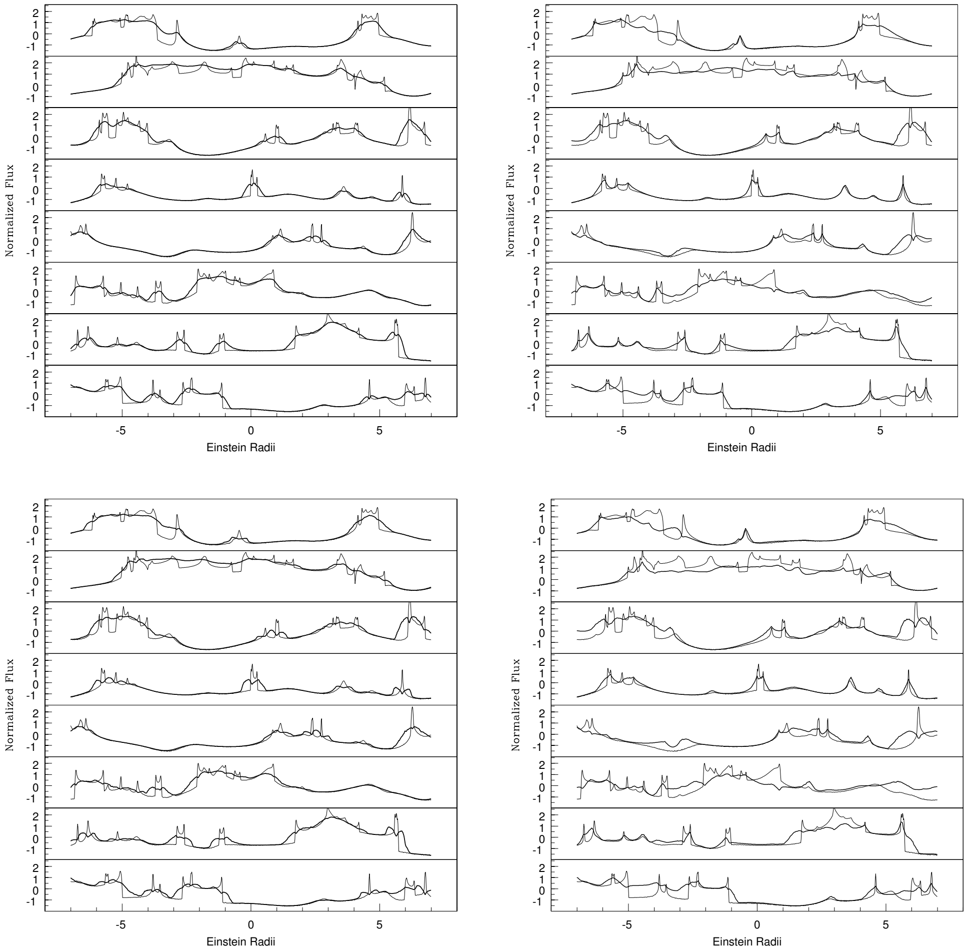

FIGURE 5.7 — (b) Light-curves of the BLR and the continuum represented in solid and lighter solid lines, respectively. Each pair of light-curves in each panel is computed across different paths drawn in the left-hand panel in Fig. 5.7a. The right-hand panels correspond to the perpendicular projection of the bicone, and the left-hand panels to the parallel projection. Inclination increases from top to bottom, with 45° and 90°. For all cases, $\theta_c = 30°$.

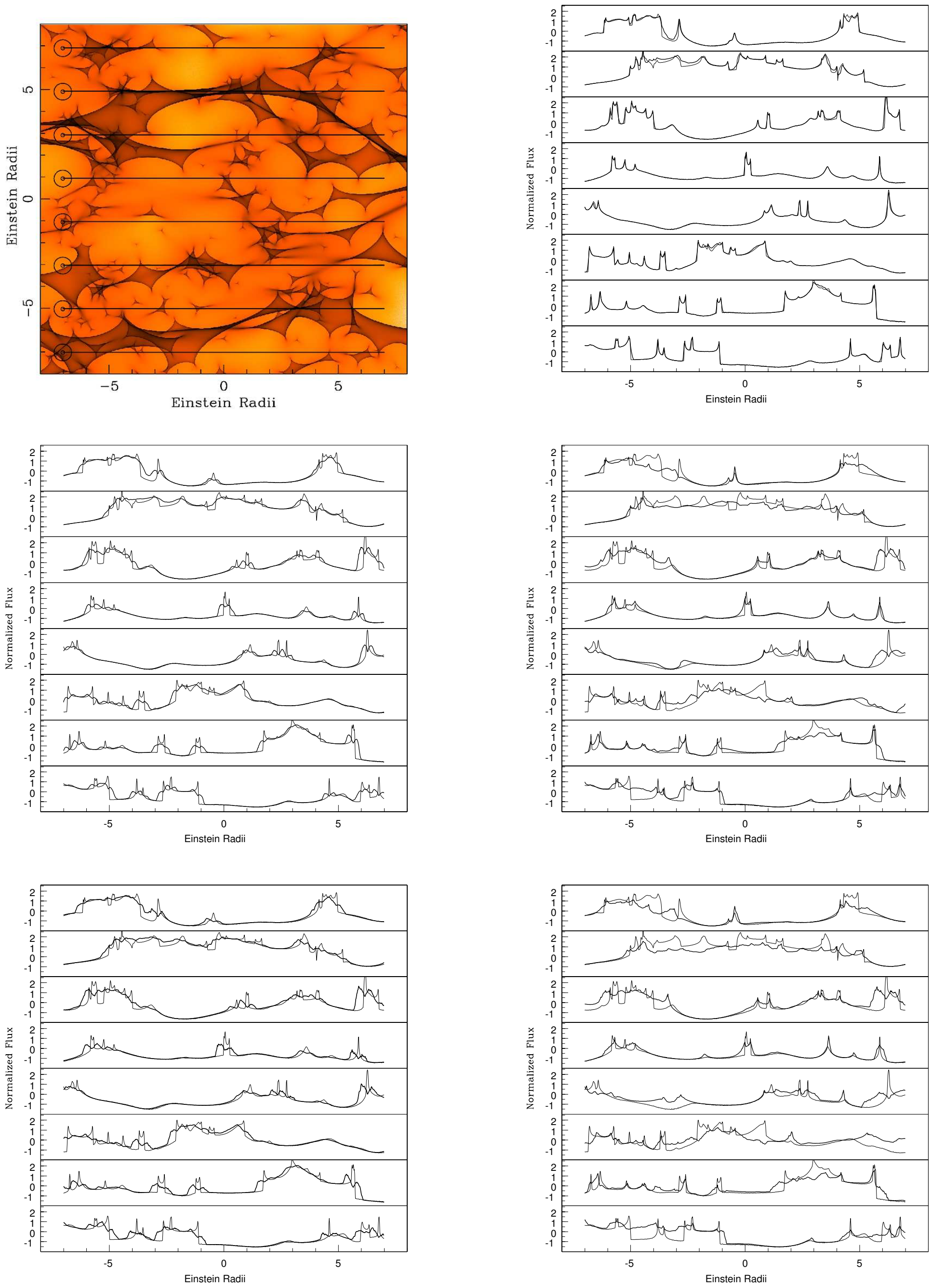

FIGURE 5.8— Same as in Fig. 5.7 a and b, but for $\theta_c = 10°$.

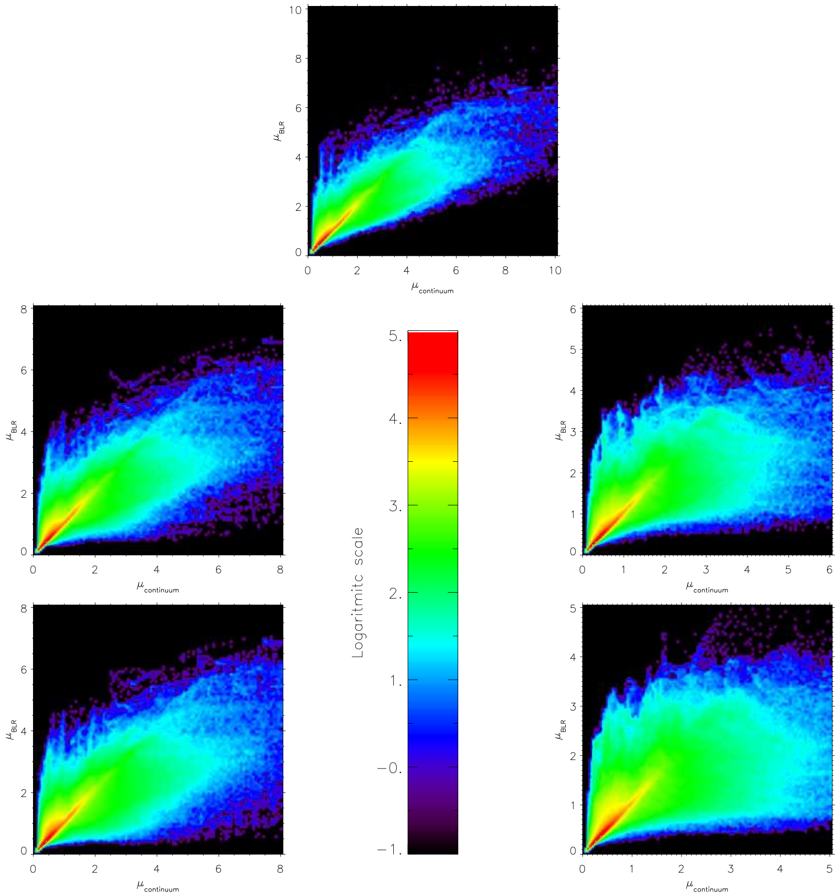

FIGURE 5.9— The correlation between the amplification of the BLR and the continuum when a biconical model is considered for the BLR and a Keplerian disc for the continuum is represented. The right-hand panels correspond to the perpendicular projection of the bicone and the left-hand panels to the parallel projection. Inclination increases from top to bottom, with 0°, 45° and 90°. For all cases, $\theta_c = 30°$.

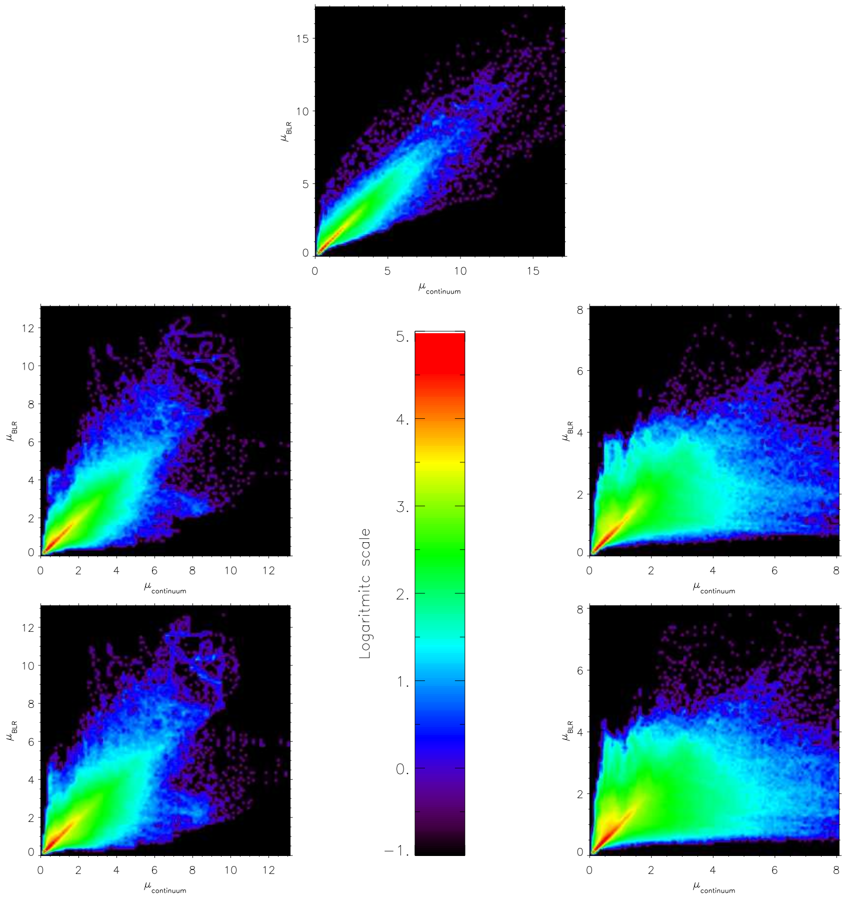

FIGURE 5.10— Same as in Fig. 5.9, but for $\theta_c = 10°$.

(Richards, Johnston & Hennawi 2004). In contrast, the continuum emission has been maintained unaltered throughout this period.

Microlensing of the high ionization BEL was the hypothesis originally preferred to explain variability (Richards et al. 2004). However this hypothesis seems difficult to reconcile with the recurrence of the blue-wing enhancement in the framework of the typical disc-like models for the BLR: instead of a new blueward enhancement, changes of the core or the red wing of the line were expected in so far as the caustic moves across the BLR velocity field. However,

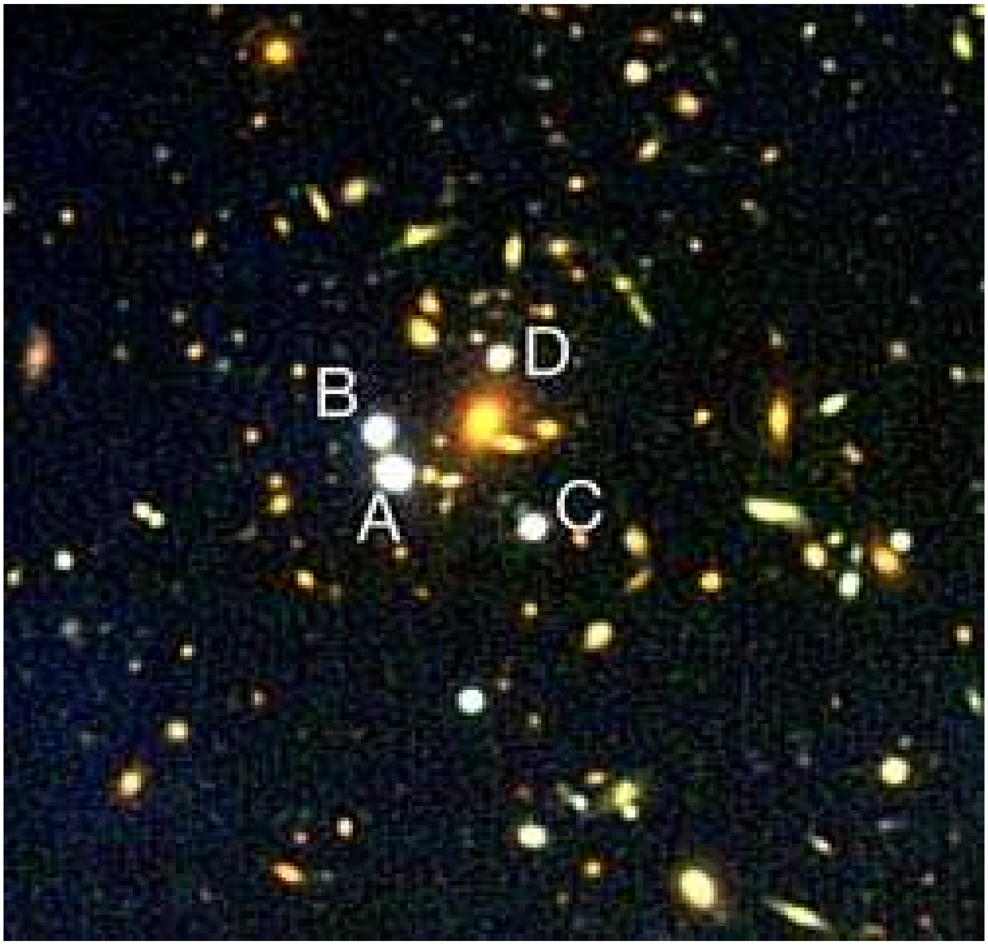

FIGURE 5.11— The light of this lensed quasar, SDSS J1004+4112, has been gravitationally split into four images (the four white dots in the center). The quasar is at $z_s = 1.732$ and the foreground lensing cluster is at $z_l = 0.68$.

this behaviour would not be so strange if a biconical geometry were adopted for the BLR. According to what we have previously seen for the case $i = 45°$ and orientation of the bicone axis perpendicular to the shear, one can imagine situations in which one of the projected cones (blue or red) could be amplified in more than one epoch without noticeable amplification of the other. In addition, the lack of correlation between the emission in the line and in the continuum is also another characteristic of the biconical model. A singular isothermal ellipsoid (SIE) model fitted to the positions of the four images of SDSS J1004+4112 reveals the presence of significant shear for image A ($\kappa = 0.39$, $\gamma = 0.64$).

In Figs 5.12 and 5.13 magnification maps for SDSS J1004+4112A corresponding to two different fractions of matter in stars with respect to the total mass (1% and 10%) are represented. An area of $500\xi_0 \times 500\xi_0$ was considered at the lens plane to compute a magnification pattern covering an area of $16\eta_0 \times 16\eta_0$ (1000×1000 pixels) at the source plane. 256 rays were shot per unlensed pixel, which means $2.5 \cdot 10^{11}$ rays traced between the observer and the source. The number of stars considered was 312 and 3121 for the 1% and 10% fractions of matter in stars, respectively. These values correspond to $\kappa_{\rm c} = 0.386$ (1%) and $\kappa_{\rm c} = 0.351$ (10%). The theoretical mean amplification, $< \mu_{th} >= |(1-\kappa)^2 - \gamma^2|^{-1}$, is 23.261 and the mean amplifications of the maps are 23.105 (1%) and 21.611 (10%), respectively. The most noticeable feature of both maps (Figures 5.12 and 5.13) is the characteristic pattern of alternating high and low amplification strips induced by the strong elongation of caustics in the direction of the shear.

We consider global displacements of the BLR parallel and transversal to the shear to try to reproduce the main features of the spectra variability in J1004+4112. The BLR radius for this quadruply imaged quasar is $r_{\rm BLR} = 7.57$ l-days for high ionization lines (using NGC 5548 as a reference object). In this gravitational lens $1\eta_0(1M_\odot) = 16.61$ l-days and, hence, $r_{ex} = 0.74\eta_0$. As in the case of B1600+434 the continuum radius is $0.096\eta_0$ (6 pixels over the magnification pattern), that corresponds to $r_{\rm cont} = 1.59$ l-days.

5.4.1 Parallel to the shear paths

In this case relative enhancements of any of the line profile peaks without noticeable continuum amplification are induced in a natural way by the presence of alternating strips of high and low amplification. We have computed BEL profiles with $r_{\rm ex} = 1.65\eta_0$, which means a more conservative value for the BLR size, $r_{\rm BLR} = 17$ l-days, or that the mass of stars in the lens is $0.2M_\odot$, with $1\eta_0(0.2M_\odot) = 7.43$ l-days. These profiles are convolved with the magnification pattern corresponding to a mass in stars amounting to 1% of the total mass

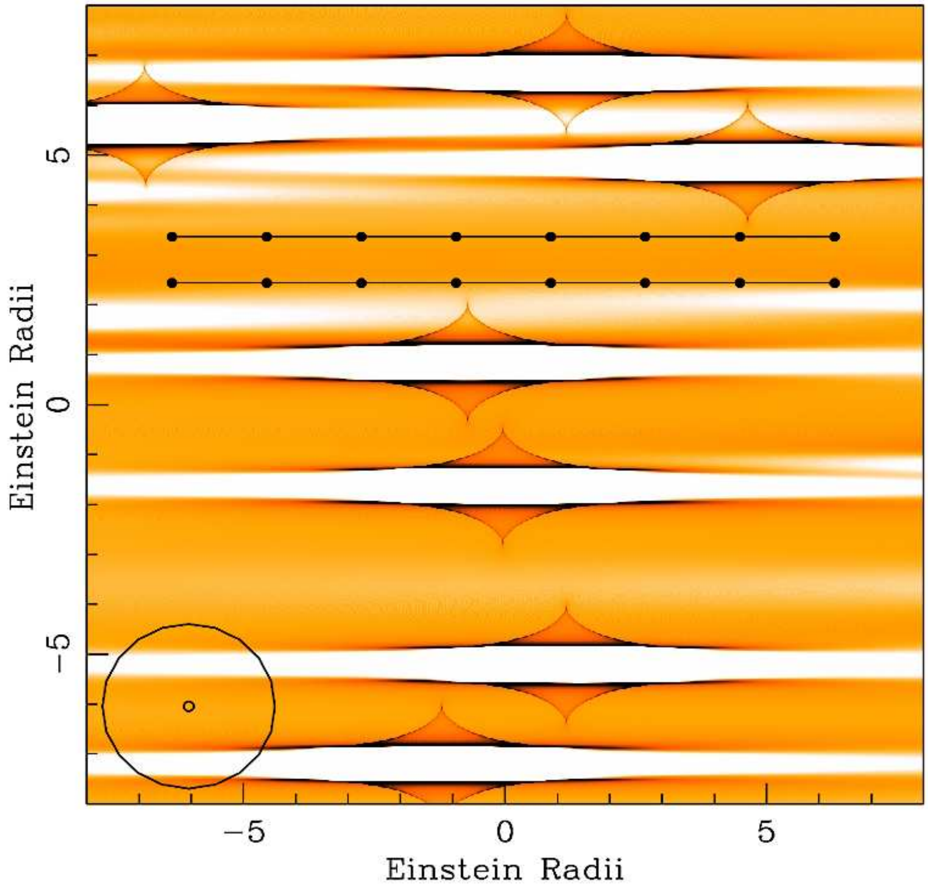

FIGURE 5.12— Magnification map for the A image of SDSS J1004+4112 for 1% of total mass in stars. Each point represents the BLR in different positions over the magnification map, and the lines are the paths over the map where the light-curves are computed. The largest circle represents the BLR with $r_{\rm ex} = 1.65\eta_0$, and the smallest circle represents the continuum with $r_{\rm cont} = 0.096\eta_0$.

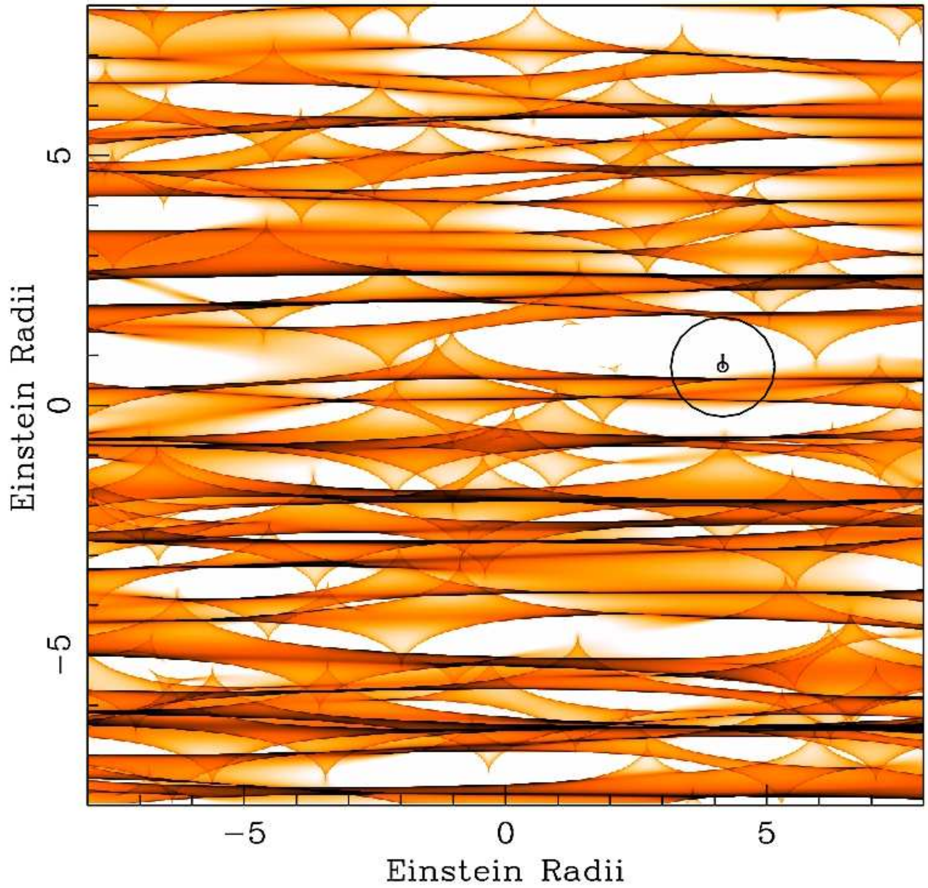

FIGURE 5.13— Magnification map for the A image of SDSS J1004+4112 for 10% of total mass in stars. The line is the path over the magnification pattern where the light-curves are computed. The largest circle represents the BLR with $r_{\rm ex} = 1\eta_0$, and the smallest circle represents the continuum with $r_{\rm cont} = 0.096\eta_0$.

(Fig. 5.12), following two different tracks over the pattern. As can be seen in Fig. 5.14, the continuum remains unaltered along the entire path. However, we face here the same problem as Richards et al. (2004): the enhancement event lasts several Einstein radii but according to the time estimates of Richards et al. (2004) it should last about one tenth of an Einstein radius (for $0.1 M_\odot$). In principle, to reduce the time-scale of an event (and also the lapse between events) we could increase the number of caustics by increasing the fraction of mass in stars. However, the caustic elongation in the shear direction is so strong that the time-scales of the events are not substantially reduced. The main effect of increasing the mass fraction in stars is to reduce the distance between consecutive strips in the magnification patterns.

5.4.2 Transversal to the shear paths

If the global displacement of the BLR is perpendicular to the shear, the time-scale of the events depends exactly on the separation between strips. In Fig. 5.15 we have represented the BEL profiles with $r_{\text{ex}} = 1\eta_0$ corresponding to 20×20 locations regularly distributed in the magnification pattern corresponding to a 10% mass fraction in stars (see Fig. 5.13). It is clear that a rich phenomenology of line profile variability (including recurrent or alternating enhancement of parts of the line profile) can be reproduced in relatively short displacements across the magnification pattern. It is not difficult to find paths to roughly reproduce two consecutive events of relative enhancement of one of the peaks without appreciable changes in the continuum. That considered in Fig. 5.16, for instance, implies a displacement across the pattern of 0.1 Einstein radii between the third and the sixth line profiles from left to right; that is, ~ 2 years with $v_\perp = 700\ \text{kms}^{-1}$ (Oguri et al. 2004), according to the estimates by Richards et al. (2004), but assuming $0.5 M_\odot$ stars in our case. Then the time between two consecutives line profiles is 0.62 years. The lapse of time between events of the order of 1 year can be obtained by considering that the mean mass of the stars is below $0.5 M_\odot$ or by supposing a factor two times greater relative velocity between the quasar host and the lens galaxy, or by combining both possibilities.

Figure 5.15 also illustrates other very noticeable effects that a high density of caustics (originated from the high amplification and shear of J1004+4112) can induce in the line profiles generated by a bicone transversally oriented and transversally moving with respect to the shear (and, hence, to the caustics). Because of the dependence of the velocity field with distance, each caustic will mainly affect emitters at a given velocity, enhancing a small part of the line profile. When more than one caustic affects the bicone, several “spikes” can be seen in the line profiles (see Fig. 5.15). The displacement of the bicone across the caustics would result in the scanning of the kinematic properties of the BLR.

Thus, the main trends of the spectral variability observed in J1004+4112 could be reproduced by the microlensing of a bicone moving transversally to the shear. The similarity of the computed phenomenon to the observed line variability can probably be improved by changing the proportion of matter in compact microlenses, by adjusting some of the model parameters (such as continuum and BLR sizes and separations) or by considering oblique paths.

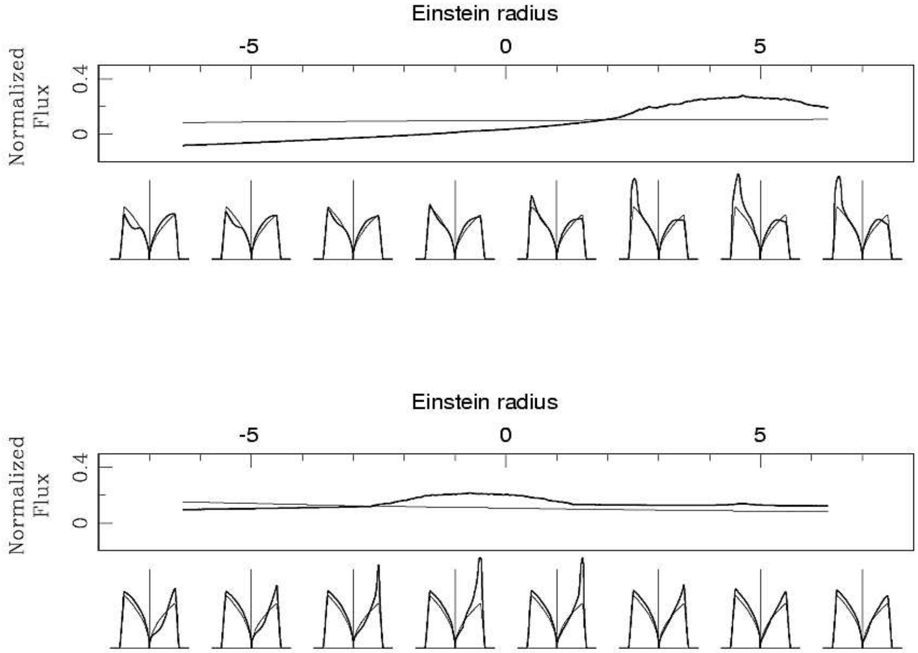

FIGURE 5.14— The line profiles for the BLR for each point and the light-curves for the BLR and the continuum for each path marked in Fig. 5.12 are shown. The parameters are $i = 45^\circ$, $\theta_c = 5^\circ$, $p = 2$, $r_{\rm cont} = 0.096\eta_0$ and $r_{\rm ex} = 1.65\eta_0$. In the line profile panels the heavy solid lines represent the amplified line profile and the lighter solid lines correspond to the line profile normalized to the mean amplification in the magnification map. In the light-curve panels the solid line represents the light-curve from the BLR and the lighter solid line corresponds to the light-curve from the continuum.

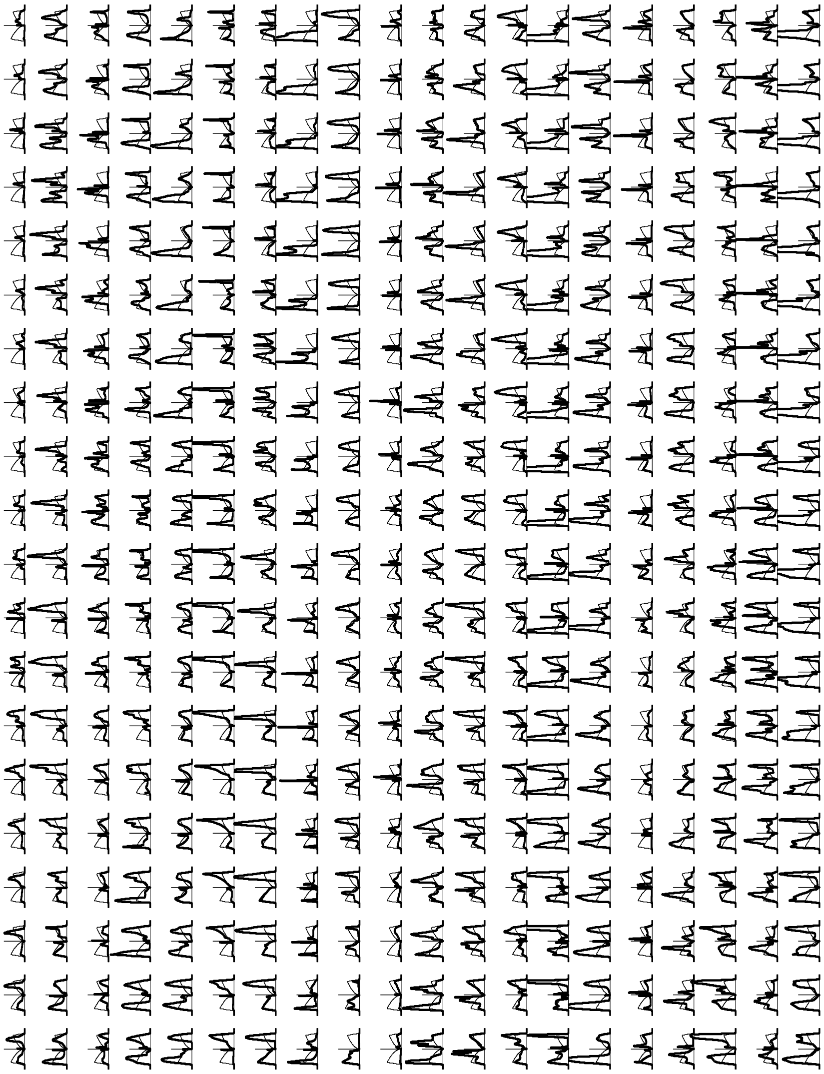

FIGURE 5.15— The BEL profiles for 20 × 20 locations regularly distributed in the magnification pattern (Fig. 5.13) are shown. The parameters are $i = 45°$, $\theta_c = 5°$, $p = 2$ and $r_{\rm ex} = 1\eta_0$. The heavy solid lines represent the amplified line profile and the lighter solid lines correspond to the line profile normalized to the mean amplification in the magnification map.

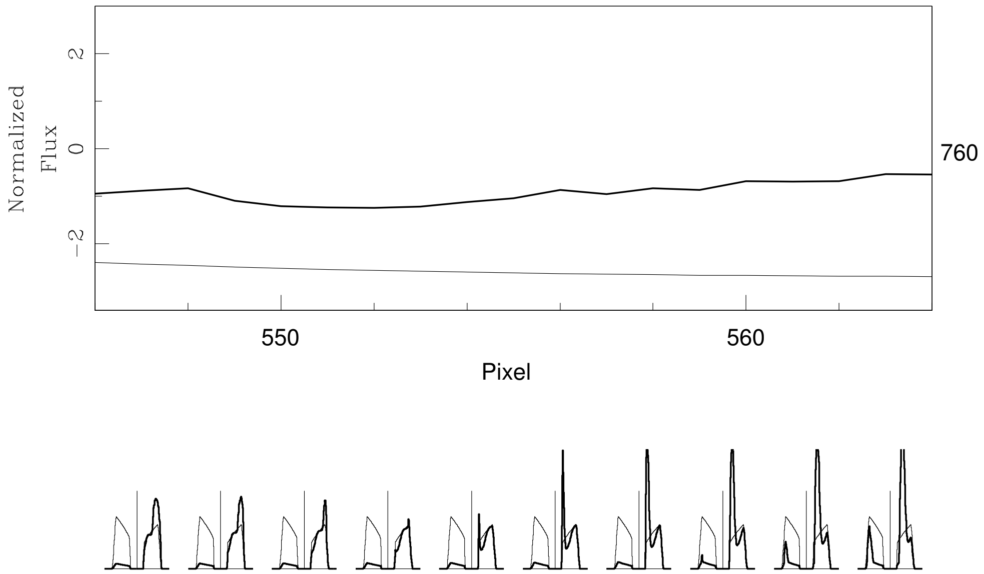

FIGURE 5.16— The line profiles for the BLR and the light-curves for the BLR and the continuum for a track superimposed on the magnification pattern (Fig. 5.13) are shown. The parameters are $i = 45°$, $\theta_c = 5°$, $p = 2$, $r_{\rm cont} = 0.096\eta_0$, $r_{\rm ex} = 1\eta_0$ and $r_{\rm in} = 0.55\eta_0$. In the line profile panel the heavy solid lines represent the amplified line profile and the lighter solid lines correspond to the line profile normalized to the mean amplification in the magnification map. In the light-curve panel the solid line represents the light curve from the BLR and the lighter solid line corresponds to the light-curve from the continuum.

5.5 Conclusions

We have explored the effects of microlensing at high optical depth on a biconical model of arbitrary inclination and aperture for the BLR. We point out some results that could be of interest:

1 - The luminosity weighted radius of a biconical region depends only on its intrinsic size along the cone axis. However, its projected area depends also on cone aperture and inclination. Thus, a biconical region of a large luminosity-weighted radius can have a small projected area if the cone aperture is small and the cone axis points toward the observer. This implies that very large amplifications, even greater than that of the continuum, are possible in microlensing events of a biconical BLR. For this geometry, a large luminosity-weighted radius measured by the reverberation method is not a definitive criterion to exclude significant microlensing amplification.

2 - For intermediate inclinations of the cone axis, $0° < i < 90°$, microlensing induces relative enhancements between the red and blue parts of the line profile.

3 - Microlensing effects (global amplification, wavelength-dependent amplification) are related to the orientation of the projected bicone with respect to the shear of the magnification pattern (this could result in quasi-periodic effects when the source moves along the magnification pattern). In particular, the correlation between the continuum and BLR light-curves can be weak when the axis of the projected bicones is perpendicular to the shear.

4 - When the bicone is oriented transversally to a caustic, the emission line profile can present a strong enhancement of a small wavelength region (spike). The movement of the bicone with respect to the caustic would scan the kinematics of the BLR. When the bicone lies in a caustic cluster, the emission line profile can be affected by several "spikes".

5 - The main features related to spectral variability detected in image A of SDSS J1004+4112 (recurrent blueward enhancement, absence of continuum variability and small time-scale) could be reasonably reproduced by the microlensing of a biconical BLR moving perpendicular to the shear if the mass fraction of the stars in the deflector is greater than 1 percent.

6

Conclusions and future work

Tu labor consiste en descubrir tu trabajo,
y luego entregarte a él de todo corazón.
Buda

In the light of recent discoveries concerning the BLR size and its scaling with AGN luminosity, currently accepted values for microlens masses and a variety of kinematic models for the BLR, we have revisited the influence of microlensing on the BEL at low and high optical depth, considering three relevant approximations: isolated microlens, straight fold caustic and caustic network. Some results are worth summarizing:

1. The global amplification of the BELs induced by microlensing events could be relevant, especially for high-ionization lines. Even for relatively small mass microlenses, the effects produced by the differential amplification of the line profile (relative enhancement of different parts of the line profile, line asymmetries, displacement of the peak of the line, etc.) would be easily detectable except for highly symmetric velocity fields. For intermediate inclinations of the biconical model, $0^\circ < i < 90^\circ$, microlensing induces relative enhancements between the red and blue parts of the line profile.

2. Current ideas about BLR size and stratification can be probed from the study of the changes that exit between the BEL profiles corresponding to microlensed and non-microlensed images, or among the BEL profiles of lines with different ionization in a microlensed image.

3. Although the straight fold caustic crossing is in general a crude approximation it is adequate when the size of the emission line region is small, as in the case of the Fe K_α line. It reproduces the main effects of microlensing amplification obtained in the case of an isolated lens.

4. Very large amplifications of BEL, even greater than that of the continuum, are possible in microlensing events of a biconical BLR. For this geometry, a large luminosity-weighted radius measured by the reverberation method does not exclude significant microlensing amplification.

5. The orientation of the projected bicone with respect to the shear of the magnification pattern is decisive in the phenomenology of microlensing. For instance, the correlation between the continuum and BLR light-curves is weak when the axis of the projected bicones is perpendicular to the shear. The kinematics of the BLR is scanned by the movement of the bicone transversally with respect to the caustic. We also found strong enhancements of a small wavelength region - "spikes" - in the BELs, when the bicone lies in a caustic cluster.

6. We have studied, under the hypothesis of microlensing, the main features related to spectral variability detected in image A of J1004+4112. We found that the recurrent blueward enhancement, the absence of continuum variability and the small time-scale could be reasonably reproduced by the microlensing of a biconical BLR moving perpendicular to the shear.

6.1 Work in progress

Our research work in microlensing is currently progressing along the following lines:

1. Improve the microlensing magnification patterns computation and implement more complex models for the BLR.

2. Extend the study for J1004+4112 to other gravitational lens systems.

3. Make the statistical studies deeper to get more realistic information about the probability that microlensing of BELs can occur.

4. Carry out observations with VLT or GTC of the high ionization lines on those systems where it is more probable to detect the variability of the broad emission lines.

A

Cosmology

> *La lectura es el último refugio*
> *para las personas proclives a la adicción.*
> Anónimo

A.1 Robertson-Walker metric and Friedmann models

We review in this appendix the standard cosmological model which is a homogeneous and isotropic solution of the field equations of General Relativity[1].

The background model is described by the Robertson-Walker metric (Robertson 1935; Walker 1935), in which hypersurfaces of constant time are homogeneous and isotropic three-spaces, either flat or curved, and change with time according to a scale factor which depends on time only. The dynamics of the scale factor are determined by two equations which follow from Einstein's field equations given the highly symmetric form of the metric.

Two postulates are fundamental to the standard cosmological model, which make the cosmological principle, and they are:

- When averaged over sufficiently large scales, there exists a mean motion of radiation and matter in the Universe with respect to which all averaged observable properties are isotropic;
- All fundamental observers, i.e. imagined observers who follow this mean motion, experience the same history of the Universe, i.e. the same averaged observable properties, provided they set their clocks suitably. Such a universe is called observer-homogeneous;

---

[1] General references on the cosmological model can be found in Weinberg (1972), Misner, Thorne & Wheeler (1973), Padmanabhan (1993), Peebles (1993) or Peacock (1999)

These postulates can be expressed mathematically as:

$$ds^2 = -dt^2 + a^2(t)\left[\frac{dr^2}{1-kr^2} + r^2(d\theta^2 + sen^2\theta d\phi^2)\right], \tag{A.1}$$

where $a(t)$ is a dimensionless time-varying scale factor and k is the value that determines the total curvature of the Universe, with $k = 1, 0, -1$ for a close, Euclidean and open universe, respectively; t is the time coordinate and r, θ and ϕ are the spatial coordinates. A metric of this form is called the Robertson-Walker metric.

To complete the description of space-time, we need to know how the scale factor $a(t)$ depends on time, and how the curvature k depends on the matter which fills space-time. Einstein's field equations relate the Einstein tensor G_{ij} to the stress-energy tensor T_{ij} of the matter,

$$G_{ij} = \frac{8\pi G}{c^4}T_{ij} + \Lambda g_{ij}, \tag{A.2}$$

with the second term being a generalization introduced by Einstein to allow static cosmological solutions of the field equations. Λ is called the cosmological constant. For finding exact solutions, this equation, which implies the knowledge of distribution of matter and energy in space-time, assumed that the matter and energy that fills the Universe can be treated as a perfect fluid. This assumption is called the Weyl condition and it implies that the energy-momentum can be described as:

$$T_{ij} = (\rho + p)u_i u_j - p g_{ij}, \tag{A.3}$$

so that the evolution of the density ρ and the pressure p in time depends on the metric tensor g_{ij} and the 4-velocity components u_i.

A cosmology based on the cosmological principle and the Weyl condition is called a Friedmann cosmology and the solutions obtained from Eq. A.2 with these constraints are called Friedmann models.

The Friedmann cosmology consist on two independent equations:

$$\left(\frac{\dot{a}}{a}\right)^2 = \frac{8\pi G}{3}\rho - \frac{kc^2}{a^2} + \frac{\Lambda c^2}{3}, \tag{A.4}$$

$$\frac{\ddot{a}}{a} = \frac{\Lambda}{3} - \frac{4}{3}\pi G\left(\rho + \frac{3p}{c^2}\right), \tag{A.5}$$

that relate scale factor $a(t)$ to the pressure p and density ρ. The relative expansion rate $(\dot{a}/a)$ is the rate at which the Universe is expanding. This quantity is called the Hubble parameter, $H = (\dot{a}/a)$ and its value at the present epoch $t = t_0$ is the Hubble constant, $H(t_0) = H_0$. The scale factor $a(t)$ is determined once its value at one instant of time is fixed.

These two equations (Eqs. A.4, A.5) can be written in terms of some density parameters, a matter term, a cosmological constant term and a curvature term as:

$$\Omega_M + \Omega_\Lambda + \Omega_k = 1, \tag{A.6}$$

where

$$\Omega_M = \frac{8\pi G}{3H_0^2}\rho_0, \qquad \Omega_\Lambda = \frac{\Lambda c^2}{3H_0^2}, \qquad \Omega_k = -\frac{kc^2}{a_0^2 H_0^2}, \tag{A.7}$$

and the subindex “0” corresponds to present time t_0.

In this kind of cosmology we have a special combination of parameters called critical density of the Universe:

$$\rho_{cr} = \frac{3H_0^2}{8\pi G}, \tag{A.8}$$

which means a limit density so that the Universe is:

- Geometrically closed for $\rho < \rho_{cr}$, which means that the expansion of the Universe will stop and contraction will start $(k < 0)$.

- Geometrically flat for $\rho = \rho_{cr}$, which means that the expansion goes asymptotically to zero. $(k = 0)$.

- Geometrically open for $\rho > \rho_{cr}$, which means that the expansion of the Universe goes on forever $(k > 0)$.

A.2 Redshift and cosmological distances

The redshift z of an object is the shift in wavelength that a photon suffers because of the expansion of the Universe since it was emitted at a time t_e from a distant object with a wavelength λ_e until it is received at present time t_0 with a wavelength λ_0, as:

$$z = \frac{\lambda_0 - \lambda_\mathrm{e}}{\lambda_\mathrm{e}} = \frac{a(t_0) - a(t_\mathrm{e})}{a(t_\mathrm{e})}, \tag{A.9}$$

where $a(t_0)$ is the scale factor or the “size” of the Universe at the time the light from the object is observed, and $a(t_\mathrm{e})$ is the size at the time it was emitted.

Redshift is almost always determined with respect to us, but it is possible to define the redshift z_{12} between objects 1 and 2, both of which are cosmologically redshifted relative to us: the redshift z_{12} of an object at redshift z_2 relative to a hypothetical observer at redshift z_1, with $z_1 < z_2$, is given by:

$$z_{12} = \frac{a(t_1) - a(t_2)}{a(t_2)} = \frac{z_2 - z_1}{1 + z_1}. \tag{A.10}$$

The redshift of a source is used as a measure of its distance to us, so we need a definition of distance as a function of redshift. However, the meaning of "distance" is no longer unique in a curved space-time. We define four different distance scales, the proper distance, the comoving distance, the angular diameter distance, and the luminosity distance (Batermann & Schneider 2001;Blandford & Narayan 1992).

The line-of-sight comoving distance, D, between two nearby object in the Universe is the distance between them, which remains constant with epoch if the two objects are moving with the Hubble flow (i.e. the expansion), so it is the distance between them which would be measured with rulers at the time they are being observed (proper distance) divided by the ratio of the scale factor of the Universe then to now; it is the proper distance multiplied by $(1 + z)$:

$$D = \frac{c}{H_0} \int_{z_1}^{z_2} \left[\Omega_M (1+z)^3 + \Omega_k (1+z)^2 + \Omega_\Lambda\right]^{-1/2} dz. \tag{A.11}$$

The comoving distance, D_M, between two nearby object in the Universe at the same redshift or distance but separated in the sky by some angle $\delta\theta$, is related to the line of sight comoving distance D as:

$$D_M = \begin{cases} \frac{c}{H_0\sqrt{\Omega_k}} \sinh[\sqrt{\Omega_k} D \frac{H_0}{c}] & \text{for } \Omega_\mathrm{k} > 0, \\ D & \text{for } \Omega_\mathrm{k} = 0, \\ \frac{c}{H_0\sqrt{|\Omega_k|}} \sin[\sqrt{|\Omega_k|} D \frac{H_0}{c}] & \text{for } \Omega_\mathrm{k} < 0. \end{cases} \tag{A.12}$$

The angular diameter distance, D_A, is defined, in analogy to the relation in a Euclidean space, as the ratio of an object's physical transverse size to its angular size (in radians).

The luminosity distance, D_L, is defined, like in a Euclidean space, by the relationship between the flux S received at z_1 and the luminosity L of a source at z_2 as $D_L = \sqrt{L/(4\pi S)}$, and this is related to the comoving distance, D_M, and the angular diameter distance, D_A, by:

$$D_L = \frac{1 + z_2}{(1 + z_1)^2} D_M = \frac{(1 + z_2)^2}{(1 + z_1)^2} D_A, \tag{A.13}$$

and when subindex 1 corresponds to present time, which means $z_1 = 0$, we recover the well known expression:

$$D_L = (1+z)D_M = (1+z)^2 D_A. \tag{A.14}$$

If we consider $k = 0$, i.e. a flat cosmology (Euclidean space), Eq. A.11 is reduced to

$$D_M = D_P = \frac{c}{H_0} \int_{z_1}^{z_2} \left[(1+z)^2(1+\Omega_M z) - z(2+z)(1-\Omega_M)\right]^{-1/2} dz, \tag{A.15}$$

with $\Omega_M + \Omega_\Lambda = 1$. If besides $k = 0$, $\Lambda = 0$, which is called the Einstein-de-Sitter model, then,

$$D_M = D_P = \frac{2c}{H_0} \left[(1+z_1)^{-1/2} - (1+z_2)^{-1/2}\right]. \tag{A.16}$$

B

Modeling the broad line region by an isolated microlens

Todos los días,
en todos los sentidos,
yo progreso más y más.
Emile Coué

Nowadays, there is no generally accepted model for the geometry and dynamics of the broad line region. So, we adopt the discrete cloud model (see Robinson 1995) in which it is assumed that the magnitude of the velocity and the volume emissivity may be independently specified by a power law. It is also assumed that the clouds or volume elements emit line radiation isotropically.

The amplified line profile produced by the system is obtained from:

$$F_\lambda = \int_V \epsilon(r)\ \delta\left[\lambda - \lambda_0\left(1 + \frac{v_{||}}{c}\right)\right]\mu(\vec{r})dV, \tag{B.1}$$

where the integral is taken over the total volume occupied by the clouds, $\mu(\vec{r})$ is the relative amplification that the microlens produces over the line profile, and $v_{||}$ is the projection of the velocity field along the line of sight. Finally, $\epsilon(r)$ is the volume emissivity of the clouds:

$$\epsilon(r) = \epsilon_0\left(\frac{r}{r_{\rm in}}\right)^\beta, \tag{B.2}$$

with $r_{\rm in}$ being the inner radius of the cloud system.

The geometry of the BLR is unknown, but it seems plausible that its overall structure could be characterized by one of three basic symmetries: spherical, conical, or cylindrical (Robinson 1995).

B.1 Spherical shell

Let us first consider a spherically symmetric cloud ensemble of outer radius $r_{\rm BLR}$, which is characterized by a radial velocity field. The component of the velocity parallel to the line of sight is (Robinson 1995):

$$v_{||} = v_0 \left(\frac{r}{r_{\rm in}}\right)^p \cos\theta \quad (p > 0). \tag{B.3}$$

If the microlens is placed at $\vec{r_0} \sim (r_0, \varphi_0)$ and the Einstein radius is η_0, the relative amplification is given by (e.g., Schneider et al. 1992):

$$\mu(\vec{r}) = \frac{u^2+2}{u\sqrt{u^2+4}}, \qquad u = \frac{|\vec{r}-\vec{r_0}|}{\eta_0}\ , \tag{B.4}$$

$$|\vec{r}-\vec{r_0}| = \left[(r\sin\theta\cos\varphi - r_0\cos\varphi_0)^2 + (r\sin\theta\sin\varphi - r_0\sin\varphi_0)^2\right]^{\frac{1}{2}}. \tag{B.5}$$

To compute the integral in Eq. B.1 we define:

$$f \equiv \lambda - \lambda_0 \left[1 + \frac{v_0}{c}\left(\frac{r}{r_{\rm in}}\right)^p \cos\theta\right]. \tag{B.6}$$

Equation B.1 appears, when the integral in the θ dimension is done and the parameters $x = c\ (\lambda - \lambda_0)/(v_{\rm max}\lambda_0)$ and $x_{\rm m} = v_0/v_{\rm max} = (r_{\rm in}/r_{\rm BLR})^p$ are defined, as:

$$F_x = \begin{cases} \int_0^{2\pi}\int_{{\rm Max}[r_{\rm lim}, r_{\rm in}]}^{r_{\rm BLR}} \epsilon(r) r^2 \frac{[\mu(x,\vec{r})]_{\rm f=0}}{[\frac{\rm df}{d\theta}]_{\rm f=0}} [\sin\theta]_{\rm f=0} dr d\varphi & \\ \qquad\qquad\qquad\qquad\qquad\qquad \text{for } r_{\rm lim} < r_{\rm BLR}, & \\ 0 \qquad\qquad\qquad\qquad\qquad\qquad \text{for } r_{\rm lim} > r_{\rm BLR}, & \end{cases} \tag{B.7}$$

with

$$[\cos\theta]_{\rm f=0} = \frac{x}{x_{\rm m}}\left(\frac{r}{r_{\rm in}}\right)^{-p}, \tag{B.8}$$

$$[\sin\theta]_{\rm f=0} = +\sqrt{1 - [\cos\theta]^2_{\rm f=0}}\ , \tag{B.9}$$

and

$$\left[\frac{\rm df}{d\theta}\right]_{\rm f=0} = \lambda_0 \frac{v_0}{c}\left(\frac{r}{r_{\rm in}}\right)^p [\sin\theta]_{\rm f=0}\ , \tag{B.10}$$

where $[\mu(x,\vec{r})]_{\mathrm{f}=0}$ is given by Eq. B.4, inserting Eq. B.9 into Eq. B.5 as:

$$\begin{aligned} |\vec{r}-\vec{r}_0|_{\pm,\mathrm{f}=0} &= \Big[(r[\sin\theta]_{\mathrm{f}=0}\cos\varphi - r_0\cos\varphi_0)^2 + \\ &\quad +(r[\sin\theta]_{\mathrm{f}=0}\sin\varphi - r_0\sin\varphi_0)^2\Big]^{\frac{1}{2}}, \end{aligned} \tag{B.11}$$

and $r_{\mathrm{lim}} = r_{\mathrm{in}}\ (|x|/x_{\mathrm{m}})^{1/p}$. The expression of r_{lim} is obtained from the delta condition.

B.2 Biconical shell

In this case, the broad lines are emitted by a bipolar flow in which clouds moving radially outward are confined to a pair of oppositely directed cones, whose common axis passes through the optical axis. In general, an individual cloud measured with respect to the cone axis has a projected velocity (Robinson 1995):

$$\begin{aligned} &v_{||} = v_0\left(\tfrac{r}{r_{\mathrm{in}}}\right)^p \xi \quad (p>0), \\ &\xi = \sin\theta\sin\varphi\sin i + \cos\theta\cos i, \end{aligned} \tag{B.12}$$

where i represents the inclination of the axis with respect to the line of sight. For this system, the amplified line profile is:

$$\begin{aligned} F_\lambda &= \int_0^{2\pi}\int_{r_1}^{r_2}\left[\int_0^{\theta_{\mathrm{c}}} + \int_{\pi-\theta_{\mathrm{c}}}^{\pi}\right]\epsilon(r)\ \delta\left[\lambda-\lambda_0\left(1+\frac{v_{||}}{c}\right)\right] \mathrm{x} \\ &\quad \mathrm{x}\quad \mu(\vec{r})\ r^2\ \sin\theta\ d\theta\ dr\ d\varphi, \end{aligned} \tag{B.13}$$

where the amplification is given by Eq. B.4, with:

$$\begin{aligned} |\vec{r}-\vec{r}_0| &= \Big[(r\sin\theta\cos\varphi - r_0\cos\varphi_0)^2 + \\ &+ \quad (r\sin\theta\sin\varphi\cos i - r\cos\theta\sin i - r_0\sin\varphi_0)^2\Big]^{\frac{1}{2}}. \end{aligned} \tag{B.14}$$

To compute the integral in Eq. B.13, we define f as:

$$f \equiv \lambda - \lambda_0\left[1+\frac{v_0}{c}\left(\frac{r}{r_{\mathrm{in}}}\right)^p\xi\right], \tag{B.15}$$

and then, after integrating in the r dimension and adopting $x = c\ (\lambda-\lambda_0)/$-$(v_{\max}\lambda_0)$ and $x_{\mathrm{m}} = v_0/v_{\max} = (r_{\mathrm{in}}/r_{\mathrm{BLR}})^p$, Eq. B.13 becomes:

$$F_x = \begin{cases} \int\limits_0^{2\pi}\left(\left[\int\limits_0^{\theta_{\mathrm{c}}} + \int\limits_{\pi-\theta_{\mathrm{c}}}^{\pi}\right]\left[\epsilon(r)r^2\mu(x,\vec{r})\left(\frac{\mathrm{df}}{dr}\right)^{-1}\right]_{\mathrm{f}=0}\sin\theta d\theta\right)d\varphi & \\ & \text{for } x_{\mathrm{m}}|\xi| < |x| < |\xi|, \\ 0 & \text{in other cases.} \end{cases} \tag{B.16}$$

Moreover,

$$[r]_{\mathrm{f=0}} = r_{in} \left(\frac{x}{\xi x_{\mathrm{m}}} \right)^{1/p}, \tag{B.17}$$

and

$$\left[\frac{\mathrm{df}}{\mathrm{dr}} \right]_{\mathrm{f=0}} = \left| -\frac{\lambda_0 \; p \; v_0}{r_{in} \; c} \left(\frac{[r]_{\mathrm{f=0}}}{r_{\mathrm{in}}} \right)^{p-1} \xi \right|. \tag{B.18}$$

$[\mu(x,\vec{r})]_{\mathrm{f=0}}$ is given by Eq. B.4, inserting Eq. B.17 into Eq. B.14 as:

$$\begin{aligned} |\vec{r}-\vec{r}_0|_{\mathrm{f=0}} = & \Big[([r]_{\mathrm{f=0}} \sin\theta \cos\varphi - r_0 \cos\varphi_0)^2 + \\ & + ([r]_{\mathrm{f=0}} \sin\theta \sin\varphi \cos i - [r]_{\mathrm{f=0}} \cos\theta \sin i - r_0 \sin\varphi_0)^2 \Big]^{\frac{1}{2}}. \end{aligned} \tag{B.19}$$

B.2.1 $i = 0^\circ$ Case

The $i = 0^\circ$ case leads to the amplified line profile:

$$F_x = \begin{cases} \int_0^{2\pi} \int_{\mathrm{Max}[r_{\mathrm{lim}}, r_{\mathrm{in}}]}^{\mathrm{Min}[r_{\mathrm{sup}}, r_{\mathrm{BLR}}]} \epsilon(r) r^2 \frac{[\mu(x,\vec{r})]_{\mathrm{f=0}}}{[\frac{\mathrm{df}}{d\theta}]_{\mathrm{f=0}}} [\sin\theta]_{\mathrm{f=0}} dr d\varphi & \\ \qquad \text{for } r_{\mathrm{lim}} < r_{\mathrm{BLR}} \text{ and } r_{\mathrm{sup}} > r_{\mathrm{in}}, & \\ 0 \qquad \text{in the other cases,} & \end{cases} \tag{B.20}$$

in a similar way to the spherical shell because Eqs. B.3 and B.12 are the same expression. Besides $[\sin\theta]_{\mathrm{f=0}}$ and $[df/d\theta]_{\mathrm{f=0}}$ are given by Eqs. B.9 and B.10, $[\mu(x,\vec{r})]_{\mathrm{f=0}}$ is given by Eq. B.4, inserting Eq. B.9 into Eq. B.11, with $r_{\mathrm{lim}} = r_{\mathrm{in}} \; (|x|/x_{\mathrm{m}})^{1/p}$, and $r_{\mathrm{sup}} = r_{\mathrm{BLR}} \; (|x|/\cos\theta_{\mathrm{c}})^{1/p}$. The expressions of r_{lim} and r_{sup} can be inferred from delta conditions.

B.2.2 $i = 90^\circ$ Case

In the $i = 90^\circ$ case we consider a projected velocity of

$$v_{||} = v_0 \left(\frac{r}{r_{\mathrm{in}}} \right)^p \sin\theta \sin\varphi \quad (p > 0). \tag{B.21}$$

Let us now compute f in Eq. B.15 as:

$$f \equiv \lambda - \lambda_0 \left[1 + \frac{v_0}{c} \left(\frac{r}{r_{\mathrm{in}}} \right)^p \sin\theta \sin\varphi \right], \tag{B.22}$$

and then, after integrating in the φ dimension and adopting $x = c\ (\lambda - \lambda_0)/$-$(v_{\rm max}\lambda_0)$ and $x_{\rm m} = v_0/v_{max} = (r_{\rm in}/r_{\rm BLR})^p$, Eq. B.13 becomes:

$$F_x = \int\limits_{{\rm Max}[r_{\rm lim},r_{\rm in}]}^{r_{\rm BLR}} \left(\left[\int\limits_{\theta_{\rm lim}}^{\theta_{\rm c}} + \int\limits_{\pi-\theta_{\rm c}}^{{\rm Min}[\pi-\theta_{\rm lim},\pi]} \right] g(x,r,\theta) d\theta \right) dr, \tag{B.23}$$

where

$$g(x,r,\theta) = \begin{cases} \epsilon(r) r^2 \sin\theta \frac{[\mu_+(x,\vec{r})+\mu_-(x,\vec{r})]_{\rm f=0}}{[\frac{\rm df}{d\varphi}]_{-,\rm f=0}} & \text{for } \theta > \theta_{\rm lim}, \\ 0 & \text{in other cases,} \end{cases} \tag{B.24}$$

with $\theta_{\rm lim} = \arcsin[(|x|/x_{\rm m})(r/r_{\rm in})^{-p}]$. The expression of $\theta_{\rm lim}$ is inferred from delta conditions. Moreover,

$$[\sin\varphi]_{\rm f=0} = \frac{x}{x_{\rm m}} \left(\frac{r}{r_{\rm in}}\right)^{-p} \frac{1}{\sin\theta}\ , \tag{B.25}$$

$$[\cos\varphi]_{\pm,\rm f=0} = \pm\sqrt{1 - [\sin\varphi]^2_{\rm f=0}}\ , \tag{B.26}$$

and

$$\left[\frac{\rm df}{d\varphi}\right]_{\pm,\rm f=0} = -\lambda_0 \frac{v_0}{c} \left(\frac{r}{r_{\rm in}}\right)^p \sin\theta\ [\cos\varphi]_{\pm,\rm f=0}\ . \tag{B.27}$$

$[\mu_\pm(x,\vec{r})]_{\rm f=0}$ is given by Eq. B.4, inserting Eq. B.26 into Eq. B.14 as

$$\begin{aligned} |\vec{r} - \vec{r}_0|_{\pm,\rm f=0} &= \Big[(r\sin\theta[\cos\varphi]_{\pm,\rm f=0} - r_0\cos\varphi_0)^2 + \\ &+ (r\cos\theta + r_0\sin\varphi_0)^2\Big]^{\frac{1}{2}}. \end{aligned} \tag{B.28}$$

B.3 Cylindrical shell

The simplest example of cylindrical symmetry is a plane, i.e., a thin disc. We will suppose that this disc has uniform thickness, $h \ll r_{\rm in}$, and that the angle between its axis and the line of sight is i. Finally, any point in the disc is assumed to follow a circular orbit about the axis, thus giving a line of sight velocity of (Robinson 1995):

$$v_{||} = v(r)\ \cos\varphi\sin i, \tag{B.29}$$

where r and φ are polar coordinates of an emitter in the disc.

For this system, the amplified line profile is

$$F_\lambda = \int_S \epsilon(r)\ \delta \left[\lambda - \lambda_0 \left(1 + \frac{v_\|}{c}\right)\right] \mu(\vec{r})\ dS. \tag{B.30}$$

Let us now define f as:

$$f \equiv \lambda - \lambda_0 \left[1 + \frac{v(r) \cos\varphi \sin i}{c}\right], \tag{B.31}$$

and $x = c\ (\lambda - \lambda_0)/(v_{\rm max}\lambda_0)$, with $v_0 = v_{\rm max}$. Then, when the integral in the φ dimension is done, Eq. B.30 becomes:

$$F_x = \begin{cases} \int_{r_{\rm in}}^{{\rm Min}[r_{\rm lim}, r_{\rm BLR}]} \epsilon(r) r \frac{[\mu_+(x,\vec{r}) + \mu_-(x,\vec{r})]_{\rm f=0}}{[\frac{df}{d\varphi}]_{+,{\rm f=0}}} dr & \text{for } r_{\rm lim} > r_{\rm in}, \\ 0 & \text{for } r_{\rm lim} < r_{\rm in}, \end{cases} \tag{B.32}$$

where

$$[\cos\varphi]_{\rm f=0} = x \frac{v_0}{v(r) \sin i}\ , \tag{B.33}$$

$$[\sin\varphi]_{\pm,{\rm f=0}} = \pm\sqrt{1 - [\cos\varphi]^2_{\rm f=0}}\ , \tag{B.34}$$

and

$$\left[\frac{df}{d\varphi}\right]_{\pm,{\rm f=0}} = \lambda_0 \frac{v(r) \sin i}{c}\ [\sin\varphi]_{\pm,{\rm f=0}}\ . \tag{B.35}$$

$[\mu_\pm(x,\vec{r})]_{\rm f=0}$ is given by Eq. B.4, inserting the expressions of $[\cos\varphi]_{\rm f=0}$ and $[\sin\varphi]_{\rm f=0}$ (Eqs. B.33 and B.34) into:

$$\begin{aligned} |\vec{r} - \vec{r}_0|_{\pm,{\rm f=0}} &= \Big[(r[\cos\varphi]_{\rm f=0} \cos i - r_0 \cos\varphi_0)^2 + \\ &+ (r[\sin\varphi]_{\pm,{\rm f=0}} - r_0 \sin\varphi_0)^2\Big]^{\frac{1}{2}}, \end{aligned} \tag{B.36}$$

and $r_{\rm lim}$ is defined by the condition:

$$v(r_{\rm lim}) = v_0 \frac{|x|}{\sin i}\ . \tag{B.37}$$

Bibliography

Abajas, C., Mediavilla, E., Muñoz, J. A., Popović, L. Č. & Oscoz, A. 2002, ApJ, 576, 640

Abajas, C. 2005, In *25 Years After the Discovery: Some Current Topic on Lensed QSOs*, http://grupos.unican.es/glendama/e-Proc.htm, p24

Abajas, C., Mediavilla, E., Muñoz, J. A. & Popović, L. Č. 2005, Mem. S. A. It. Suppl., 7, 48

Abajas, C., Mediavilla, E., Muñoz, J. A., Gómez-Álvarez, P. & Gil-Merino, R. 2006, submitted

Alcock, C., Allsman, R. A., Alves, D. R., Axelrod, T. S., Becker, A. C., et al. 2000a, ApJ, 541, 734

Alcock, C., Allsman, R. A., Alves, D. R., Axelrod, T. S., Becker, A. C., et al. 2000b, ApJ, 542, 281

Antonucci, R. 1993, ARA&A, 31, 473

Arav, N., Barlow, T. A., Laor, A., Sargent, W. L. W. & Blandford, R. D. 1998, MNRAS, 297, 990

Baade, W. & Minkowski, R. 1954, ApJ, 199, 206

Barnothy, J. M. 1965, AJ, 70, 666

Bartelmann, M. & Schneider, P. 2001, Physics Reports 340, 291

Belle, K. E. & Lewis, G. F. 2000, PASP, 112, 320

Blandford, R. D. & Mckee, C. F. 1982, ApJ, 255, 419

Blandford, R. D. 1990, In *Saas-Fee Advanced Course 20*, ed. T. J. L. Courvoisier & M. Mayor. Springer-Verlag, Berlin, Heidelberg, New York

Blandford, R. D. & Narayan, R. 1992, ARA&A, 30, 311

Boronson, T. A. & Green, R. F. 1992, ApJS, 80, 109

Bradley, S. E. & Puetter, R. C. 1986, A&A, 165, 31

Chang, K. & Refsdal, S. 1979, Nature, 282, 561

Chang, K. & Refsdal, S. 1984, A&A, 132, 168

Chartas, G., Agol, E., Eracleous, M., Garmire, G. P., Bautz, M. W. & Morgan, N. D. 2002, ApJ, 568, 509

Chartas, G., Eracleous, M., Agol, E. & Gallagher, S.C. 2004, ApJ, 606, 78

Chelouche, D. 2005, ApJ, 629, 667

Chen, K., Halpern, J. P. & Filippenko, A. V. 1989, ApJ, 339, 742

Chwolson, O. 1924, Astr. Nachrichten, 221, 329

Colley, W. N., Tyson, J. A. & Turner, E. L. 1996, ApJ, 461, L83

Collin-Souffrin, S., Dumont, S. & Tully, J. 1982, A&A, 106, 362

Crenshaw, D. M. 1986, ApJS, 62, 821

Dai, X., Chartas, G., Agol, E., Bautz, M. W. & Garmire, G. P. 2003, ApJ, 589, 100

de Robertis, M. 1985, ApJ, 289, 67

Dumont, A. M. & Collin-Souffrin, S. 1990a, A&A, 229, 302

Dumont, A. M. & Collin-Souffrin, S. 1990b, A&A, 229, 313

Eddington, A. S. 1920, *Space, time and gravitation*, Cambrige University Press

Einstein, A. 1915, Sitzungber. Preuf. Akad. Wissench., erster Halbband, 831

Einstein, A. 1936, Science, 84, 506

Eracleous, M. & Halpern, J. P. 1994, ApJS, 90, 1

Fabian, A. C., Iwashawa, K., Reynolds, C. S. & Young, A. J. 2000, PASP, 112, 1145

Falco, E. E., Kochanek, C. S. & Muñoz, J. A. 1998, ApJ, 494, 47

Falco, E. E., Impey, C. D., Kochanek, C. S., Lehár, J., McLeod, B. A., Rix, H. -W., Keeton, C. R., Muñoz, J. A. & Peng, C. Y. 1999, ApJ, 523, 617

Fath, E. A. 1908, Lick Observatory Bulletin, 5, 71

Fluke, C. J. & Webster, R. L. 1999, MNRAS, 302, 68

Gaskell, C. M. & Sparke, L. S. 1986, ApJ, 305, 175

Gil-Merino, R. & Lewis, G. F. 2005, A&A, 437, L18

Goad, M. & Koratkar, A. 1998, ApJ, 495, 718

Goldman, I. & Bahcall, J. N. 1982, A&A, 115, 242

Gómez-Álvarez, P., et al. 2006, ApJ, Submitted

Gould, A. & Miralda-Escude, J. 1997, ApJ, 483, L13

Grieger, B., Kayser, R. & Refsdal, S. 1988, A&A, 194, 54

Hazard, C., Mackey, M. B. & Shimmins, A. J. 1963, Nature, 197, 1037

Hewitt, J. N., et al. 1988, Nature, 333, 537 .

Hewitt, J. N., Turner, E. L., Lawrence, C. R., Schneider, D. P. & Brody, J. P. 1992, AJ, 104, 968

Hoffmeister, C. 1929, AN, 236, 233

Huchra, J., Gorenstein, M., Horine, E., Kent, S., Perley, R., Shapiro, I. I. & Smith, G. 1985, AJ, 98, 1989

Inada, N., Oguri, M., Keeton, C. R., Eisenstein, D. J., Castander, F. J., et al. 2003, Nature, 426, 810

Irwin, M. J., Webster, R. L., Hewett, P. C., Corrigan, R. T. & Jedrzejewski, R. I. 1989, AJ, 98, 1989

Iwashawa, K., Fabian, A. C., Young, A. J., Inoue, H. & Matsumoto, C. 1999, MNRAS, 306, L19

Jackson, N. J. & Browne, I. W. A. 1991, MNRAS, 250, 414

Jackson, N., de Bruyn, A. G., Myers, S., Bremer, M. N., Miley, G. K., et al. 1995, MNRAS, 274, L25

Jennison, R. C. & Das Gupta, M. K. 1953, Nature, 172, 996

Kaspi, S., Smith, P. S., Netzer, H., Maoz, D., Jannuzi, B. T. & Giveon, U. 2000, ApJ, 533, 631

Kaspi, S., Maoz, D., Netzer, H., Peterson, B. M., Vestergaard, M. & Jannuzi, B. T. 2005, ApJ, 629, 61

Kassiola, A. & Kovner, I. 1993, ApJ, 417, 450

Kayser, R., Refsdal, S. & Stabell, R. 1986, A&A, 166, 36

Klimov, Y. G. 1963, Sov. Phys. Doklady, 8, 119

Kochanek, C. S. 2004, ApJ, 605, 58

Koratkar, A. P. & Gaskell, C. M. 1991, ApJS, 75, 719

Kormann, R., Schneider, P. & Bartelmann, M. 1994, A&A, 284, 285

Kovner, I. 1987, ApJ, 312, 22

Krolik, J. H. 1999, *Active Galactic Nuclei: from the central black hole to the galactic environment*, Princeton, N. J. : Princeton University Press

Kwan, J. & Carroll, T. J. 1982, ApJ, 261, 25

Lang, K. R. 1980, *Astrophysical Formulae: A compendium for the Physicist and Astrophysicit.* Springer-Verlag, Berlin, Heidelberg, New York

Laplace, P. S. 1795, *Exposition du systme du monde*

Lehár, J., Falco, E. E., Kochanek, C. S., McLeod, B. A., Muñoz, J. A., Impey, C. D., Rix, H. -W., Keeton, C. R. & Peng, C. Y. 2000, ApJ, 536, 584

Lewis, G. F. & Ibata, R. A. 1998, ApJ, 501, 478

Lewis, G. F., Irwin, M. J., Hewett, P. C. & Foltz, C. B. 1998, MNRAS, 295, 573

Lewis, G. F. & Ibata, R. A. 2004, MNRAS, 348, 24

Liebes, S. 1964, Phys. Rev. B., 133, 835

Lodge, O. J. 1919, Nature, 104, 354

Lynds, R. & Petrosian, V. 1986, Bull. AAS, 18, 1014

MacLeod, J. M. & Andrew, B. H. 1968 ApJL, 1, 243

Maltby, P. & Moffet, A. T. 1963, ApJS, 7, 141

Marziani, P., Calvani, M. & Sulentic, J. W. 1992, ApJ, 393, 658

Mathews, W. G. 1982, ApJ, 258, 425

Matthews, T. A., Morgan, W. W. & Schmidt, M. 1964, ApJ, 140, 35

McGimsey, B. Q., Smith, A. G., Scott, R. L., Leacock, R. J., Edwards, P. L., Hackney, R. L. & Hackney, K. R. 1975, AJ, 80, 895

Mediavilla, E., Arribas, S., del Burgo, C., Oscoz, A., Serra-Ricart, M., et al. 1998, ApJL, 503, L27

Michell, J. 1982, *Black Holes: Selected reprints*, Stony Brook. Originally appeared in 1784, Trans. R. Soc. London, 74, 35.

Miller, P., Rawlings, S., Saunders, R. & Eales, S. 1992, MNRAS, 254, 93

Minkowski, R. 1960, ApJ, 132, 908

Misner, C. W., Thorne, K. S. & Wheeler, J. A. 1973, *Gravitation*, W. H. Freeman and Company

Muñoz, J. A., Mediavilla, E., Falco, E. E., Oscoz, A., Barrena, R., et al. 2001, ApJL, 563, L107

Nandra, K., George, I. M., Mushotzky, R. F., Turner, T. J. & Yaqoob, T. 1997, ApJ, 477, 602

Nandra, K., George, I. M., Mushotzky, R. F., Turner, T. J. & Yaqoob, T. 1999, ApJ, 523, L17

Nemiroff, R. 1988, ApJ, 335, 593

Netzer, H. 1990, In *Saas-Fee Advanced Course 20*, ed. T. J. L. Courvoisier & M. Mayor. Springer-Verlag, Berlin, Heidelberg, New York

Newton, I. 1704, *Optics*, 2nd edn, query 1

Oguri, M., Inada, N., Keeton, C. R., Pindor, B., Hennawi, J. F., et al. 2004, ApJ, 605, 78

Oshima, T., Mitsuda, K., Fujimoto, R., et al. 2001, ApJ, 563, L103

Osterbrock, D. E. & Shuder, J. M. 1982, ApJS, 49, 149

Osterbrock, D. E. 1989, *Astrophysics of Gaseous Nebulae and Active Galactic Nuclei*, Milley Valley, University Science Books

Paczyński, B. 1986, ApJ, 301, 503

Padmanabhan, T. 1993, *Structure formation in the Universe*, Cambridge University Press

Peacock, J. A. 1999, *Cosmological Physics*, Cambridge University Press

Peebles, P. J. E. 1993, *Principles of Physical Cosmology*, Princeton University Press, Princeton

Penston, M. V., Croft, S., Basu, D. & Fuller, N. 1990, MNRAS, 244, 357

Perry, J. J. & Dyson, J. E. 1985, MNRAS, 213, 665

Peterson, B. M. 1993, PASP, 105, 247

Peterson, B. M. & Wandel, A. 1999, ApJL, 521, L95

Peterson, B. M. 2001, in *The starburst-AGN Connection*, Singapur: World Scientific

Peterson, B. M. 2004, *Physics of Active Galactic Nuclei at all Scales*, Springer Lecture Notes in Physics Series, Ed. Alloin, D., 693

Peterson, B. M., Ferrarese, L., Gilbert, K. M., Kaspi, S., Malkan, M. A., et al. 2004, ApJ, 613, 682

Popović, L. Č., Mediavilla, E. & Muñoz, J. A. 2001, A&A, 378, 295

Popović, L. Č., Mediavilla, E., Jovanović, P. & Muñoz, J. A. 2003, A&A, 398, 975

Popović, L. Č., Jovanović, P., Mediavilla, E., Zakharov, A. F., Abajas, C., Muñoz, J. A. & Chartas, G. 2006, ApJ, 637, 620

Rauch, K. P. & Blandford, R. D. 1991, ApJ, 381, 39

Rees, M. J. 1971, Nature, 229, 312

Rees, M. J. 1984, ARA&A, 22, 471

Refsdal, S. 1964a, MNRAS, 128, 295

Refsdal, S. 1964b, MNRAS, 128, 307

Refsdal, S. 1966a, MNRAS, 132, 101

Refsdal, S. 1966b, MNRAS, 134, 315

Refsdal, S. & Surdej, J. 1994, Rep. Prog. Phys., 56, 117

Richards, G. T., Fan, X., Schneider, D. P., Vanden Berk, D. E., Strauss, M. A., et al. 2001, AJ, 121, 2308

Richards, G. T., Johnston, D. & Hennawi, J. 2004, IAU Circ., 8325, 2

Richards, G. T., Keeton, C. R., Pindor, B., Hennawi, J. F., Hall, P. B., et al. 2004, ApJ, 610, 679

Robertson, H. P. 1935, ApJ, 82, 284

Robinson, A. & Pérez, E. 1990, MNRAS, 244, 138

Robinson, A. 1995, MNRAS, 272, 647

Robson, I. 1996, *Active Galactic Nuclei*, Wiley-Praxis Series in Astronomy and Astrophysics, New York

Schmidt, M. 1963, Nature, 197, 1040

Schmidt, R., Webster, R. L. & Lewis, G. F. 1998, MNRAS, 295, 488

Schmitt, J. L. 1968, Nature, 218, 663

Schneider, P. 1996, IAU Symposia, 168, 209

Schneider, P. & Weiss A. 1987, A&A, 171, 49

Schneider, P. & Wambsganss, J. 1990, ARA&A, 273, 42

Schneider, P., Ehlers, J. & Falco, E. 1992, *Gravitational Lenses*, Berlin: Springer

Seyfert, C. K. 1943, ApJ, 97, 28

Shalyapin, V. N., Goicoechea, L. J., Alcalde, D., Mediavilla, E., Muñoz, J. A. & Gil-Merino, R. 2002, ApJ, 579, 127

Smith, M. D. & Raine, D. J. 1985, MNRAS, 212, 425

Soldner, J. 1804, Berliner Astronomisches Jahrbuch, 161

Soucail, G., Fort, B., Mellier, Y. & Picat, J. P. 1987, A&A, 172, L14.

Stirpe, G. M. 1990, A&AS, 85, 1049

Strittmatter, P. A., Serkowski, K., Carswell, R., Stein, W. A., Merrill, K. M. & Burbidge, E. M. 1972, ApJ, 175, L7

Terlevich, R., Tenorio-Tagle, G., Franco, J. & Melnick, J. 1992, MNRAS, 255, 713

Tyson, J. A., Valdes, F. & Wenk, R. A. 1990, ApJL, 349, L1

Ulrich, M. -H., Maraschi, L. & Urry, C. M. 1997, ARA&A, 35, 445

Walker, A. G. 1935, Quant. Journ. Math. Oxford Sci., 6, 81

Walsh, D., Carswell, R. F. & Weymann, R. J. 1979, Nature, 279, 381

Wambsganss, J. 1990, PhD thesis, Munich University, report MPA 550

Wambsganss, J., Paczyński, B. & Katz, N. 1990, ApJ, 352, 407

Wambsganss, J., Paczyński, B. & Schneider, P. 1990, ApJL, 358, L33

Wambsganss, J. & Paczyński, B. 1991, AJ, 102, 86

Wambsganss, J. 1998, Living Reviews in Relativity, 1, 12

Wandel, A., Peterson, B. M. & Malkan, M. A. 1999, ApJ, 526, 579

Weedman, D. W. 1986, *Quasar astronomy*, Cambridge University Press

Weinberg, S. 1972, *Gravitation and Cosmology: Principles and Applications of the General Theory of Relativity*, John Wiley & Sons, New York

Weymann, R. J., et al. 1980, Nature, 285, 641

Wilson, A. S. & Tsvetanov, Z. J. 1994, AJ, 107, 1227

Wisotzki, L., Becker, T., Christensen, L., Helm, A., Jahnke, K., Kelz, A., Roth, M. M. & Sánchez, S. F. 2003, A&A, 408, 455

Witt, H. J. 1990, A&A, 236, 311

Witt, H. J., Kayser, R. & Refsdal, S. 1993, A&A, 268, 501

Wyithe, J. S. B. & Webster, R. L. 1999, MNRAS, 306, 223

Wyithe, J. S. B., Webster, R. L. & Turner, E. L. 2000, MNRAS, 315, 51

Wyithe, J. S. B., Webster, R. L., Turner, E. L. & Mortlock, D. J. 2000, MNRAS, 315, 62

Yonehara, A. 1999, ApJL, 519, L31

Yonehara, A., Mineshige, S., Fukue, J., Umemura, M. & Turner, E. L. 1999, A&A, 343, 41

Yonehara, A. 2001, ApJ, 548, L127

York, D. G., Adelman, J., Anderson, J. E., Anderson, S. F., Annis, J., et al. 2000, AJ, 120, 1579

Young, P. 1981, ApJ, 244, 756

Zheng, W., Binette, M. & Sulentic, J. W. 1990, ApJ, 365, 115

Zwicky, F. 1937a, Phys. Rev. Lett., 51, 290

Zwicky, F. 1937b, Phys. Rev. Lett., 51, 679